THE RELATIONSHIP BETWEEN MECHANICAL PROPERTIES AND MICROSTRUCTURE OF HT9 STEEL

BY

CAROLYN ANNE TOMCHIK

DISSERTATION

Submitted in partial fulfillment of the requirements
for the degree of Doctor of Philosophy in Nuclear Engineering
in the Graduate College of the
University of Illinois at Urbana-Champaign, 2016

Urbana, Illinois

Doctoral Committee:

Professor James F. Stubbins, Chair
Professor Brent Heuser
Assistant Professor Yang Zhang
Professor Pascal Bellon

Abstract

Next-generation advanced reactor system designs present new challenges for material design and selection. The structural materials selected for these reactors will need to withstand higher operation temperatures, more neutron irradiation (greater flux), and corrosion from liquid metal coolants. HT9, a ferritic/martensitic alloy, was used in previous fast research reactors (such as EBR-II and FFTF). However, it needs validation before it can be selected for use in the more extreme environments of Gen–IV reactors. This dissertation presents a series of in-situ high-energy synchrotron X-ray diffraction (XRD) tensile tests conducted on alloy HT9. The loading behavior of HT9 was examined using diffraction line profile analysis methods. Analysis of the shift in diffraction peak position during deformation of the specimens allowed for the determination of elastic lattice strains in the two primary constituent phases of the material: the ferritic/martensitic matrix and the $Cr_{23}C_6$ carbide particles. With the initiation of plastic deformation, the samples exhibited a clear load transfer from the matrix phase to the carbide particulate. The evolution of the dislocation density in the material as a result of deformation was characterized by peak broadening analysis. Small scale tensile samples of HT9 were strained at room temperature and at test temperatures from 300 °C to 500 °C. The $Cr_{23}C_6$ carbide phase in the material is shown to accommodate a significant portion of the load after the ferrite phase yields, despite making up only ~3 % by volume. A set of irradiation-damaged HT9 samples harvested from a duct irradiated in the FFTF were also examined using in-situ XRD. This unique set of specimens extracted from the ACO–3 duct represents a first set of samples to be irradiated under realistic time-variant conditions, including cyclic temperature and fluence variations.

To everyone who encouraged my curiosity; I blame you.

Acknowledgments

I would like to express heartfelt thanks to my advisor, committee chair, and department head, Prof. James F. Stubbins, for his friendly and patient advising throughout my time in the NPRE department. I am appreciative of his flexibility, allowing me to self-direct and advance my work while remaining a present and active member of my family and community. I am thankful for his support and encouragement to travel to meetings and conferences around the world. I met many accomplished and generous students, scientists, and professors in my travels. They have all contributed to the development of this work, my identity as a researcher, and building a network of friends and colleagues that extends across oceans.

I would like to thank Prof. Brent Heuser, Prof. Yang Zhang, and Prof. Pascal Bellon for their service on my dissertation committee, being flexible and generous with their time, and providing thoughtful feedback to improve this work.

I would like to thank Dr. Don Brown for giving me the opportunity to study the ACO–3 tensile XRD samples, letting me spend a week with his research group at LANL, and providing invaluable instruction and guidance in XRD analysis, technical writing, and research. He is an exceedingly kind and talented researcher; I am thankful for his mentoring.

I would like to thank Dr. Levente Balough, for patiently teaching me to use eCMWP line profile fitting software and assisting with line profile analysis.

For their study of the ACO–3 duct material and constant willingness to help, I would like to thank: Dr. Osman Anderoglu for TEM examinations of as-irradiated and strained samples; Dr. Bjorn Clausen and Dr. Thomas Sisneros for their related studies of the ACO-3 duct materials and their help to plan complimentary work; and Dr. Stuart Maloy for providing the HT9 materials for study and his continued leadership of the nuclear materials community in the development of advanced structural materials.

I am grateful to Dr. Kun Mo for his mentoring, guidance, co-op support, and friendship. I would also like to thank him for sharing his adaptation of Jon Almer's MATLAB script, which was used to analyze most of the XRD diffraction patterns in this work.

I would like to thank Dr. Abdellatif Yacout, the Nuclear Engineering division, and the ANL summer intern program, for supporting me on internship and co-op appointment at Argonne National Lab.

For their support of the XRD experiments at APS, I would like to thank: Dr. Jon Almer, Dr. John Okasinski, and Dr. Jun-Sang Park at beamline 1-ID; and Dr. Jeff Terry, Dr. Joshua Wright, and Rachel Seibert at sector 10, MRCAT.

I owe thanks to Cliff Gulyash with the MRL machine shop at UIUC for his frequent and extraordinary effort machining samples under ridiculous time constraints. And for telling me to always tape shut my sample boxes - this saved my work on more than one occasion and is advice I pass along to new experimentalists.

I would like to acknowledge my fellow researchers at UIUC, past and present, who I am lucky to call my friends; most especially, Bei Ye, Wei-Ying Chen, Yinbin Miao, Xiang Liu, Guangming Zhang, Kuan-Che Lan, Jun-Li Lin, Di Yun and Maria Okuniewski- for sharing results, advice, grueling overnight shifts at the APS, meals, and laughs.

I would also like to thank former doctoral students who mentored and allowed me to work with them as an undergraduate student, fostering my interest in research: Dr. Darren Alman, Prof. Jean Paul Allain, and Dr. Matt Coventry.

I would like to thank my friends and family for their unwavering support, and for only asking once in a while if I'd "finished yet?"

I am thankful for my best friends, confidants, and fellow researchers, Aaron Oaks and Ian Percel, They never stop inspiring, comforting, and pushing me, and do each at exactly the right time. I'd also like to thank Aaron for teaching me to use LaTeX, this looks sharp.

Finally, I would like to thank my husband, Ed Lachner, my daughter, Violet, and my dog, Persie. Completing this dissertation was made easier with their love, hugs, and late-night snack deliveries. Extra special thanks are owed to Violet, her thoughtful questions and infectious giggles motivate me on even the toughest days.

This research used resources of the Advanced Photon Source, a U.S. Department of Energy (DOE) Office of Science User Facility operated for the DOE Office of Science by Argonne National Laboratory under Contract No. DE-AC02-06CH11357. MRCAT operations are supported by the Department of Energy and the MRCAT member institutions. Support for this study was also provided by DOE NEUP under grant number 485363-973000-191100, entitled Irradiation Performance of Fe-Cr Base Alloys.

Table of Contents

Chapter 1 Introduction . . . 1
1.1 Motivation . . . 1
1.2 Research Focus . . . 3

Chapter 2 Background . . . 5
2.1 Applications and Limitations of HT9 . . . 5
2.2 Radiation Damage . . . 6
2.3 The Development of Alloy HT9 . . . 7
2.3.1 Steel and Alloying Elements . . . 7
2.3.2 Advanced Alloys for Nuclear Applications . . . 9
2.3.3 Characterization and Properties of Alloy HT9 . . . 10
2.3.4 Radiation Damage and HT9 . . . 12
2.4 Irradiation History of the ACO–3 Duct . . . 14
2.5 Previous Work on the ACO–3 Duct Samples . . . 15
2.6 X-ray Diffraction . . . 16
2.7 Line Profile Analysis . . . 19
2.8 Goals of the Present Research Study . . . 20

Chapter 3 Continuous Strain Testing of Unirradiated HT9 at Elevated Temperature 23
3.1 Experimental Methods . . . 23
3.1.1 Sample Details . . . 23
3.1.2 Test Conditions . . . 24
3.2 X-ray Diffraction Analysis for Determination of Phase Strain and Stress . . . 27
3.3 Results . . . 30
3.3.1 Lattice Strains . . . 33
3.3.2 Phase Stresses . . . 35

Chapter 4 Stepwise Straining of Unirradiated HT9 at Elevated Temperature . . . 44
4.1 Experimental Methodology . . . 45
4.1.1 Modular Load Testing Environment . . . 45
4.1.2 Test Conditions . . . 45
4.2 X-ray Diffraction Analysis . . . 49
4.3 Results . . . 52
4.3.1 Lattice Strains . . . 54
4.3.2 Phase Stresses . . . 56

4.3.3 Dislocation Density Evolution . . . 58

Chapter 5 X–ray Diffraction Study of Load Partitioning in Irradiated HT9 Strained at Room Temperature . . . 60
5.1 Experimental Methodology . . . 61
5.1.1 Source and History of Material . . . 61
5.1.2 Sample Preparation . . . 61
5.1.3 Experimental Conditions . . . 62
5.2 X-ray Diffraction Analysis . . . 64
5.2.1 Phase Strain and Stress . . . 64
5.2.2 Line Profile Analysis . . . 66
5.3 Results . . . 67
5.3.1 Lattice Strains . . . 68
5.3.2 Phase Stresses . . . 72
5.3.3 Peak Broadening . . . 73

Chapter 6 Discussion . . . 76
6.1 The Effect of Sample Irradiation Conditions . . . 76
6.1.1 Elastic Deformation . . . 76
6.1.2 Plastic Deformation . . . 77
6.2 The Effect of Tensile Testing Conditions . . . 80
6.2.1 Elastic Region . . . 80
6.2.2 Plastic Region . . . 82
6.2.3 Dislocation Density Evolution . . . 84

Chapter 7 Conclusion . . . 87
7.1 Load Partitioning Behavior of Alloy HT9 . . . 87
7.2 Influence of Irradiation Conditions on the Microstructure and Mechanical Properties of HT9 . . . 88
7.3 Technical Impact and Merit . . . 88

Chapter 8 Recommendations for Future Work . . . 90
8.1 Alpha Prime Precipitation . . . 90
8.2 Complementary Experimental Techniques . . . 91
8.3 Further Analysis of Diffraction Data . . . 91
8.4 Further Study of Radiation Effects . . . 92
8.4.1 In-situ XRD of HT9 Samples Irradiated in ATR . . . 92
8.4.2 In-situ XRD with Ion Irradiation and Tensile Testing at XMAT . . . 92

References . . . 93

Chapter 1

Introduction

1.1 Motivation

The U.S. International Energy Information Administration (EIA) predicts there could be a 48% increase in world energy demand between 2012 and 2040 with a 69% increase in electricity generation as a result of increasing global population and worldwide economic growth [1]. Concerns about energy security and greenhouse gas emissions motivate the development of more nuclear power plants to meet growing energy needs without contributing to the increasingly urgent problem of climate change (and without depending upon potentially cost-volatile fossil fuel sources). With public enthusiasm for nuclear power waning in the wake of the devastating 2011 tsunami and accident at the Fukushima Daiichi power plant in Japan, the nuclear industry must focus even more sharply on developing more affordable and safer reactors. Several new concepts have been proposed to address the need for improved energy and cost efficiency while including passive safety features. The most promising advanced next-generation (Gen IV) nuclear fission and fusion reactor proposals are now being considered. These designs necessitate developing and qualifying materials for use in harsher temperature and irradiation environments than those in current commercial reactors, as shown in fig. 1.1 [2]. Ferritic/Martensitic (F/M) alloys are promising candidate structural materials for these advanced reactor designs, owing to their resistance to irradiation-induced creep [3] and void swelling [4], high thermal conductivity, low thermal expansion coefficient, and good high-temperature strength as compared with austenitic steels currently in use [5–10]. Figure 1.2 shows the remarkable difference in material response to irradiation between austenitic and ferritic steels - the void swelling in austenitic 316 SS is substantial and increases sharply with dose. By contrast, the F/M alloys see little swelling even at high dpa.

Alloy HT9, initially developed for fossil-fuel powered plants and later chosen for the US (fast) breeder reactor program, remains one of the leading F/M materials for use in

future nuclear designs including fission, fusion, and fast reactors [11, 12]. HT9 is a top candidate for sodium-cooled fast reactors, in particular, because in addition to excellent radiation resistance, it is compatible with liquid sodium coolant [13]. Despite continued development of more advanced alloys for next-generation reactors, HT9 remains of great interest for study because of the extensive irradiation performance database gathered from samples irradiated in e.g. the EBR-II and the Fast Flux Test Facility (FFTF). The body of previous work done with this alloy also makes it a good choice for doing exploratory work on deformation mechanisms in F/M alloys, since results from complementary studies are available.

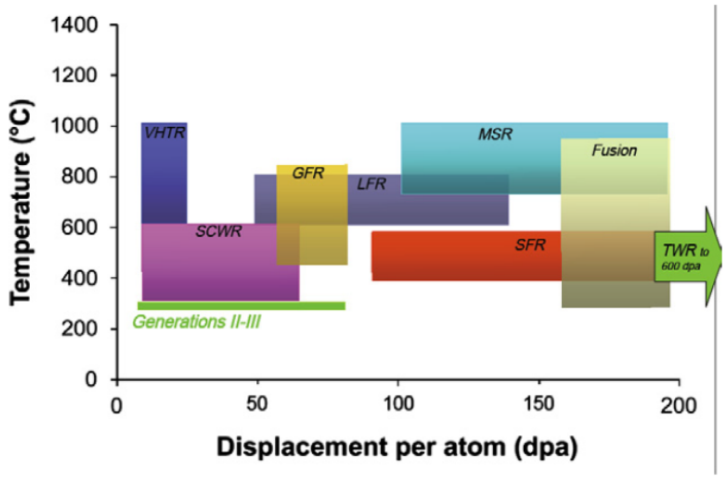

Figure 1.1: Expected operating temperature range and irradiation doses for structural materials in the core of the leading Gen IV reactor concept proposals, the traveling wave reactor, and fusion designs. Steels need to be developed and validated for use in these more extreme environments. Figure from [14].

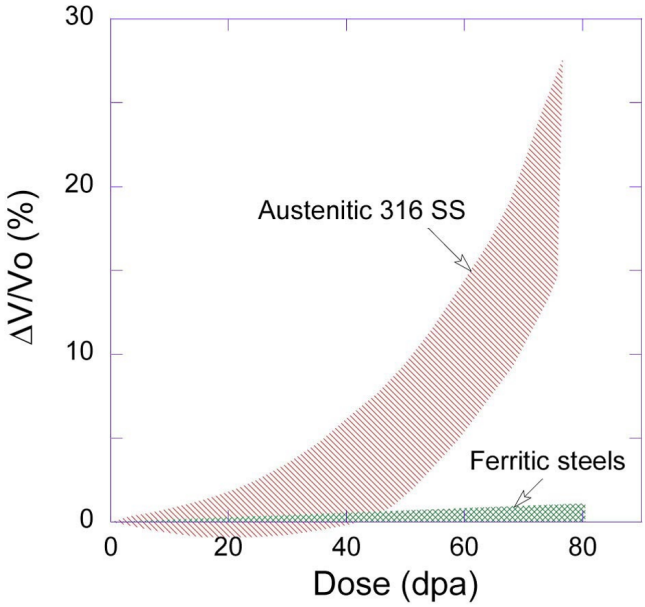

Figure 1.2: Comparison of irradiation-induced swelling between austenitic 316 stainless steel and ferritic/martensitic steels with irradiation in EBR-II at 420 °C showing superior swelling resistance of the latter [5]. Figure from [12].

1.2 Research Focus

HT9 contains a number of precipitated phases, including α' (a matrix-coherent Cr-rich precipitate) and G-phase (a silicide rich in Ni, Mo, and Mn) [15]. It also contains an indigenous population of small carbide structures, identified primarily as $M_{23}C_6$ carbides, making up approximately 3 % by volume. These carbide precipitates are distributed throughout the ferritic/martensitic matrix. Developing an understanding of how these precipitates affect the loading behavior of the material under varying temperature and irradiation conditions is crucial to evaluating HT9's potential for use in future practical applications. Additionally, characterizing the stability or evolution of dislocation and carbide structures as a function of irradiation dose and temperature will be necessary to evaluate this material for extended use in extreme irradiation environments at high temperatures. Since the carbide size distribution and quantity are controllable features in the material design and thermo-mechanical processing technique, an understanding of how they affect loading behavior is also of high value to modeling and future design efforts.

While many studies have been done examining the (macroscopic) mechanical properties of HT9 and similar alloys, using synchrotron radiation to study deformation in this material is a relatively new approach and offers distinct advantages. A high-energy

synchrotron X-ray beam is capable of penetrating into the bulk of a small sample, allowing for statistically significant sampling of material microstructure. An in-line loading frame at the Advanced Photon Source (APS) at Argonne National Laboratory also provides the unique ability to observe microstructural evolution during tensile deformation, rather than merely examining a sample before and after load testing. A detector collects the diffraction peaks from multiple constituent phases within the bulk of the material many times during the course of the deformation. Measuring the shift in each peak position with deformation allows for computation of the associated lattice strain within the phase from which the peak originates. The load partitioning between the constituent phases of the material [16–24], i.e., the way in which the matrix phase sheds excess applied load to the hard precipitate/inclusion phase as it yields, is found by comparing the lattice strain developed in each phase (and in each set of (hkl) oriented grains within a phase). The change in width of the diffraction peaks with deformation gives information about the developing microstructure, as broadening is due to either developing microstrain or a change in the crystallite size. This work examines the load partitioning behavior in HT9 under a variety of irradiation and testing conditions using high energy synchrotron X-ray diffraction.

Chapter 2

Background

2.1 Applications and Limitations of HT9

Alloy HT9, sometimes referred to as 12Cr-1Mo-VW steel, is a high-chromium F/M steel with a nominal composition of Fe-12Cr-1Mo-0.5W-0.5Ni-0.25V-0.2C (in wt%). Sandvik HT9 was originally developed in Europe during the 1960s for the fossil-fuel power industry; later it became the first material chosen for investigation during the development of the U.S. fast reactor program and the first F/M material considered in the U.S. fusion reactor program [6, 25]. Because it has been considered for U.S. nuclear applications since the 1970s, there is a substantial body of work that has examined the effect of radiation on HT9. In Chen's review of this work, he notes that despite having more comprehensive irradiation effects information on HT9 than on similar F/M materials, key issues have yet to be addressed [12]. Namely, HT9 and similar materials exhibit irradiation-induced embrittlement at low temperatures (due to radiation-induced precipitation, hardening, and helium production) which could limit their usability. Increased yield strength and compromised ductility following irradiation at low temperatures has been seen in repeated examinations. An accompanying increase in Ductile to Brittle Transition Temperature (DBTT) presents a significant concern for practical reactor applications, since the temperature of core components will cool during periods of reactor shutdown, making the material susceptible to fracture. Figure 2.1 shows the DBTT of irradiated HT9 material for various irradiation conditions [26]. Note that the lower the temperature, the greater the change in DBTT with fluence and the higher fluence at which the DBTT saturates. Addressing the issue of embrittlement in HT9 and related materials requires a more complete understanding of phase stability and precipitation under various irradiation conditions as well as the contribution of the precipitate phase(s) to fracture behavior.

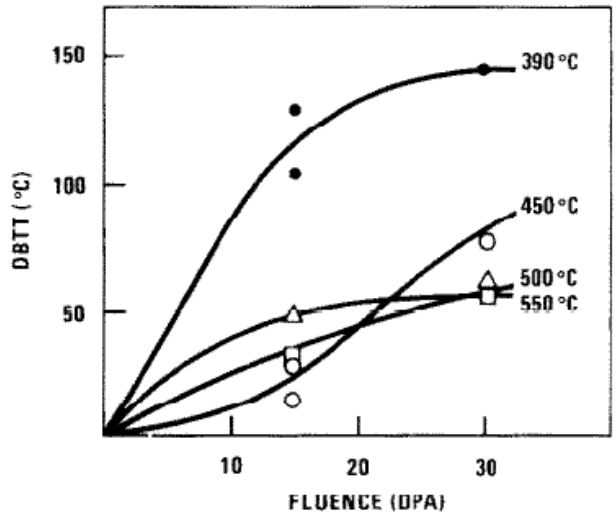

Figure 2.1: The effect of irradiation temperature and fluence on the Ductile-to-Brittle Transition Temperature (DBTT) of HT9, taken from [26].

2.2 Radiation Damage

Radiation damage to crystalline materials depends on the interaction between the incident particle (e.g., neutron or ion) with the atom(s) in the lattice of the material. Briefly, when an energetic particle is incident on a material, it can knock an atom from its lattice position. This first displaced atom becomes known as the primary knock-on atom, or PKA. The incident particle and the PKA can in turn continue to displace additional atoms from the lattice. This is known as a damage cascade. Pairs of self-interstitials and vacancies (Frenkel pairs) are produced within these cascades when atoms are displaced. Many of these pairs will annihilate as interstitials diffuse to nearby vacancy sites following the cascade, but the surviving point defects evolve depending on the irradiation conditions of the material, resulting in radiation induced segregation, phase transformation, and crystalline defects (e.g., voids and dislocations).

Material response to irradiation is known to be highly dependent not only on the irradiation dose, but also on dose rate, irradiation temperature, and irradiating species (e.g., neutron or ion). Therefore, great care must be taken when comparing results of different irradiated material studies. Materials can also be susceptible to the pattern or history of their radiation, including oscillations in flux, temperature, and stress experienced during normal reactor operation. This makes understanding the combined results of different studies additionally difficult, and demonstrates a need to isolate different variable effects when possible. However, when isolating variables (like dose and

temperature) to study their effects independently, one is forced to merely imitate reactor conditions in a limited way (often using an ion beam in place of neutron irradiation, and even more often using an increased dose rate in order to generate relatively high and specific doses in a limited amount of experimental time). Much of the existing data on the irradiation response of HT9 has been derived from separate individual samples irradiated under well-defined conditions within a test assembly. To address a concern that the history effects during realistic reactor operations could result in higher swelling levels in HT9 than those seen under constant irradiation conditions (as was found in austenitic steels [27]), a fuel assembly made of HT9, designated ACO–3, was designed for insertion into an FFTF core experiment that would experience realistic reactor cycling conditions [28]. Samples were extracted from various locations along the ACO–3 duct following its irradiation and designated for various post-irradiation examinations (PIEs). Small tensile samples, among others, were machined from the extracted material; some were made available to us to strain in-situ with high-energy X-ray diffraction.

2.3 The Development of Alloy HT9

2.3.1 Steel and Alloying Elements

When pure molten iron is cooled (at standard pressure), it solidifies first into delta ferrite (at 1538 °C), which has a bcc crystal structure and a carbon solubility of ~0.1 wt.%. Upon further cooling, its crystal structure changes to austenite (at 1394 °C), which has an fcc structure and can dissolve ~2 wt.% carbon. Further cooling transforms the austenite into the bcc alpha ferrite phase, which has a much lower carbon solubility of ~0.02 wt.%. The addition of small amounts of carbon to the iron creates steel. Carbon is an interstitial impurity that distorts the iron lattice, blocking dislocation motion and thereby hardening and strengthening the material. Carbon solubility is dependent upon both the phase (structure) and temperature of the iron. The rate of cooling steel determines its microstructure; the developed structure depends upon the time allowed for carbon to diffuse out of the austenite matrix (forming ferrite and the iron-carbide cementite, Fe_3C). Slow cooling allows for carbon to diffuse out between planes of ferrite, creating alternating lamellae of ferrite and cementite. The resulting structure is termed pearlite. Cooling very quickly (e.g. by quenching in water) does not allow time for diffusion of carbon out of the austenite lattice and thereby traps carbon in solid solution. The matrix accommodates by shearing into a bct structure with the carbon in the lattice. This phase

is called martensite, and can be thought of as ferrite supersaturated with carbon. It is very hard and brittle, but reheating it (tempering) allows carbon to precipitate out of the martensite, transforming it to ferrite, and optimizing the material properties depending on the requirements of the steel. Various alloying elements are also added to alter the steel properties and phase transition temperatures, even creating temperature ranges in which two phases can exist simultaneously (duplex steels).

The addition of chromium results in ferritic stainless steel, wherein chromium substitutes for iron atoms in the matrix. These alloys are termed "stainless" because while iron will oxidize readily in oxygen-containing environments, the addition of sufficient amounts of chromium (generally $>\sim$11%) results in the creation of a thin chromium-oxide layer, or passive film, at the surface that blocks any surrounding oxygen from reaching the iron. In addition to increasing the oxidation and corrosion resistance of an alloy, chromium also promotes the ferrite bcc structure after tempering and can generate fine precipitates that strengthen the steel by inhibiting dislocation motion. The corrosion resistance of steels increases with increasing chromium content. Adding nickel as an alloying element favors the formation of austenite (FeCr alloys with $\sim$10% Ni will be austenitic at room temperature). Molybdenum enhances resistance to localized corrosion (pitting) and adds strength and creep resistance through solid-solution strengthening and carbide precipitate formation. Manganese improves ductility at high temperatures, can alternately stabilize austenite (at low temperature) or ferrite (at high temperature), and increases nitrogen solubility. It can also mitigate potentially harmful effects of sulfur impurities by enabling the formation of MnS rather than the toughness-reducing FeS. Silicon increases oxidation resistance and promotes ferrite formation. It also increases ductility and toughness, reduces corrosion rate, and can form intermetallic compounds that increase strength in precipitation hardened steels. Vanadium will stabilize the bcc ferrite structure and increase tempering resistance. Niobium promotes the formation of ferrite and carbides and enhances high temperature mechanical properties. Needless to say, there are many more alloying elements that can be added to alloys to different effect, depending upon the primary structure of the alloy. The Schaeffler diagram, originally developed for determining the solidifying mode of welding material, is one visualization chart that approximates the combined effects of alloying elements on the phase of the resulting alloy. It weighs all ferrite-stabilizing elements to estimate a chromium equivalent concentration and all the austenite-stabilizing elements toward an equivalent nickel concentration, thereby representing each alloy as an equivalent Fe-Cr-Ni combination. A guide to the resulting alloy structure is then provided by the diagram, shown in fig. 2.2.

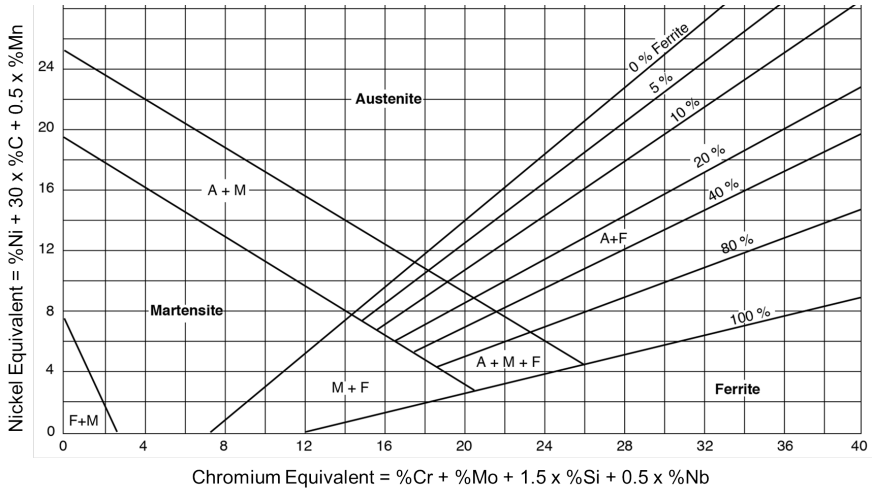

Figure 2.2: The Schaeffler diagram estimates the structure of steel based on the weighted combinations of alloying elements. Figure provided by Sandvik Materials Technology.

2.3.2 Advanced Alloys for Nuclear Applications

Generation II (Gen II) reactors currently operating in most of the world (including in the U.S. and France) as well as advanced reactor designs designated as Gen III and III+ (operating in Japan and under construction elsewhere) use ferritic and austenitic steels for their core structural components. These reactors generally operate to fuel burnups of 50 to 60 GWd/tU and have outlet temperatures in the vicinity of 300 °C. A new generation of reactors is in development under the leadership of the Generation IV International Forum (GIF). This international collective is developing six new reactor technologies with expected deployment dates between 2030 and 2040. The six reactor systems are being developed to meet design goals of enhanced sustainability, environmental friendliness (via reduced waste production), economic viability, safety, reliability, and proliferation resistance.

The proposed Gen IV designs aim to operate at higher temperatures (500 °C to 1000 °C) and achieve more than double the fuel burnup of current reactors (~100-200 GWd/tU) [2]. Ferritic alloys have insufficient strength at these high temperatures. While austenitic alloys have shown resistance to creep at high temperature, they suffer from void swelling as a result of neutron irradiation, which greatly compromises their mechanical strength. Gen IV reactor designs therefore require the development of advanced materials to withstand harsher radiation environments as well as higher temperatures. The ferritic/martensitic class of materials has adequate strength, superior thermal conductivity, and resistance to void swelling for longer-term use at higher temperatures. A representation of the evolution and development of the ferritic/martensitic alloy HT9 from grade 410 stainless

steel is shown in fig. 2.3.

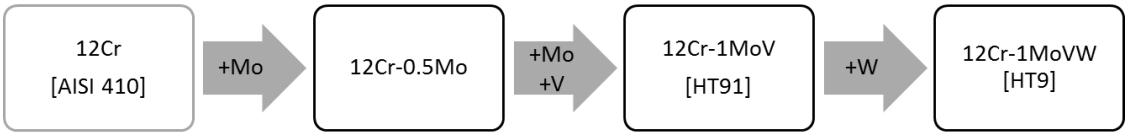

Figure 2.3: Development process for alloy HT9 ferritic/martensitic steel. The first alloy, AISI 410, has a 105h creep rupture strength of 35 MPa at 600 °C, the addition of Mo in the next development increased it to 60 MPa [6].

Structural materials for fusion applications, such as those for the tritium breeding blanket and first wall, will require similar high temperature and radiation tolerance, and need to produce only low-activity by-products for safe disposal at the end of their service life. Requirements for fusion reactors are close to those for Gen IV fission reactors, so research and materials development for them is mutually applicable. Relatively little modification is needed to adapt Gen IV-appropriate alloys for use in fusion reactors. The modified group of alloys designed to create only low-activity by-products when used in fusion systems are known as reduced-activation ferritic/martensitic (RAFM) alloys. They were developed by substituting alloying elements in familiar high-chromium steels for ones that would not transmute and generate radioactive isotopes when absorbing a high-energy fusion neutron. Molybdenum (Mo) was replaced largely by tungsten (W), another ferrite-stabilizer and strengthener; tungsten carbides also coarsen more slowly than those formed by Mo, further improving the tensile strength, ductility, and toughness of the material. Nickel (Ni) was replaced with manganese (Mn), lowering potential activation while still encouraging the formation of martensite.

2.3.3 Characterization and Properties of Alloy HT9

Alloy HT9 is a strong stainless steel with a nominal composition of Fe-12Cr-1Mo-0.5W-0.5Ni-0.25V-0.2C (in wt%). It is often referred to in the literature as "12Cr-1MoVW" steel. The microstructure of normalized-and-tempered HT9 is a fine lath tempered martensite (ferrite). It consists of a ferritic/martensitic matrix with inclusions of carbide precipitates (primarily $M_{23}C_6$) [29]. The lath structure and precipitate distribution is heavily dependent on processing conditions. Austenitization temperatures from 950 °C to 1200 °C produce prior austenite grains (PAG) sizes of 25 µm to 330 µm and lath packet sizes of 10 µm to 95 µm, respectively; the PAG to lath packet size ratio remains ~3:1

in all cases [30]. The lath width is generally ~1 µm. The austenitizing temperature also determines the precipitated carbide size and morphology: carbides (approximately 0.06 µm × 0.2 µm) are generally distributed along the PAG boundaries with some larger ones (1 µm × 3.5 µm) appearing at lower austenitizing temperatures. Smaller carbides can also appear along the lath packet and parallel lath boundaries as well as within the laths, their size and shape (blocky to needle-like) depend on austenitization and tempering conditions. The fraction of carbides varies from ~3.4 wt.% in its normalized and tempered condition up to ~4.6 wt.% after aging at 550 °C for 5000 h.

In Klueh's work [29], room temperature testing of two different heats of HT9 showed Yield Strength (YS) and Ultimate Tensile Strength (UTS) of ~640 MPa to 690 MPa and ~800 MPa to 860 MPa, respectively. In elevated temperature tests, the YS was ~540 MPa to 640 MPa at 400 °C, ~500 MPa to 590 MPa at 450 °C, ~500 MPa to 550 MPa at 500 °C, and ~430 MPa to 480 MPa at 550 °C. The UTS followed a similar trend, showing ~670 MPa to 780 MPa at 400 °C and falling to ~600 MPa to 640 MPa at 500 °C. Reported values for total elongation of the heats of HT9 tested in [29] are ~6% at 400 °C up to ~11% at 500 °C, with uniform elongation increasing from ~3% to ~4% in the same respective tests. Uniform elongation decreased to 2% at a test temperature of 550 °C. As established in early tests on this alloy, and represented by the range of values quoted here, the properties of HT9 vary depending upon thermo-mechanical treatment of the alloy. A collection of mechanical properties data derived from numerous sources is amassed in the AFCI Handbook [31], but is currently only available for individual release.

Analysis of tensile tests performed at room temperature through 600 °C on HT9 samples in a nitrogen atmosphere with a strain rate of 10^{-3} / sec indicated that the strength properties of the material were gradually reduced with increasing temperature. The ductility of the material was enhanced at elevated temperatures by enhanced plastic flow. Observation of the fracture surfaces with scanning electron microscopy (SEM) confirmed reduced cracking and the appearance of dimpled microstructures with increased test temperature, confirming more ductile fracture at higher temperatures [32]. The macroscopic stress-strain curves for this set of tensile tests is shown in fig. 2.4. The magnitude of the strength reduction with temperature was greater at test temperatures in excess of 400 °C, and the uniform elongation for 500 °C and 600 °C tests was reduced to the point that the UTS was barely higher than the YS. This behavior is indicative of a critical temperature between 400 °C and 500 °C above which the mobility of lattice imperfections (like dislocations) through their grain boundaries results in greatly enhanced plastic flow. The tests conducted at room temperature through 300 °C showed decreased total elongation with increasing temperature, while tests above 300 °C showed greater elongation with

increasing test temperature. The authors attributed this to the presence of dynamic strain hardening as dislocations became locked in the vicinity of grain boundaries in the lower temperature tests.

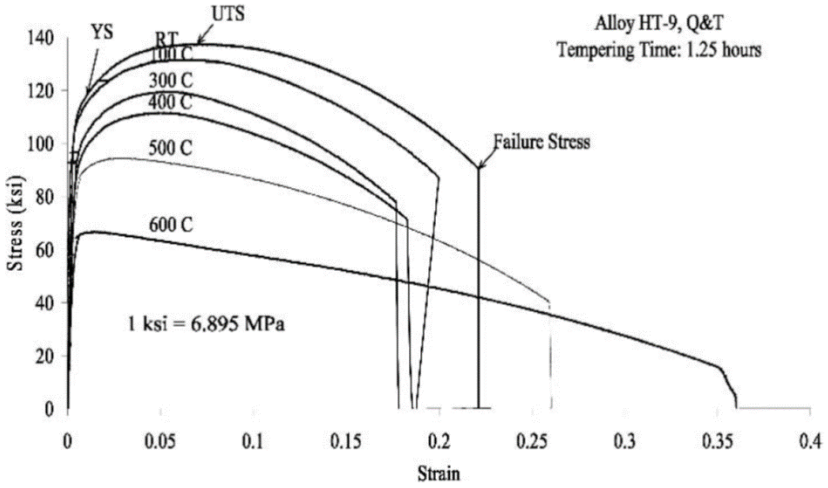

Figure 2.4: The macroscopic stress-strain curves of HT9, strained at 10^{-3}/ sec in a nitrogen atmosphere, with increasing test temperature [32].

2.3.4 Radiation Damage and HT9

The high-temperature strength of HT9 is provided by its microstructure (determined by the choice of heat treatment) and secondary precipitate phases. Exposure to neutron irradiation at reactor operating temperatures could compromise the relied-upon microstructure and precipitations, limiting the alloy's usefulness in nuclear applications. Neutron damage is known to produce damage cascades that leave point defects in the material. These defects then migrate towards defect sinks in the material, such as dislocations or grain boundaries. The re-combination, annihilation and clustering of defects take place at rates determined by the relative sink strengths and defect mobilities. The efficiency of each type of sink in capturing point defects varies, and the difference gives rise to inhomogeneous distribution of point defects at irradiation temperatures, resulting in effects such as void swelling, irradiation creep, and radiation-induced segregation.

The irradiation effects in alloy HT9 ferritic/martensitic steel have been explored experimentally through irradiation of HT9 samples at, e.g., HFIR (High Flux Isotope Reactor), the EBR-II (Experimental Breeder Reactor II), FFTF (Fast Flux Test Facility), and PHENIX, as well as at STIP II (SINQ Target Irradiation Program). Dislocation density was greatly

reduced with increasing irradiation temperature. In one ion-irradiation examination [33] at irradiation temperatures above 600 °C, there was no discernible difference in the unirradiated and irradiated dislocation densities, indicating material recovery at this temperature. Another study of ion irradiation showed significant recovery in HT9 at ~500 °C [34]. With regard to precipitate structures in HT9, irradiation can result in the dissolution of initial carbide precipitates by atomic mixing, or it can result in coarsening by radiation-enhanced diffusion, which is highly dependent on the damage rate and irradiation temperature. The difference between the rate of diffusion by interstitial and vacancy mechanisms creates enrichment of the fastest-moving species near defect sinks (like grain boundaries) in what is known as the inverse Kirkendal effect. The concentration of Cr near the grain boundaries in HT9 can be either enriched or depleted depending upon the irradiation dose [35]. A summary of the various precipitates found after irradiation of HT9 material is found in [12], and is reproduced in table 2.1.

Table 2.1: Precipitates found in HT9 as a function of irradiation conditions, from [12].

Irradiation Facility	Precipitate	Temperature (°C)	Dose (dpa)
FFTF	α', χ	420	35
	η	407	47
	α', G	380-440	20-155
Phenix	α'	400-530	30-116
	η	419	79
EBR-II	α', χ, G	400, 425	25-60
HFIR	α', η	400	7.4
	G	300, 400, 500	10-12, 38
14 MeV Ni	α', χ	300-600	200

Evidence of HT9's superior resistance to void swelling with irradiation has been established by examining samples irradiated in HFIR, Phenix, EBR-II, and FFTF. The experimental results support that the onset of void swelling in HT9 occurs at doses in excess of 100 dpa, and the steady-state swelling rate is $< 0.1\%$/dpa. This swelling resistance was attributed to solute trapping caused by the weak interactions between vacancies and Cr, the character of the dislocation loop structure, and the many subgrain and lath boundaries in the microstructure of the tempered martensite [12]. Precipitates in the material may also suppress void swelling by serving as defect sinks to facilitate recombination.

Irradiation of HT9 at low temperatures ($< 0.3T_m$) results in hardening (increased yield strength) and reduced ductility. At these temperatures, hardening is caused by irradiation-produced dislocation loops and defect clusters. Therefore, the hardening may increase with dose but saturate at the point when defects begin to overlap. Examinations of samples irradiated in EBR-II, HFIR, and FFTF indicate yield strength initially increases sharply with dose but saturates near 10 dpa for irradiation temperatures at or under 400 °C [12]. However, there is not any evidence of irradiation hardening for exposure at temperatures above 425 °C. Some of the best experimental evidence for the irradiation-temperature dependence of hardening comes from samples extracted from the ACO–3 duct after irradiation in FFTF. The Ductile-to-Brittle Transition Temperature (DBTT) of HT9 shifts to higher temperatures with exposure to radiation, making the material susceptible to brittle fracture even at the elevated temperatures seen by reactor structural components (particularly during periods of reactor shutdown when the material is cooler). The magnitude of the shift in DBTT is thought to depend, in part, on the carbide content of the material [36]. Irradiation embrittlement is reduced thanks to dislocation recovery and precipitate coarsening at temperatures above 425 °C; Byun reported an abrupt drop in DBTT with irradiation temperature $> 0.3T_m$ when examining a set of HT9 samples from the ACO–3 duct [37]. However, some embrittlement persists even at very high temperatures where there is no irradiation hardening because of M_6C precipitates in the material [38]; at high temperatures, irradiation-induced precipitates are responsible for some embrittlement of HT9.

2.4 Irradiation History of the ACO–3 Duct

The ACO–3 assembly was irradiated in three positions in the FFTF core over a six-year period (moving progressively inward toward the core center as the fuel burned down). The assembly contains the first HT9 material subjected to both slowly declining and two sharp increases in neutron flux and temperature (during fuel burn down and when moved inwards, respectively) over the course of its irradiation. Details describing the core arrangement and irradiation cycles can be found in [28]. Samples were extracted from various positions along the ACO–3 hexagonal duct following the irradiation, with average irradiation temperature and dose depending on the position along the duct, see fig. 2.5. Details of the sample extraction technique can be found in [39].

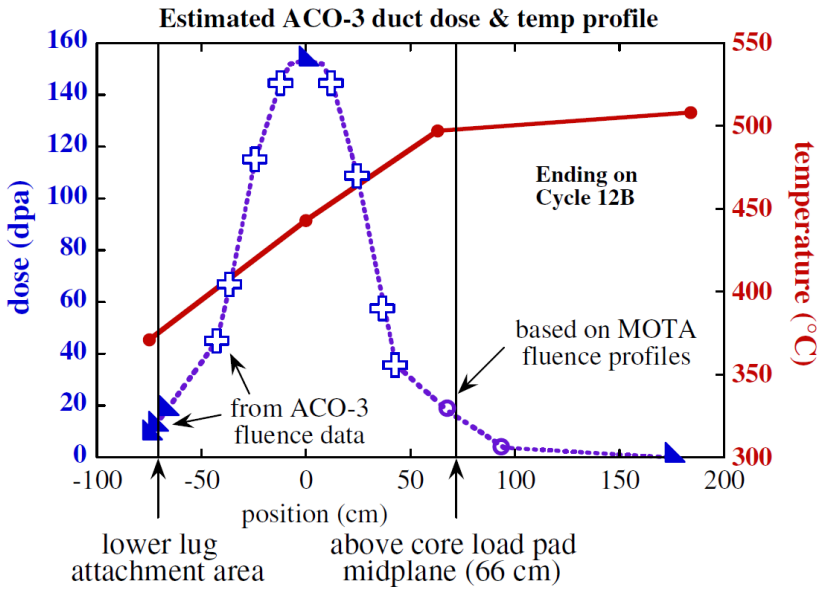

Figure 2.5: Irradiation conditions experienced by the ACO–3 duct, taken from [28].

2.5 Previous Work on the ACO–3 Duct Samples

The irradiation-induced microstructure of the ACO–3 duct material was studied using SANS and APT [15] as well as TEM [15, 28, 40]. Estimation of tensile properties was done via small specimen shear-punch testing [41]. Impact properties and fracture toughness of the irradiated samples were also determined [37, 42, 43]. Most recently, EFTEM, neutron diffraction, and synchrotron X-ray diffraction were used to characterize the as-irradiated microstructure of extracted samples [44]. The dominance of irradiation temperature over dose in affecting irradiation-induced change (over a range of 2-157 dpa and 378 °C to 504 °C) was established, as was the existence of a transition irradiation temperature near $0.3T_m$. This division in results for irradiation temperatures above and below ~$0.3T_m$ (410 °C to 430 °C) is consistent with a trend found in previous work examining HT9 material [12, 41, 45]. Figure 2.6 shows a collection of experimental results on irradiated HT9 samples illustrating a threshold irradiation temperature at ~430 °C.

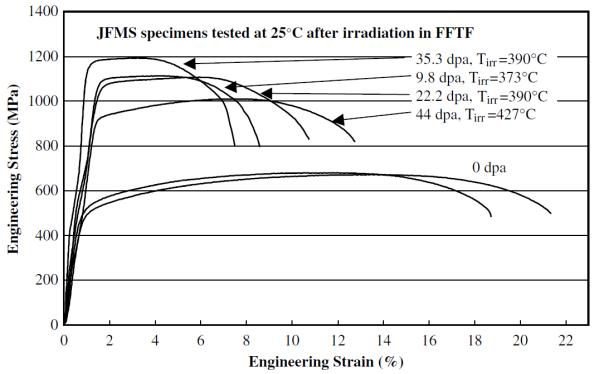

(a) Stress/strain curves measured on tensile specimens of HT9 alloy at 25 °C after irradiation up to 67dpa at 373 °C to 427 °C in FFTF, from [45].

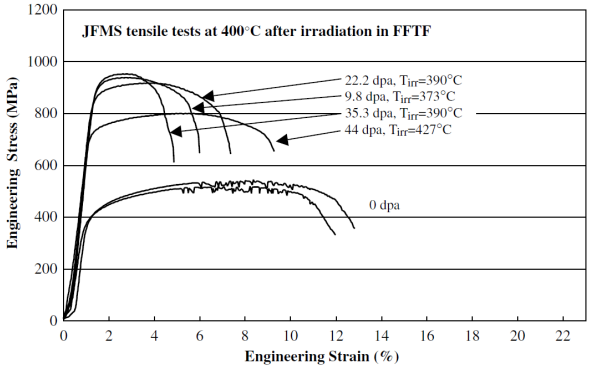

(b) Stress/strain curves measured on tensile specimens of HT9 alloy at 400 °C after irradiation up to 67dpa at 373 °C to 427 °C in FFTF, from [45].

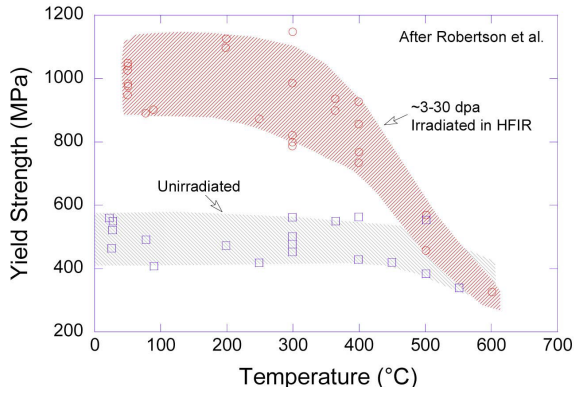

(c) Irradiation temperature dependence of yield strength of HT9 irradiated to ~3-30dpa, from [12].

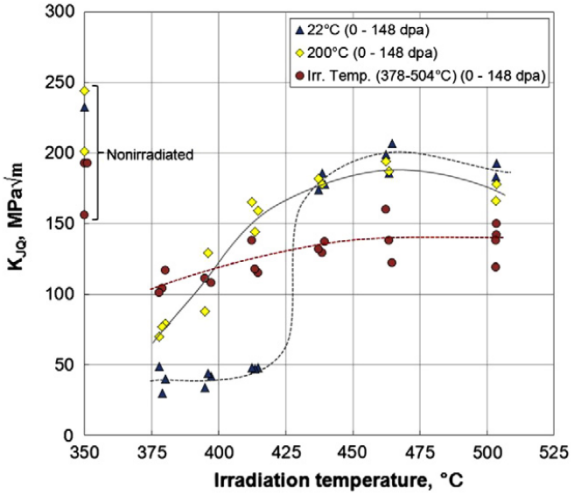

(d) Irradiation temperature dependence of fracture toughness of HT9 at different test temperatures, from [42].

Figure 2.6: Representations of the threshold irradiation temperature near ~$0.3T_m$.

2.6 X-ray Diffraction

X-ray diffraction is a valuable characterization tool; it is becoming more commonly used both in its own right and as a complementary tool to traditional microscopy. Because high-energy, high-brilliance X-rays are capable of penetrating into the depth of steels (on the order of a millimeter), they can provide information about the microstructure of the sample without any need for significant surface preparation of samples. This is particularly advantageous when working with radioactive samples, for which post-irradiation handling and manipulation can be difficult, costly, and restrictive. While

microscopy reveals details of local effects, X-ray diffraction is able to sample the bulk of a material and provide statistical sampling of microstructural evolution throughout the bulk.

When X-rays are incident on a crystalline material, they are diffracted by sets of parallel crystallographic planes in accordance with Bragg's Law:

$$n\lambda = 2d \sin\theta \tag{2.1}$$

where n is an integer, λ is the wavelength of incident radiation, and θ is the diffracted angle of the X-rays. Since we fix the wavelength, λ, of the incident radiation, we can find d_{hkl}, the space between parallel planes of atoms, by:

$$d_{hkl} = \frac{\lambda}{2 \sin\theta} \tag{2.2}$$

The space between parallel planes of diffracting atoms (a set of lattice planes (hkl)) determines the position 2θ of the diffraction peak. We may consider a polycrystalline sample (ignoring texture effects) as a powder in which we sample many randomly oriented grains. When we assume random grain orientations, we know that each set of planes will give rise to a diffraction cone and this will appear on a 2D detector (that cuts across the cone) as a Debye ring at a position 2θ, see fig. 2.7a. The cone is actually made up of many tiny intensity dots, each dot representing diffraction from a single coherently scattering domain. In the case of a sample that contains highly oriented grains, the Debye rings will not be continuous but will rather contain spots of higher and lower intensity, as in fig. 2.7b.

Changes in a material's diffraction pattern stem from changes in its state. For an example, see fig. 2.8. For analysis, we focus primarily on X-ray diffraction peak position shift and broadening. Shifting of peak position (a change in the lattice parameter) is a result of homogeneous strain, or macrostrain, attributable to macroscopic deformation of the material. Broadening of peaks is a result of a) size broadening, a change in the size of coherently scattering domains (crystallite size) and/or b) strain broadening, development of microstrain attributable to linear-type defects, the prototype of which are dislocations. Lattice defects like dislocations in a real crystal displace atoms relative to their ideal position, distorting the reciprocal lattice. Therefore the diffraction condition is satisfied not only at the discrete ideal positions of the reciprocal lattice points, but in a finite volume surrounding each ideal lattice point. This effect is known as strain broadening. Deconvolution of the crystallite size effects from microstrain effects on line broadening is based on the order dependencies and hkl anisotropy.

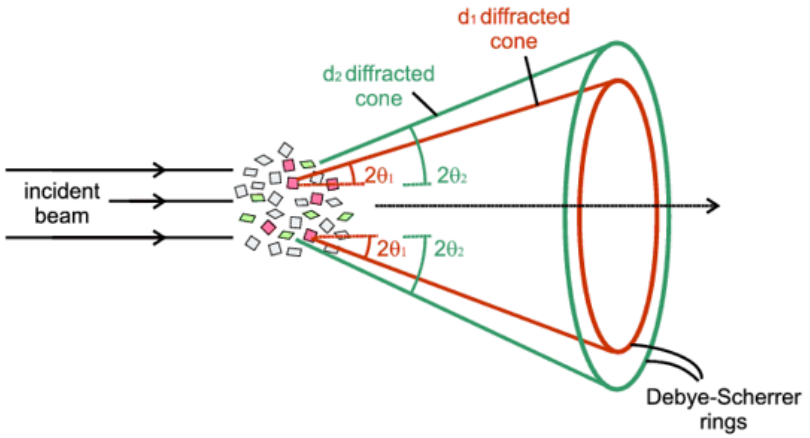

(a) A detector is positioned so that it cuts across the diffraction cone, capturing Debye rings [46].

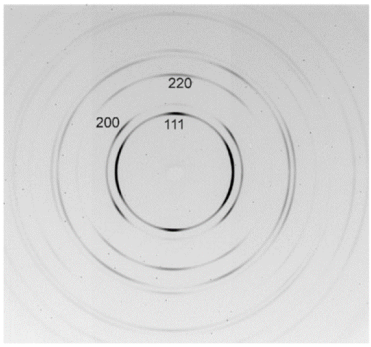

(b) The Debye rings of a sheet of rolled copper show preferred orientation of grains, texture [47].

Figure 2.7: The geometry of Debye diffraction rings.

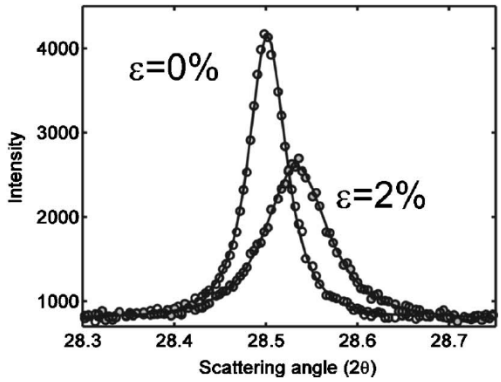

Figure 2.8: An example of the effect of tensile strain on an Al film sample, taken from [48]. The X-ray diffraction spectra were taken before deformation and at a tensile strain of 2 %. The (200) peak clearly displays both peak center shifting and peak broadening due to tensile deformation of the sample. When the material is stretched in the axial direction, it compresses in the lateral direction in accordance with its Poisson's ratio, ν ($\nu = -lateralstrain/axialstrain$). This figure shows the response of the material in the lateral direction, perpendicular to the direction of loading.

2.7 Line Profile Analysis

In order to extract information from the diffraction patterns collected during an X-ray diffraction experiment, it is useful to integrate the diffraction rings over a selected azimuthal region to create a one-dimensional diffraction line profile. In this representation, each ring of the diffraction pattern becomes a single peak in the profile. Analysis of the resulting profile is referred to as diffraction line profile analysis (DLPA). Two approaches exist for fitting the 1-D diffraction line profiles: fitting single peaks individually, and fitting a full peak pattern simultaneously. Full pattern (or whole pattern) analysis methods include the Rietveld Method [49–51] and the extended Convolutional Multiple Whole Profile (eCMWP) method [52, 53]. Peaks are fit with a bell-shaped profile function, most often a Pseudo-Voigt.

Rietveld refinement is a "top down" fitting approach. A model powder diffraction profile is built using specified structural information for each phase of the material (the space group, lattice parameters, and atomic positions in the unit cell). A profile function is built around this model, accounting for instrumental broadening. The analytical profile function relies greatly on the fitting of peak intensities, determined by the complex structure factors F_{hkl} for each phase of the material. Structure factors describe the ratio of the amplitude of the wave scattered by all the atoms in a unit cell to the amplitude of the wave scattered by a single electron. Reflection intensities I_{hkl} are proportional to the square of the structure factor ($I_{hkl} \propto |F_{hkl}|^2$), where F is a function of the atomic scattering factor, f (an electronic property of an atom), and the position of the atoms (u, v, w). The structure factors are found by:

$$F_{hkl} = \sum f_j e^{2\pi i(hu+kv+lw)} \qquad (2.3)$$
$$f_j = f_{j0} e^{-B_j(\frac{\sin\theta^2}{\lambda})}$$

where f_j is the atomic scattering factor, representing the scattering power of an atom divided by the scattering power of an electron, and B_j is the Debye-Waller (or Temperature) factor, which represents the weakening of an atom's scattering power due to its vibrational motion. The structure factors F_{hkl} are therefore determined by crystallography for a given lattice parameter, space group, and atom coordinates. The obtained analytical profile function is then fitted to the data and refined (by a least squares method) through optimization of a set of variables that describe the structure, quantity, and atomic positions

of the phases using simultaneous whole profile fitting [49–51].

The extended Convolutional Multiple Whole Profile (eCMWP) method is a "bottom up" approach in which patterns are fitted by a least squares algorithm and refined for parameters representing physical features of the diffracting material [52, 53], e.g., the subgrain (crystallite) size and distribution, the dislocation density and arrangement parameter, and strain anisotropy. Ab initio theoretical functions for size, strain, and planar faults are convolved with measured instrumental profiles to create a theoretical line profile. The convolution of effects on diffraction intensity is based on that suggested by Warren and Averbach, [54]. Crystallites are assumed to have either spherical or ellipsoidal shape with a lognormal size distribution, and microstrain is assumed to be caused by dislocations. Anisotropy of strain and size are accounted for with the use of contrast factors [55] and ellipticity of the crystallites, respectively. The theoretical model relies on the modified Warren-Averbach Fourier model of broadening [54] and a parameter characterizing the arrangement of dislocations defined by Wilkens [56]. Prior to analysis of the measured diffraction profile, the background is manually fitted and subtracted by a spline created by the user. The theoretical profiles are convolved with the measured instrumental diffraction profile, and the resulting is fitted numerically to the background-subtracted experimental diffraction intensity pattern. The microstructural parameters are then refined by a nonlinear least squares procedure.

2.8 Goals of the Present Research Study

Not only is HT9 of interest for next-generation nuclear systems, it is also similar in structure to many other F/M alloys. Since this study examines the way in which the carbide inclusion phases affect the behavior of the material when exposed to stress, the results can be necessarily extended to F/M alloy development efforts, particularly for those with Fe~12Cr-Mo that have been shown to have very similar mechanical properties (a few examples are shown in fig. 2.9). These results can also be compared with examinations of similar materials to improve understanding of the deformation mechanisms in these steels. The goal of this project is to establish a connection between the microstructure of alloy HT9 and the mechanical properties it exhibits under tension, with the aim of providing an explanation that can extend to other high-Cr F/M steels.

While an extensive database of mechanical properties information exists for the HT9 alloy, these in-situ tensile experiments are the first of their kind on this material, and aim to lend an understanding of how each constituent phase of the material responds to

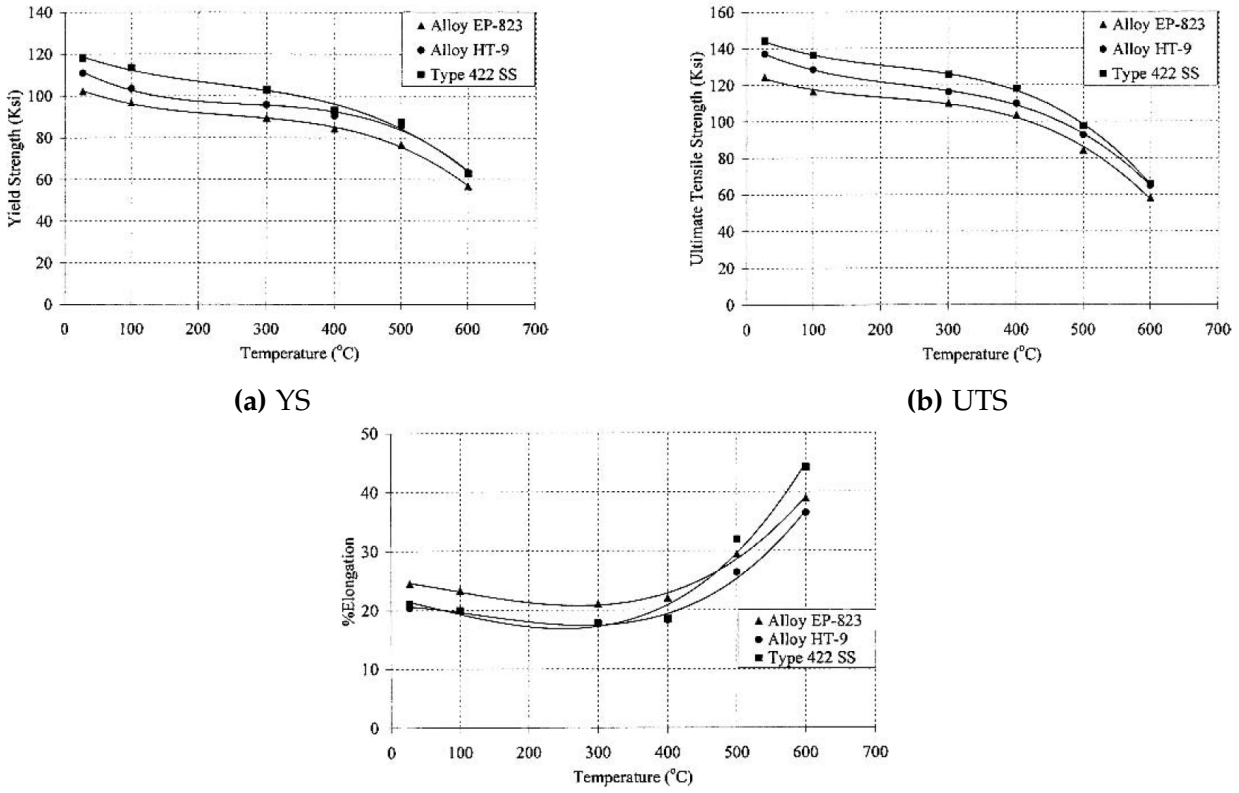

(a) YS **(b)** UTS

(c) % Elongation

Figure 2.9: Mechanical properties of similar Fe~12Cr-Mo alloys as a function of temperature [32]. EPS-823 is a Russian alloy designed for nuclear applications, and type 422 stainless steel is used in high temperature and pressure environments for components like turbine blades in the aircraft and power industry. The alloys show the same mechanical behavior, lending credence to the assertion that the results for the present HT9 study can extend to similar materials.

external strains. With a greater understanding of how each phase accommodates (and subsequently sheds) applied load, we can not only design and optimize better alloys in the future, but can also provide parameters by which modelers can more effectively simulate these alloy systems with inclusion phases. By testing samples subject to irradiation at several dose and temperature conditions as well as unirradiated samples at different test temperatures, we may achieve a more comprehensive understanding of the mechanical behavior of HT9.

The ACO–3 duct material has been examined previously, but minimal effort was directed toward tying microstructural features directly to changes in mechanical properties. A goal for the study of the ACO–3 duct material is to complement the previous work and help to provide a missing link establishing the relationship between the microstructure and mechanical behavior of this fast-neutron irradiated HT9 material.

The facilities at the Advanced Photon Source (APS) allow for in-situ tensile testing with X-ray diffraction. This allows collection of information about the microstructure before and after deformation occurs, but also during the course of the deformation itself. The point of sample failure is of particular interest, and this setup provides a unique opportunity to observe it.

Chapter 3

Continuous Strain Testing of Unirradiated HT9 at Elevated Temperature

In order to examine the effect of test temperature on the deformation behavior of HT9, miniature tensile samples were strained at constant temperature while X-ray diffraction patterns were recorded to determine their internal lattice strains. Tests were conducted at room temperature, 300 °C, 400 °C, and 500 °C. This temperature set was selected to include the range of irradiation temperatures experienced by the ACO–3 duct material during its irradiation in FFTF and to complement irradiations of HT9 samples conducted at the ATR-NSUF at Idaho National Laboratory. Future Gen-IV reactor designs will require materials to be evaluated at higher temperatures than tested here (in excess of 600 °C) [14]. However, the present study is limited to exploring the behavior in a lower temperature range, with a focus on the difference between more brittle fracture of the steel occurring at lower temperatures and ductile failure at higher temperatures.

This experiment was conducted at sector 1 of the APS (at beamline 1-ID) which has an ideal setup for conducting in-situ tensile tests and XRD characterizations of materials [16]. Beamline 1-ID has been used extensively to conduct a variety of similar material examinations with excellent results. It is equipped with a unique 4-panel (”Hydra”) detector array, allowing for good resolution of full Debye rings from the samples. This experiment captures in detail how each set of grains {hkl} accumulates and subsequently sheds the applied load.

3.1 Experimental Methods

3.1.1 Sample Details

In-situ tensile experiments were conducted on unirradiated HT9 material (heat 9–607) supplied by Oak Ridge National Laboratory (ORNL). The chemical composition analysis of this steel is shown in table 3.1. The material was normalized and tempered with an accepted standard fusion program heat treatment [57]: 30 min at 1050 °C followed by an

Table 3.1: The chemical analysis of heat 9–607 HT9 steel supplied by ORNL.

Chemical Analysis (supplier source/check)														
C	Mn	P	S	Si	Ni	Cr	Mo	Cu	N	Co	Ti	Al	V	W
0.2/0.2	0.52/0.61	0.02/0.016	0.006/0.007	0.22/0.26	0.5/0.54	11.63/11.65	1/1.02	0.04/0.03	0.047/0.041	0.08/0.09	<0/01	<0/01/0.009	0.3/0.29	0.52/0.61

air cool, then 2.5 h at 780 °C followed by an air cool. Miniature tensile samples of "S1" type (colloquially referred to as "dog bone" samples) were cut from the material using electro-discharge machining (EDM). The nominal sample geometry is shown in fig. 3.1; with a gage length of 5 mm, width of 1.2 mm, and thickness of 500 µm. This set of tensile specimens was sliced thinly to allow some to be included in small capsules (with limited space) for irradiation in the Advanced Test Reactor at Idaho National Lab (ATR–NSUF, or ATR). Those samples were irradiated in ATR with an experimental matrix of irradiation temperatures including 300 °C, 450 °C and 550 °C and doses of 0.01 dpa, 0.1 dpa, 0.5 dpa, 1 dpa, 5 dpa and 10 dpa. At the time of this writing, they are still considered too hot for testing at APS, but they will be ideal for complementary study once they have lower activity.

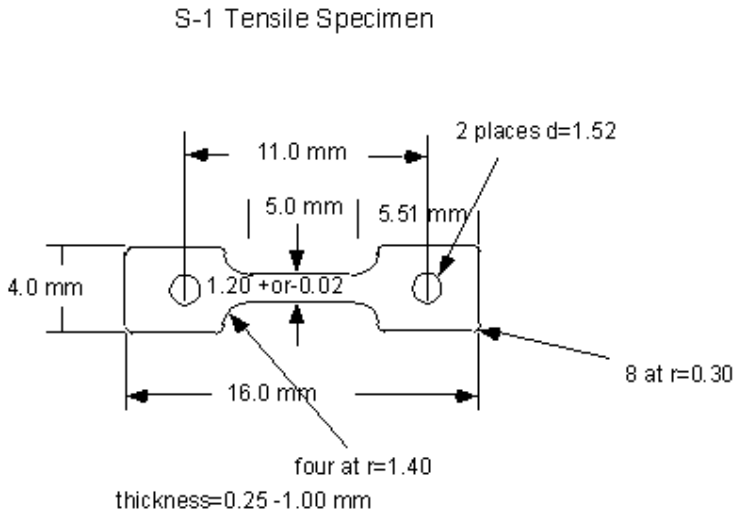

Figure 3.1: Dimensions of the "S1" type miniature tensile specimen.

3.1.2 Test Conditions

Uniaxial static tensile tests to failure were conducted in air while recording high-energy X-ray diffraction patterns throughout the deformation. The tensile samples contained holes at each shoulder (tab end) of the specimen, shown in fig. 3.1, through which pins were inserted to hold and transfer load to the specimen. Samples were tested in an MTS

closed-loop servo-hydraulic test frame with furnace-type induction heater and deformed under displacement control. They were held vertically and strained to failure with a constant crosshead speed of 0.001 mm/s, resulting in a constant strain rate of 2×10^{-4}/s. The induction furnace used in this set of experiments was very stable; test temperatures of 300 °C, 400 °C and 500 °C were easily achieved and maintained. To begin each test, samples were pinned into holding grips attached to the load frame, thermocouples attached, and a small load (20 N) was placed on the specimen to ensure it was secure. For the high temperature tests, the furnace was put in place around the sample and covered by insulation. The furnace was then turned on to heat the sample, and the temperature was allowed to stabilize at the target temperature for ~10 min before starting continuous strain tensile testing. Pictures of the experimental setup inside the hatch at sector 1-ID are shown in fig. 3.2.

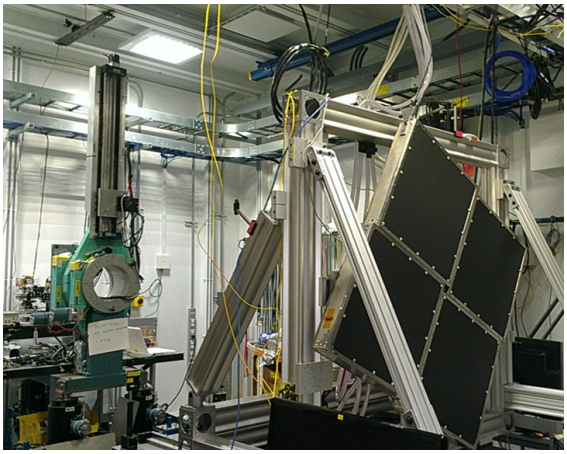

(a) The hydra detector array in the hatch at sector 1-ID, comprised of 4 GE detectors.

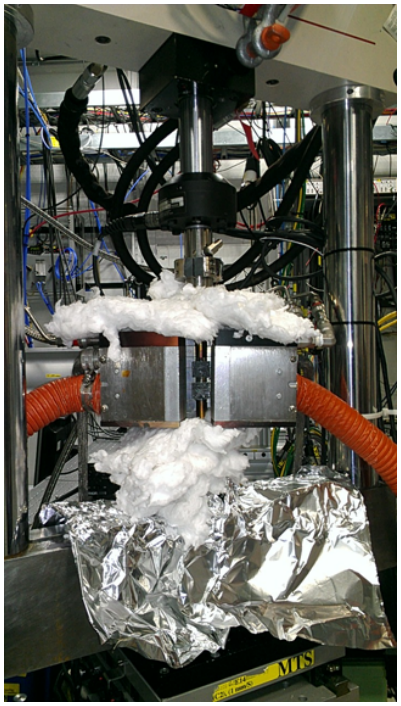

(b) A sample loaded in the MTS load frame with the furnace plates in place on either side. Some of the insulation has been put in place above and below the furnace.

Figure 3.2: Pictures of the setup for the in-situ, continuous strain, elevated temperature XRD experiment at sector 1-ID.

The engineering strain, ε_e, is calculated as the relative displacement (change in gage length) divided by the original gage length:

$$\varepsilon_e = \frac{\Delta L}{L_0} \tag{3.1}$$

where ΔL is the change in gage length, which we measure directly by the difference in displacement given by the load frame, and L_0 is the gage length of the sample prior to deformation (in this case, 5 mm, shown in fig. 3.1). The engineering stress, σ_e, was calculated directly from the load cell by:

$$\sigma_e = \frac{F}{A} \tag{3.2}$$

where F is the force measured directly by the MTS load frame and A is the cross-sectional area of the gage portion of the sample. The thickness and width of the gage were measured with calipers prior to load testing to ensure using an accurate cross-sectional area calculation. Because there is some error inherent in the EDM shape cutting and slicing process, we measured thickness variation of $\sim \pm 10\,\%$ across the sample set.

The APS synchrotron X-ray was filtered with a Si(111) monochromator to give a monochromatic beam, and the beam size was tuned with defining slits. Diffraction measurements were taken with the resulting monochromatic 70 keV ($\lambda = 0.177$ Å) X-ray beam impinging on the gage area of the sample. The incident beam size was approximately 100×100 μm^2. The Debye diffraction rings from the ferrite and the carbide precipitates contained in the diffraction volume were recorded on a 4-panel set of GE41RT area detectors (known as the "Hydra"), each measuring 41 cm $\times$ 41 cm and composed of a 2048×2048 array of 200 μm pixels. A schematic of the beam line for the experiment is shown in fig. 3.3.

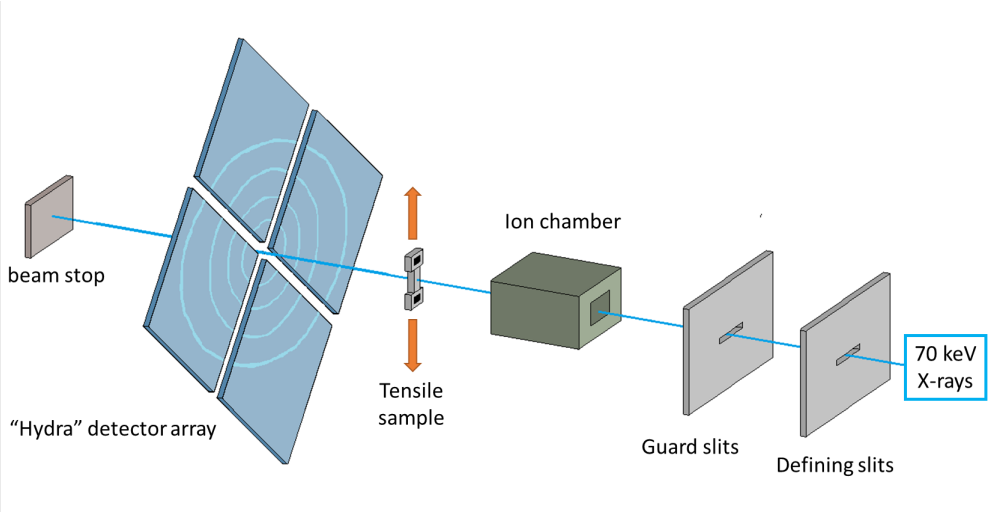

Figure 3.3: Schematic of the diffraction setup for the continuous strain experiment at beamline 1-ID.

3.2 X-ray Diffraction Analysis for Determination of Phase Strain and Stress

When a load is applied to the sample, the originally circular diffraction rings become ellipsoidal. With tensile strain, the rings become narrower in the direction of loading and wider in the transverse direction, see fig. 3.4. Recall that the distance between the center and diffracted intensity ring on the detector has an inverse relationship to the interplanar d-spacing, by eq. (2.1). Therefore as the interplanar spacings in the loading direction increase, the diffraction angle 2θ decreases. The reverse is true for the transverse direction. The changes in the shape of the rings are used to determine the internal lattice strain in the material.

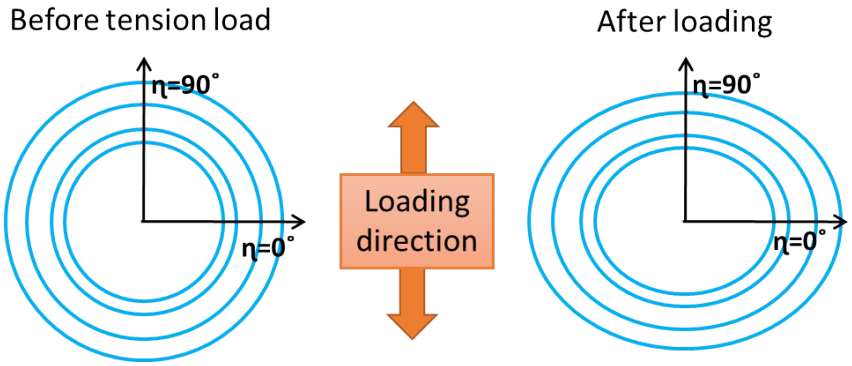

Figure 3.4: An illustration of the change in shape of Debye diffraction rings with sample tensile loading, where η is the azimuthal angle about the axis of the incident beam.

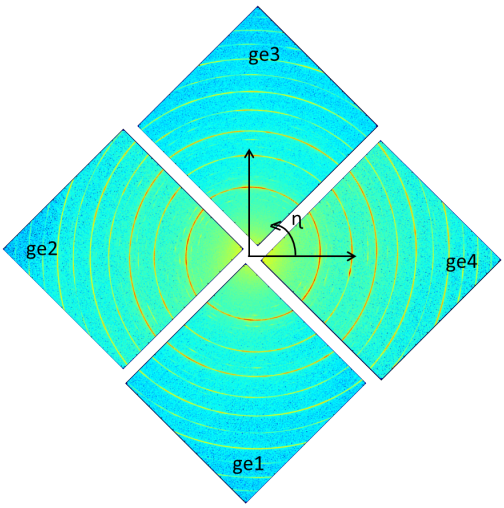

Figure 3.5: A representative diffraction pattern collected on the 4-panel "hydra" detector; η denotes the azimuthal angle of diffraction about the beam axis. This pattern was collected from an HT9 sample heated to 300 °C prior to loading.

Figure 3.5 shows a diffraction pattern collected on the "Hydra" detector array prior to sample deformation. The patterns collected on the detectors were transformed into one-dimensional diffraction line profiles (in Intensity vs 2θ) by integrating over a 20° azimuthal range centered about each of the axial/tensile (vertical) and transverse (horizontal) directions. For the hydra 4-panel array, the azimuthal range representing each direction is captured on a different detector, as shown in fig. 3.5. Because of the high X-ray beam energy and the resulting low diffraction angle, the diffraction vectors Q are nearly normal to the incident beam. Therefore, to good approximation, the diffraction vectors $Q_{\parallel}$ corresponding to the profiles representing 20° integration centered about azimuthal angles $\eta = 90°$ and $\eta = 270°$ (shown vertically in fig. 3.5) are parallel to the loading (axial) direction, and those diffraction vectors $Q_{\perp}$ corresponding to integration about $\eta = 0°$ and $\eta = 180°$ (the horizontal in fig. 3.5) are transverse to the loading direction.

The MATLAB script developed by Almer and Mo [58] was used to view the raw diffraction pattern collected on the detector, view the transform of that pattern, and then to generate the integrated line profiles about η = 0°, 90°, 180° and 270° for each diffraction pattern captured during the deformation. Figure 3.6 illustrates the output after each of the aforementioned steps.

The script was used to apply a pseudo-Voigt single peak fitting routine to each of 7 ferrite and 3 carbide peaks found in the diffraction line profile for each time step throughout the deformation. The X-rays counted in a particular diffraction peak (hkl) are diffracted from a set of grains defined by a specific plane normal (hkl) parallel to

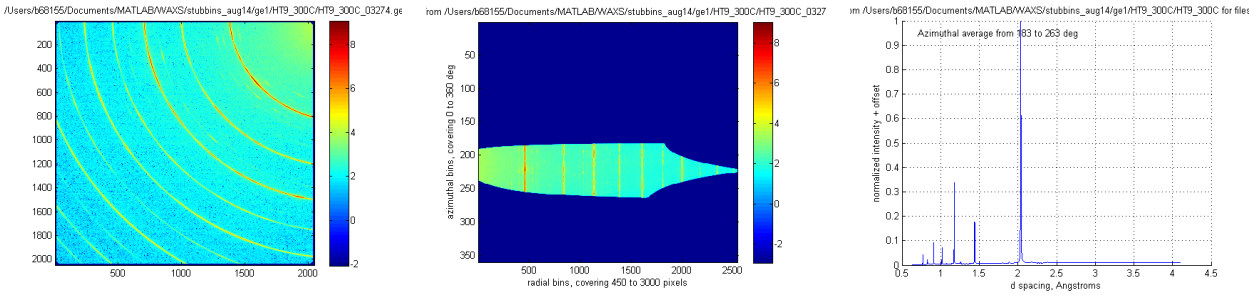

(a) The raw diffraction pattern captured on a single detector panel, ge1.

(b) The transform of the diffraction pattern on detector ge1.

(c) The integrated diffraction line profile from the pattern on ge1.

Figure 3.6: Steps taken in the MATLAB code to create line profiles, performed in sequence from left to right. The example difraction pattern came from HT9 heated to 300 °C prior to straining.

the diffraction vector. The evolution of a particular peak, by e.g. changes in its position (d-space) or width over the course of the deformation, represents the evolution of that particular set of grains. Figure 3.7 shows a ferrite peak that was fitted with a pseudo-Voigt function using the MATLAB fitting routine. The fitting parameters of each peak (most importantly, the peak center position and width) were written to a text file for use in line profile analysis.

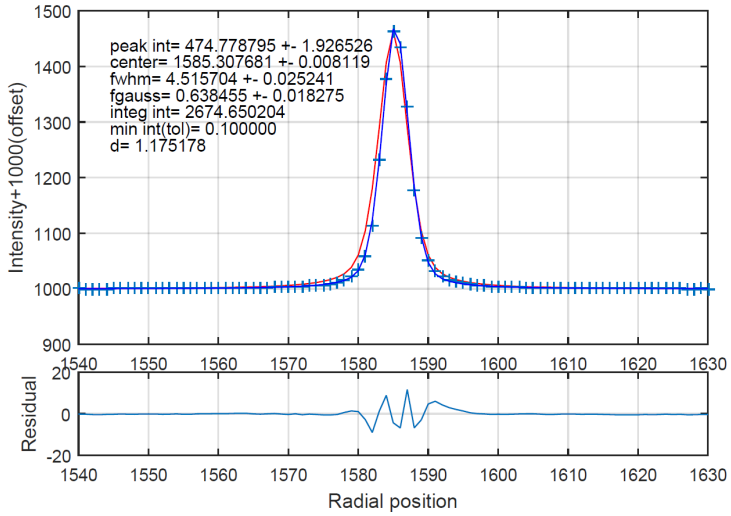

Figure 3.7: The (211) ferrite peak, in blue, shown with the peak generated by fitting it singly with a pseudo-Voigt function, in red. For diffraction line profile analysis, the center location of the fitted peak in 2θ is used to calculate the associated d-spacing of the peak by eq. (2.1).

The shift in peak position (lattice spacing) with applied loads was then used to compute the internal lattice strains for (hkl) sets of grains in both the ferrite and carbide phases of

the material using eq. (3.3):

$$\varepsilon = \frac{(d - d_0)}{d_0} \tag{3.3}$$

where d refers to the interplanar spacing of a particular set of lattice planes (d_{hkl}), or can refer to the lattice parameter, a. Strains calculated from single peak fits will be referred to as hkl-specific, or orientation dependent, strains. Those calculated from the lattice parameter, a, will be referred to as phase strains. Note that d_0 is taken to be the linear extrapolation of the lattice spacing in the elastic region to zero stress. This ignores the fact that there will be pre-existing thermal stresses in each phase due to the mismatch in coefficient of thermal expansion.

It is assumed that the lattice strains in a grain set (hkl) or phase represent the response of that group of oriented grains or phase, and thus the internal hkl-specific and/or phase stresses are calculated in the axial direction using the generalized Hooke's law:

$$\sigma_{11} = \frac{E}{1+\nu}\varepsilon_{11} + \frac{\nu E}{(1+\nu)(1-2\nu)}\left(\varepsilon_{11} + \varepsilon_{22} + \varepsilon_{33}\right) \tag{3.4}$$

where the subscript '11' refers to the axial direction and the subscripts '22' and '33' refer to each of two transverse directions. Symmetry is assumed in the transverse directions ($\varepsilon_{22} = \varepsilon_{33}$) and the transverse stresses calculated from the proper permutations of indices. Poisson's ratio for both phases is taken to be $\nu = 0.3$, the modulus of $E_{ferrite} = 208\,\text{GPa}$, and $E_{carbide} = 330\,\text{GPa}$ [59, 60]. The average Von-Mises effective stress at yield can then be calculated for each phase by:

$$\sigma_{eff} = \sqrt{\frac{(\sigma_{11} - \sigma_{22})^2 + (\sigma_{22} - \sigma_{33})^2 + (\sigma_{33} - \sigma_{11})^2}{2}} \tag{3.5}$$

3.3 Results

The macroscopic stress-strain curves of the HT9 material strained continuously at elevated temperature are shown in fig. 3.8. The samples tested at room temperature and at 300 °C have virtually the same stress-strain curve (within a margin of error). As expected, the strength of the material is lower at higher testing temperatures. The sample tested at 500 °C shows the most ductility (a total elongation of 20%), but compromised strength. The shape of the 500 °C curve is notably different from the others, which all show significant strain hardening during plastic deformation. The 500 °C test shows the onset

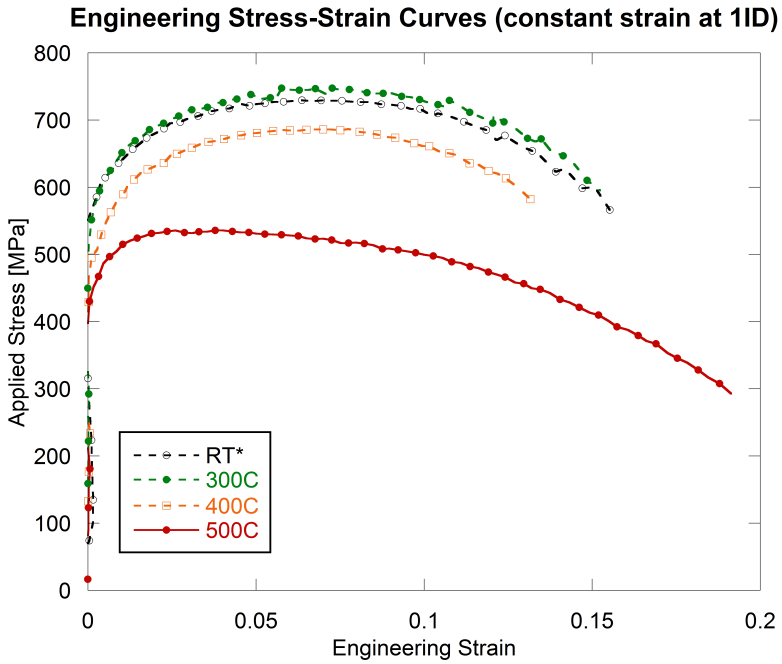

Figure 3.8: Macroscopic Stress-Strain curves for load tests conducted on unirradiated HT9 with constant, continuous strain at elevated temperatures. *Note the RT data included here was collected on the same beamline on a sample from the same set, but was part of another experiment on a different day; there were slight variations in the geometry of the experimental setup.

of necking at only ~3 % strain, whereas the samples tested at lower temperatures do not reach their ultimate tensile strength and begin necking until reaching ~7 % strain. The material strength properties at each test temperature are shown in fig. 3.9a: Yield Strength (YS), Ultimate Tensile Strength (UTS), and Failure Strength (FS). These values were estimated based on the macroscopic strain curves displayed in fig. 3.8 and represent the magnitude of the applied stress at the point of 0.2% engineering strain, at maximum stress, and at the point of sample failure, respectively. Shown in fig. 3.9b are the uniform elongation and total elongation at each sample test temperature. Also include are the values found in the experiments by Roy, performed on larger tensile samples at 10× the strain rate in a nitrogen atmosphere [32].

The tests performed by Roy at elevated temperatures showed similar dependencies of strength and ductility properties on test temperature [32], but measured greater strength and superior ductility. The body of existing literature contains a large range of quoted yield strengths for HT9 tested at room temperature. Unfortunately, the details of the material used in each test (heat number, production source, thermo-mechanical treatment

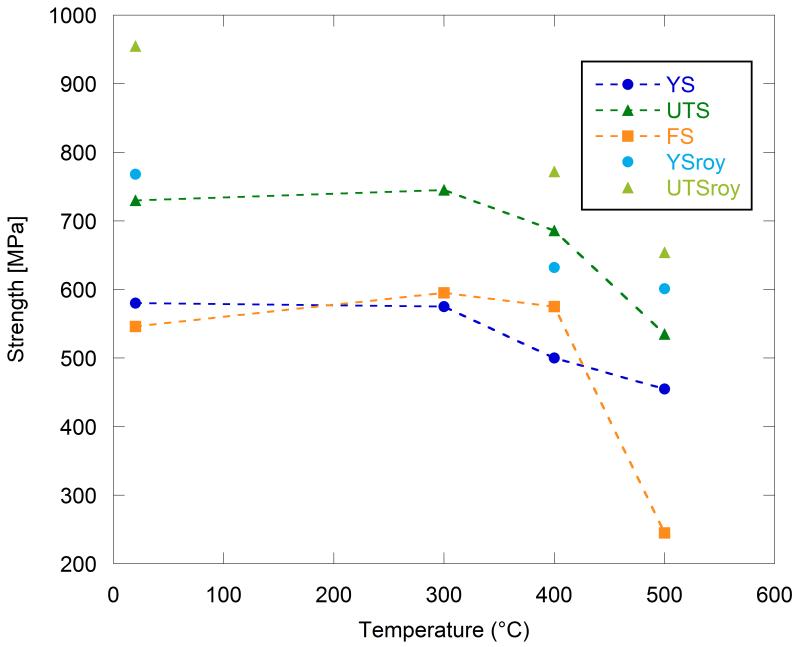

(a) Macroscopic mechanical properties plotted as a function of test temperature. Here YS refers to the 0.2% offset yield strength, UTS to the ultimate tensile strength, and FS to the failure strength.

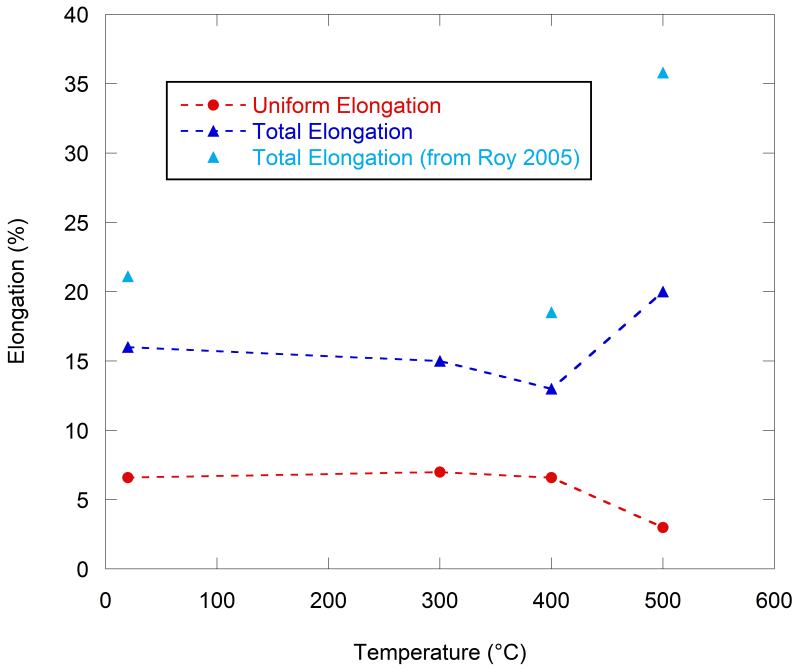

(b) Percent elongation as a function of test temperature for continuous strain tensile tests.

Figure 3.9: Macroscopic properties calculated based on the engineering-stress strain curves for continuous strain tensile tests performed at elevated temperatures. Properties of a different laboratory heat of HT9 measured by Roy are also include for comparison [32].

details) are not always available. The values for YS shown in fig. 3.9a compare well with previous studies, which is predictable, considering the enormous range of quoted values (between ~450 MPa and 780 MPa) [11, 44, 61–63]. Fewer tests have been conducted at elevated temperatures, but the high temperature results in fig. 3.9 agree reasonably well with those by Maloy, shown in fig. 3.10 [11, 45].

One reason for the wide range of quoted yield strengths is that the microstructure of HT9 varies greatly depending on the heat treatment received by the sample prior to testing. It is likely that the heat treatment and production processes of the HT9 used in the tests by Roy resulted in different microstructures leading to the difference in mechanical properties. Different heat treatments (including quenching and tempering times) can produce varying percentages of retained delta-ferrite, as well as different size and shape of martensite laths. The grain sizes, precipitate sizes, and phase distribution within the material can also vary with thermo-mechanical treatment. Therefore, comparisons in mechanical property values made between distinct tests (performed on material from different suppliers with sometimes unknown heat treatment conditions and uncharacterized microstructures) must be made with this in mind.

A full X-ray diffraction spectra prior to deformation of an HT9 sample is shown in fig. 3.11. At all temperatures (RT, 300 °C, 400 °C, and 500 °C) both before and after deformation, peaks found in the spectra were attributable to either the bcc ferrite phase or the carbide precipitates $Cr_{23}C_6$; carbide peaks were indexed using pdfcard #35-0783.

3.3.1 Lattice Strains

Figure 3.12 shows hkl-specific lattice strains, ε_{hkl}, for the ferrite and carbide phases in the HT9 material as a function of applied stress at the four chosen test temperatures. The blue symbols represent the ferrite response and the red the carbide. The response in the axial (loading) direction (developing positive strain) is indicated with solid symbols and the transverse direction (developing negative strain) with open symbols. The ferrite elastic response is predictably anisotropic, with the (200) grains having the lowest effective modulus of elasticity, followed by (310). The remainder of the tracked ferrite grains ((110), (211), (220), (222), and (321)) show approximately the same and higher effective moduli of elasticity. Ferrite is known to be elastically anisotropic, and the standard values for the iron crystal stiffness matrix ($S_{11} = 0.8, S_{12} = -.28, S_{44} = 0.86$) support the measured anisotropy, indicating the crystal is most compliant along the (100) and stiffest along the (111) plane normal direction (using either the Reuss or Kroner model [64]). The

elevated temperature results here, however, do not show as distinct a difference in the stiffness between the ⟨111⟩ and ⟨110⟩ directions as the stiffness matrix indicates. Elastic anisotropy of the ferrite persists at all test temperatures. The carbide elastic response is isotropic and roughly the same as the ferrite (110) and (211) grain sets, which are often used as representations of the whole ferrite matrix phase. Note that for the room temperature sample, the carbide peaks were particularly difficult to resolve, and there is substantial uncertainty in values of d_{420} and d_{422} (d_{440} could not be tracked). Because of the uncertainty in these values for the room temperature carbide peaks, extrapolation and estimation of the initial d_0 value for the carbide grains was extremely rough. The perceived anisotropic response of the carbide elastic region in the room temperature test case is most likely a result of large errors in peak parameters for the carbide peaks. Other tensile tests performed on HT9 at room temperature showed an elastically isotropic carbide response (refer to fig. 5.4 for an example).

The ferrite response following elastic deformation can be broken into 2 regions. The first region begins when the ferrite yields and the experimentally measured ferrite lattice strains either saturate or nearly saturate such that further increases in the applied load and imposed macroscopic strain have a reduced effect on the lattice strain (seen as the slope of blue lines in the plots becoming more vertical). This indicates the onset of plastic deformation in the matrix phase. The second region begins when the slope of the blue ferrite phase curve decreases again as the ferrite accumulates more elastic strain, indicating hardening. The plot for the room temperature sample shows an additional downturn of the ferrite response curve after the maximum applied stress is reached - this indicates that we diffraction sampled the necking region of the gage. It is difficult to capture the necking region of every sample, since the likelihood of sampling it with a small beam cross sectional area is relatively slim. Particularly in these miniature tensile samples, necking and fracture doesn't necessarily occur at the midpoint of the gage length; it is impossible to determine in advance of the test where the necking will occur. Taking many diffraction patterns along the length of the gage at each strain step can better ensure sampling both the necked and unnecked regions of the sample (as in [58]), but it also necessitates a much longer experiment run time.

The carbide phase response is difficult to present because the peaks were poorly resolved. While efforts were made to track 3 carbide peaks that were initially visible in the diffraction pattern ((420), (422), and (440)), the limited (20°) range of integration of the intensity rings about each azimuthal angle η combined with the low intensity of the carbide peaks relative to the background often made the peak shape difficult to resolve. The carbide stress-lattice strain curves are shown only for the grain sets and

directions that presented reasonably convincing and resolvable peaks. Even in the best cases, the carbide data had considerable noise owing to the poorly resolved peak shapes, and what is presented in the curves in fig. 3.12 is a 5-8 point smoothing of the carbide data. The high uncertainty of the carbide data aside, there appears to be a difference in carbide response between the highest temperature test (at 500 °C) and the others. The high temperature test appears to show the (422) and (440) carbide grains unloading early, at nearly the same strain as the ferrite (200) grains, while the (420) accumulated a lattice strain up to .008, consistent with the lower temperature tests. This anisotropy of the carbide phase, however, is only seen in the axial direction; the carbide transverse response appears isotropic.

Figure 3.13 shows another (closer) look at the accumulation of lattice strain in a few representative ferrite grains. Recall we are using the (211) peak to provide an estimate of the overall phase response. The slope of the saturating strain region, the first plastic deformation region described, decreases with increasing test temperature. That is, there is more complete saturation of the ferrite strain in tests performed at lower temperatures. The hardening region (after the curve turns over again) shows the most hardening in the room temperature test, and progressively less hardening with increasing test temperature. There is no discernible ferrite strain hardening in the highest temperature test. The elastic response of the ferrite is clearly anisotropic, as mentioned previously, and while the stresses at points of transition between the plastic deformation regimes are the same for each set of grains (hkl), there is some anisotropy with in the rate of strain accumulation and the degree of strain saturation, evidenced by slight differences in the slope of the curves within each of regime.

The stress at the transition points between the plastic deformation regimes of the ferrite are plotted as a function of test temperature in fig. 3.14. The stresses at these points decrease with increasing test temperature. Tests at room temperature through 400 °C show the saturation region (the difference in stress between the strain saturation and hardening points) grows larger with increasing temperature. At 500 °C, there is little to no hardening in the ferrite phase, and no strain hardening transition point can be discerned.

3.3.2 Phase Stresses

Estimated axial phase stresses calculated by eq. (3.4) for the ferrite and carbide phases are presented in fig. 3.15 for HT9 tested with continuous straining at 300 °C, 400 °C, and

500 °C. In this estimation, the (211) ferrite grains are considered representative of the entire ferrite matrix phase, and the (420) carbide grains are considered to represent the behavior of the whole carbide phase.

There is considerable noise in the stress estimates, stemming from limited peak tracking in the transverse direction. It is clear, however, that the mechanical behavior of the ferrite phase in the 500 °C sample is fundamentally different from that in the 300 °C and 400 °C tests. The stress development in the 300 °C and 400 °C samples appears to be the same, within the margin of error. The ferrite phase stress at yield is approximately 510 MPa regardless of test temperature, increasing to only 540 MPa for the 300 °C test. However, the maximum stress in the ferrite phase is considerably lower for the highest temperature test, only reaching 590 MPa. The 300 °C and 400 °C tests show a maximum ferrite phase stress of 735 MPa and 800 MPa, respectively. Considering the noise in these plots, the ferrite phase maximum stress in the two lower temperature tests can be considered roughly the same, ~30% higher than for the 500 °C test. Note that at 500 °C, the maximum stress of 590 MPa appears to be slightly higher than the yield strength, indicating some minimal amount of strain hardening persists in the ferrite phase at this temperature.

Discerning differences in the estimated carbide stresses proves more difficult. The carbide stress at yield appears similar at all temperatures, 1600 MPa for the 300 °C and 400 °C tests, reaching 2020 MPa in the 500 °C test. As in the ferrite, the 300 °C and 400 °C maximum stresses in the carbide are quite similar, ~4980 MPa and ~4700 MPa, respectively. The estimated maximum carbide stress in the 500 °C test isn't reached until near the point of failure, and is in the vicinity of 4300 MPa. The 300 °C and 400 °C tests show about 13% more stress accumulation in the carbides than for the 500 °C test. At all test temperatures, the stresses accumulating in the carbide are an order of magnitude higher than those in the ferrite. The variation in test temperature is shown to have a greater impact on the stress accumulation in the ferrite phase than in the carbide phase.

The estimated phase stresses in both the axial/loading and transverse directions are shown plotted together with the macroscopic applied stress in fig. 3.16. This figure serves to illustrate the magnitude of difference between the stresses accumulated in the ferrite and carbide phases. The small volume fraction of carbide phase accumulates a remarkable amount of stress in the loading direction. It also accumulates more stress than the ferrite in the transverse direction, about 6× more at 400 °C and 8× more at 300 °C. However, since the estimated stresses in the transverse direction show the (211) ferrite grains appear to have accumulated positive stress at some points, the transverse phase stresses are uncertain enough that they ought only be used for qualitative comparison with those in the axial direction. The respective transverse phase stresses have the same

relationship to each other as they do in the axial direction, but the magnitude of the accumulated phase stresses is much smaller in the transverse direction. Consideration of the assumed transverse symmetry ($\sigma_{22} = \sigma_{33}$) and the magnitude of difference in the directional stresses ($\sigma_{11} >> \sigma_{22}$) reduces the average Von Mises equivalent stress given by eq. (3.5) to $\sigma_{eff} \approx \sigma_{11}$. In other words, the equivalent effective stress on a phase is approximately equivalent to the axial stress on that phase. Therefore, we will reference computed estimates of the axial stress σ_{11} in discussion of phase stresses.

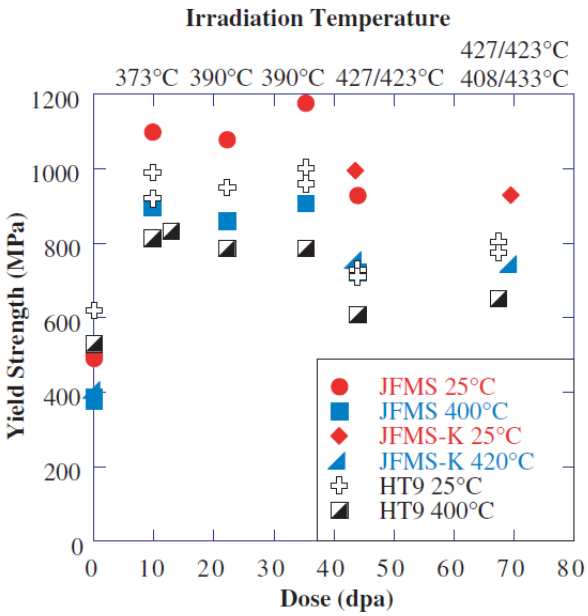

(a) Offset yield strength of HT9, taken from [45]. YS of unirradiated HT9 is shown along the y-axis by the black + and shaded square for room temperature and 400 °C, respectively.

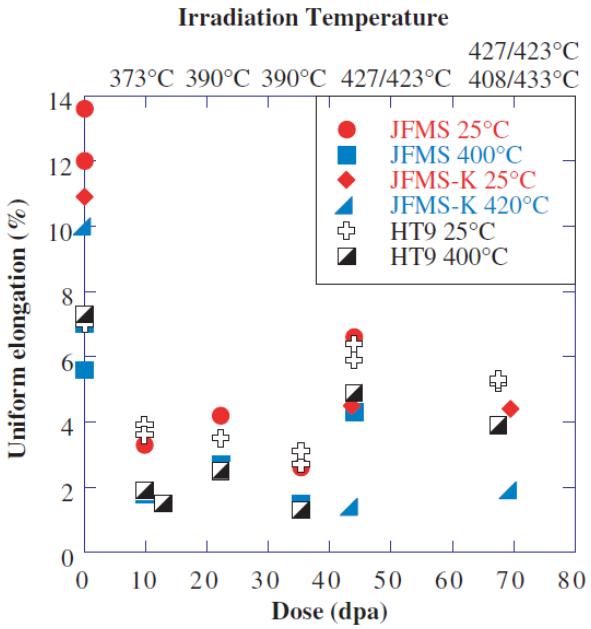

(b) Uniform elongation of HT9, taken from [45]. Uniform elongation of unirradiated HT9 is shown along the y-axis by the black + and shaded square for room temperature and 400 °C tests, respectively.

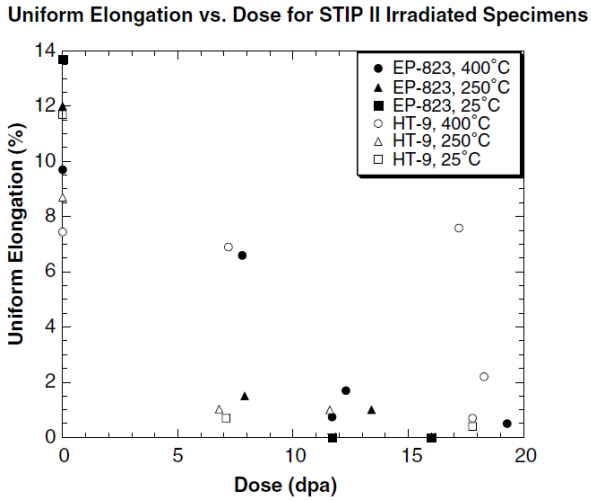

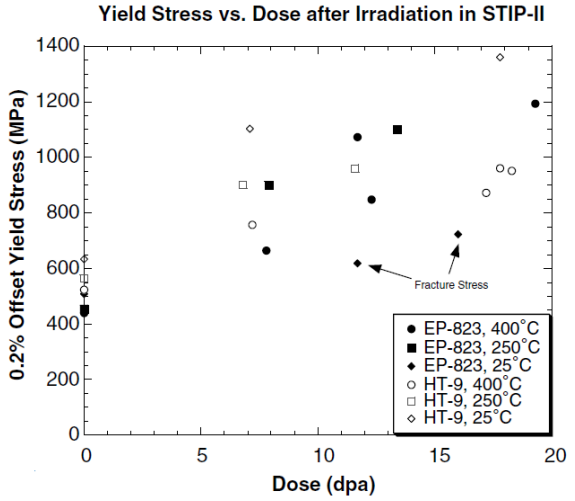

(c) Uniform elongation and offset yield strength of HT9, taken from [11]. Unirradiated HT9 values are shown along the y-axis by open symbols.

Figure 3.10: Mechanical properties of HT9 measured at test temperatures of 25 °C, 250 °C and 400 °C, from [11, 45].

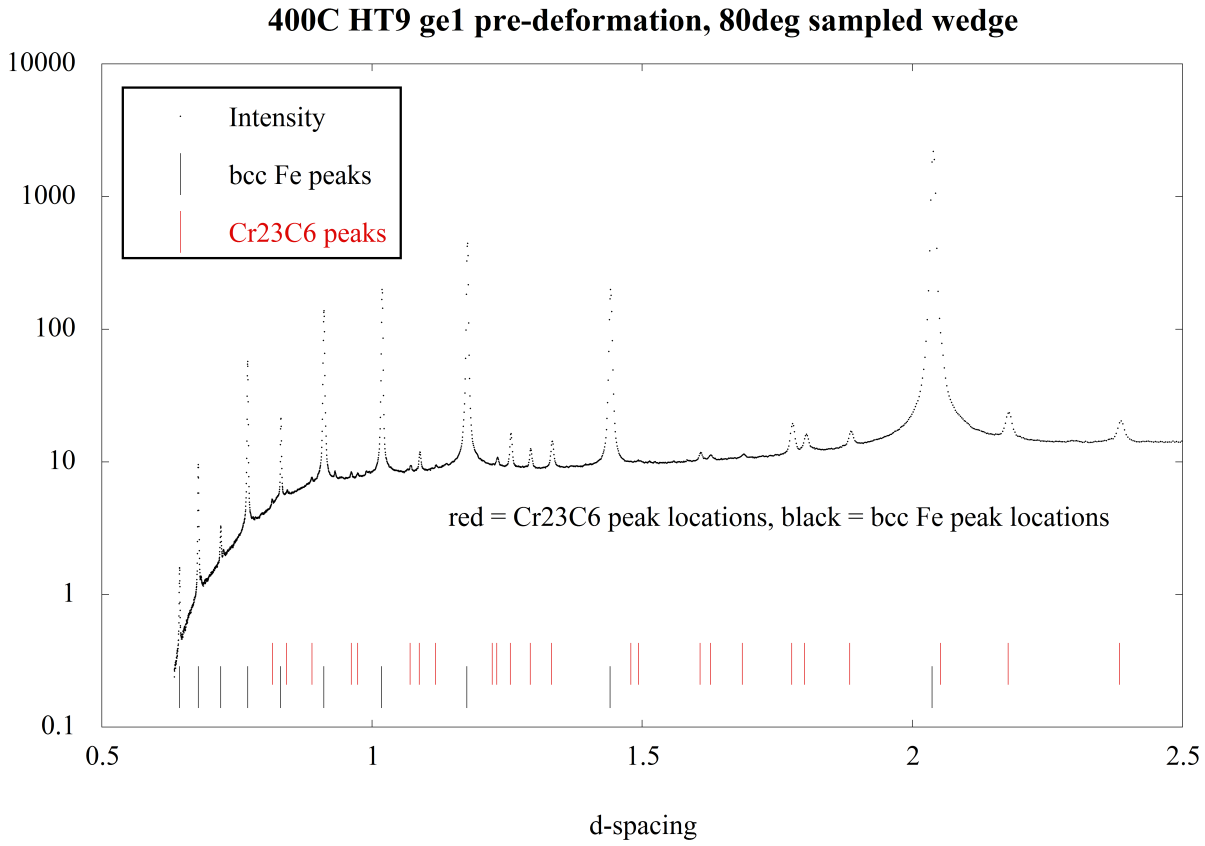

Figure 3.11: The X-ray diffraction spectra, a peak line profile across an 80° azimuthal range, taken from ge1 after HT9 was heated to 400 °C. The hashes along the bottom of the plot indicate the expected location of bcc ferrite phase peaks in black and $Cr_{23}C_6$ carbide precipitate phase in red.

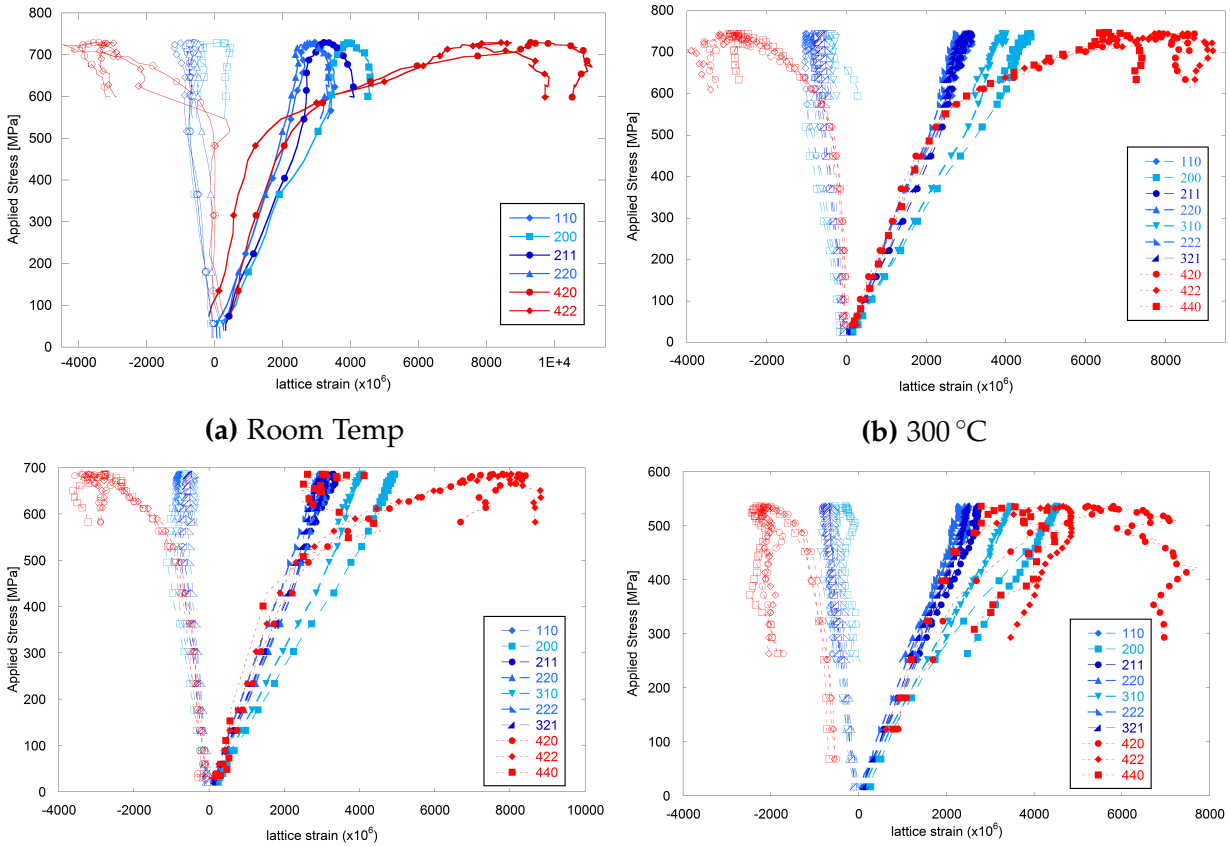

(a) Room Temp

(b) 300 °C

(c) 400 °C

(d) 500 °C

Figure 3.12: Applied Stress vs. lattice strains for the ferrite matrix grains hkl (in shades of blue) and carbides (in red) in HT9 strained at different temperatures. The closed symbols represent the loading direction, the open symbols the transverse direction.

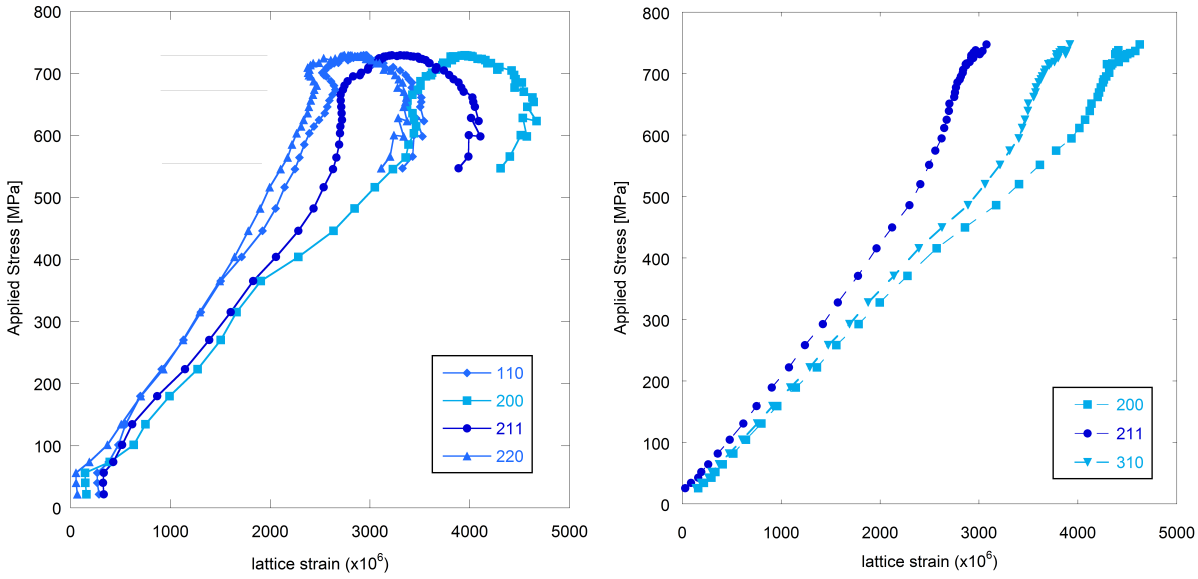

(a) Room Temp

(b) 300 °C

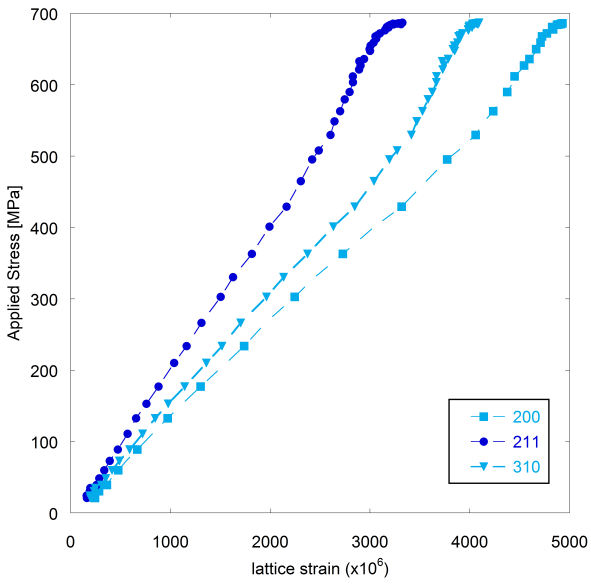

(c) 400 °C

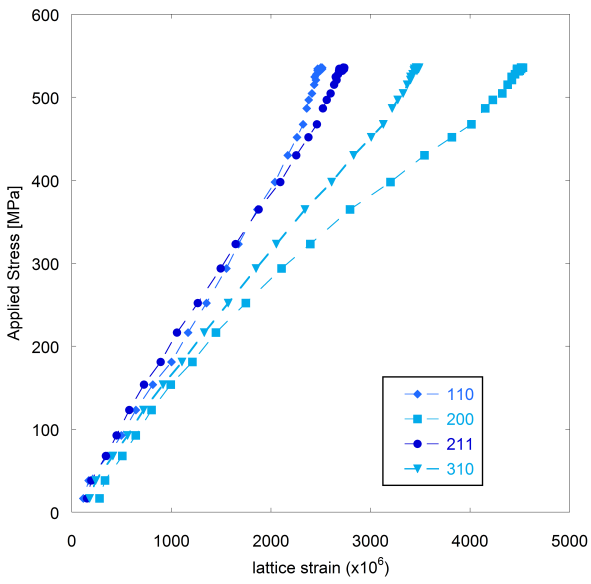

(d) 500 °C

Figure 3.13: Loading behavior of selected ferrite grain orientations in HT9 strained at different temperatures. For clarity, unloading data has been removed.

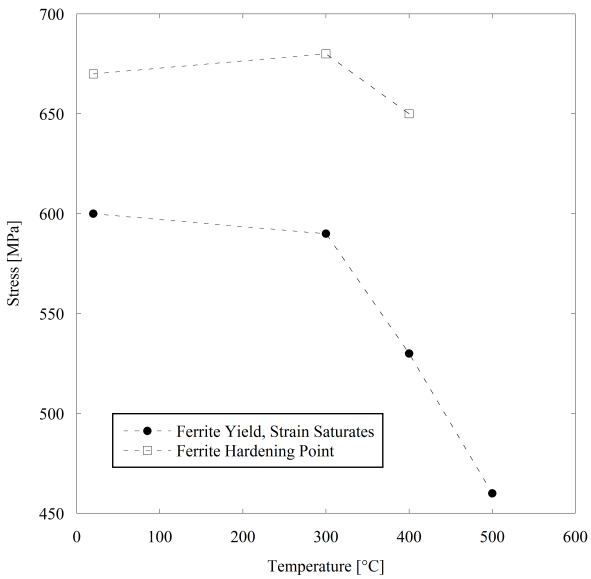

Figure 3.14: The transition point at which the ferrite phase yields and the strain nears saturation (closed circles) and the transition point at which the ferrite phase again accumulates strain indicating hardening (open squares) are plotted as a function of test temperature.

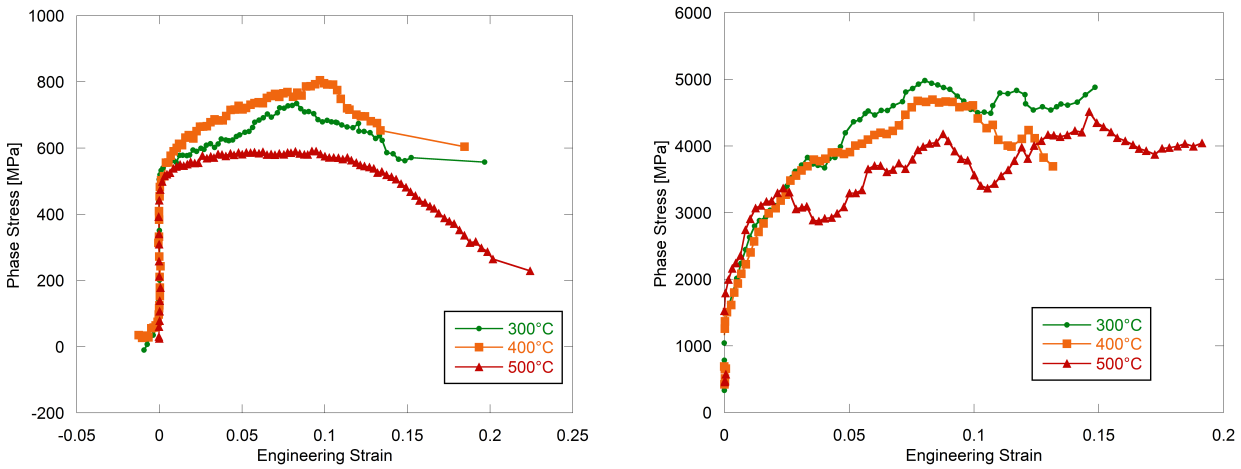

(a) Ferrite Matrix **(b)** Carbide Precipitate

Figure 3.15: Estimated phase stresses (in the loading direction) in each of the constituent phases of the HT9 material, using the (211) grains to represent the ferrite and the (420) the carbide phase.

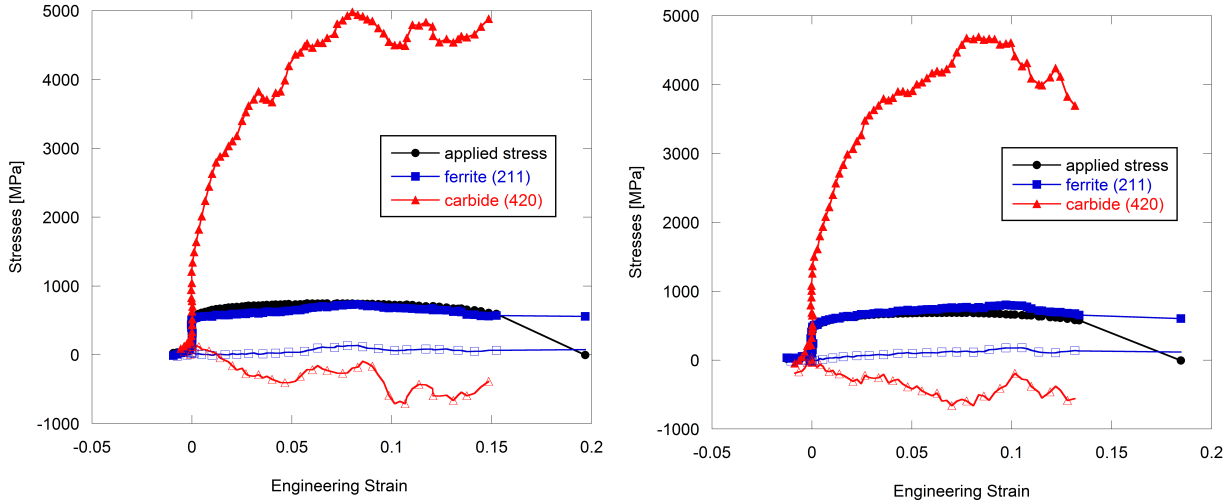

(a) 300 °C **(b)** 400 °C

Figure 3.16: A comparison of the stress development in each constituent phase of the HT9 material, where the ferrite response is approximated by the (211) grains, shown in blue, and the carbide by the (420), shown in red. Closed symbols show the stresses in the axial direction, open symbols show the transverse direction.

Chapter 4

Stepwise Straining of Unirradiated HT9 at Elevated Temperature

The 1-ID beamline sees a vast number of users every year, and rarely is the allotted time for any one group enough to conduct all proposed experiments (or to perform repeat testing). In addition, the beamline is not at present particularly well equipped to handle hot samples. They can be tension tested in situ, but require (as they would at any APS beamline) double encapsulation of the hot material. Because the hydraulic load frame at 1-ID is not designated as hot and therefore can not be contaminated, the prescribed containment layer needs to come between the body of the load frame and the sample. This necessitates building a flexible containment attached to loading grips that accommodates the elongation of the sample with deformation. Not only is this a tedious setup, but this containment causes sufficient background scattering that can obscure the weak peaks from minor inclusion phases (like carbides) in the diffraction pattern. The following set of experiments explored performing a similar test to that detailed in section 3.1.2 on an alternate beamline at the APS: sector 10, MRCAT. This beamline is the proposed location for ultimately examining the samples that have been irradiated in the ATR. The experiment described in this section was part of the first set of tensile tests done with a newly-designed portable, fully contained loading stage intended for future testing of hot samples. The MRCAT does not have a 4–panel detector array, so the highest resolution plate detector available was used. The trade for this high resolution detector was the requirement of a long data collection time. The detector read-out time (combined with the limited displacement rate of the loading stage) was such that the time between collecting diffraction patterns was ~2 min. The long time step between data collection points meant continuous deformation of the sample was unsuitable. The samples were instead strained in steps, and held at constant displacement during collection of diffraction data.

When designing this experiment, test temperatures were chosen to add to the discussion of the material behavior dependence on a threshold irradiation temperature near $0.3T_m$, where T_m is the melting point [41, 42, 45]. In executing the experiment, however, the maximum achievable temperature was lower than planned. A control test was conducted at room temperature; elevated temperature tests were conducted near 300 °C and 410 °C,

close to the irradiation temperature of some of the ACO–3 duct samples. Single peak fitting of multiple ferrite and carbide peaks was completed using the same MATLAB subroutine detailed in Chapter 3. The dislocation density evolution within each sample was estimated using the modified Williamson-Hall method [55].

4.1 Experimental Methodology

4.1.1 Modular Load Testing Environment

In-situ tensile experiments were conducted on the same unirradiated HT9 material described in section 3.1.1, heat 9–607 from ORNL, cut into miniature tensile specimens 500 µm thick. Specimens were held in place on the loading stage by pins inserted through the holes in each shoulder of the sample. The miniature tensile samples were strained in a Deben leadscrew tensile testing stage designed for use in XRD experiments and associated environments, shown in fig. 4.1. The stage includes a 5 kN loadcell and can be used at temperatures up to 550 °C. It was equipped with a Deben microtest stage controller which was used for remote control of the stepwise loading. The loading stage is relatively compact, measuring approximately $30 \times 15 \times 5$ cm. Its modest size allowed it to be mounted atop rotation and displacement stages all housed completely inside a containment glovebox, seen in fig. 4.2. Once this portable module is completed and approved for in-situ tensile testing of hot samples at the APS, it can be used to examine future irradiated samples (most importantly, those from the ATR irradiations) without exposing the APS beamline hatches to contamination.

4.1.2 Test Conditions

Tensile deformations of HT9 were conducted with intermittent collection of X-ray diffraction patterns at room temperature, 300 °C, and ~410 °C. As in the continuous strain tests, samples were strained vertically in air to the point of failure. Unlike the continuous strain tests at 1-ID, the loading procedure applied displacements of 0.01 mm to 0.02 mm in steps. Small displacement increments were used in the elastic region to ensure capturing diffraction information at the yield point, and larger increments were used after yield to minimize the time required for each test. The maximum displacement rate of the loading stage, 1.5 mm/min, was used to apply each displacement step. The maximum

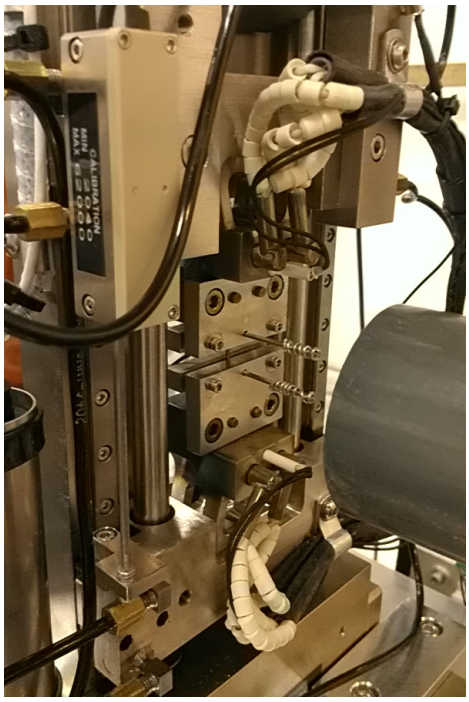

Figure 4.1: Deben 5 kN Leadscrew tensile testing stage equipped with grips, the sample held in place by pins.

speed of the stage corresponded to a strain rate of 5×10^{-3}/s, an order of magnitude higher than for the continuous strain test. Once the designated step displacement was reached, the sample was held at constant displacement for roughly 2 minutes to allow the detector image to be captured and saved before the next incremental displacement was applied. The approximate overall deformation rate of each sample, considering that one displacement step was taken about every 2 minutes, was 2×10^{-5}/s to 8×10^{-5}/s.

The sample strained at room temperature was measured using a 30 keV beam with a cross section of 400×400 µm^2 and was tested under load control. This choice of control mode turned out to be problematic; it led to grossly inaccurate macroscopic strain measurements, which will be discussed in section 4.3. The high temperature tests implemented a conduction heater and control unit with integrated cooling. The thermocouple used to determine sample temperature was attached at the base of the gage area of the sample, see fig. 4.3. This was necessary to prevent the thermocouple wire contributing intensity rings (fcc Ni) to the diffraction pattern. This thermocouple placement led to some uncertainty in the test temperature of the sampled portion of the specimen gage. The high temperature tests showed significant instability in sample temperature during the deformation. Despite stability of the elevated temperatures prior to the start of each tensile test, the measured sample temperature decreased throughout

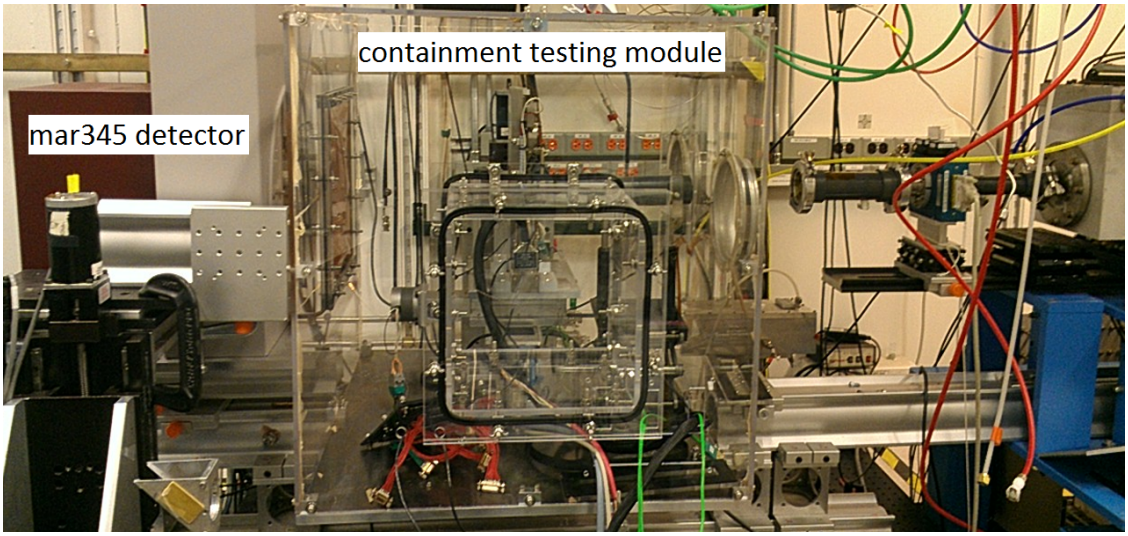

Figure 4.2: A picture of the experimental setup at the MRCAT beamline. Pictured at the center is the portable hot tensile testing module, containing the tensile testing stage, rotation stage, displacement stages, and inlets for coolant water and control cables. Gloves mounted in the ports on the right hand side of the box will be used to manipulate the samples during hot sample testing. To the right of the containment box is the ion chamber, immediately to the left is the Mar345 detector.

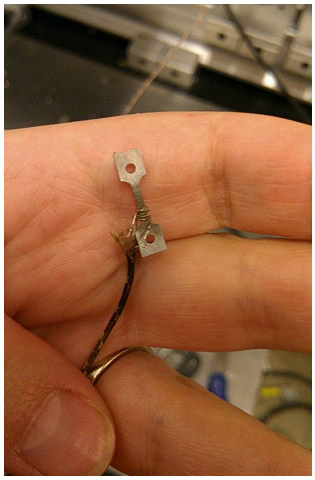

Figure 4.3: Thermocouple wire wrapped around the base of the gage section of the miniature tensile sample before loading in the test frame.

the course of the deformation. The high temperature samples were measured with a higher energy 50 keV beam of the same 400×400 μm^2 size and tested under displacement (strain) control. This control mode was significantly more reliable for the screw-driven tensile stage. A Mar345 (345 mm diameter image plate) detector with a pixel size of 100×100 μm^2 was used for superior peak resolution, but significant time was required for transfer of the diffraction data from this large detector to computer storage after

each image was collected. A simplified schematic of the experiment setup appears in fig. 4.4. Notice in fig. 4.2 that in order to maximize the number of ferrite diffraction peaks captured (by minimizing the sample-to-detector distance), the Mar345 detector (the large burgundy and beige box) was placed as close as possible to the back of the containment box.

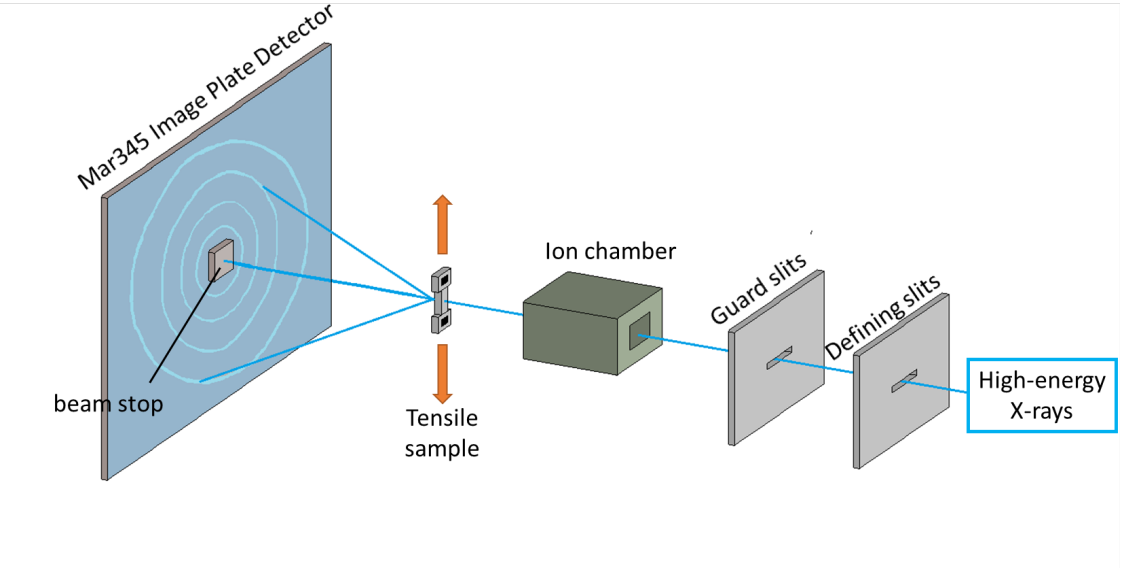

Figure 4.4: A schematic of the experimental setup for stepwise strain tests at the sector 10 MRCAT beamline.

This pilot set of experiments with the modular test unit had significant limitations. Because the irradiated ACO–3 material exhibited mechanical behaviors in two distinct regimes with a threshold irradiation temperature in the vicinity of 430 °C, this experimental plan aimed to test samples at temperatures both below and definitively above this threshold for comparison with the ACO–3 samples exposed to similar operating temperatures. Unfortunately, this was not possible. The highest sample temperature achieved with the integrated heater was approximately 430 °C. This temperature was stable prior to applying any load to the sample. However, the temperature dropped to 420 °C within a few minutes of applying a small initial load (20 N) to remove any slack from between the holder/pins and sample. The temperature continued to drop as strain was applied, staying within (413 ± 2) °C from an applied stress of ~300 MPa through failure of the sample. This drop in measured temperature may have been caused by the thermocouple loosening as the sample was strained (but finding any evidence of this proved impossible as the thermocouple fell off the sample completely after it failed) and/or conduction heating through the frame rather than by a furnace heater, resulting in

a larger temperature gradient along the sample length. The substantial uncertainty in the temperature means it is quite possible that the true temperature of the sampled region in the higher temperature test is closer to 400 °C, putting it squarely below the reported threshold irradiation temperature. The 300 °C sample also cooled as it was deformed, despite initially stabilizing at 300 °C with the initial small load applied. It stayed within a range of (295 ± 2) °C from an applied stress of ~300 MPa through failure.

For each tensile test, the engineering stress, σ_e, was again calculated by eq. (3.2) and engineering strain ε_e by eq. (3.1). The true dimensions of the gage region of each sample were recorded prior to testing. The applied load F and relative displacement ΔL were measured directly by the Deben tensile stage.

4.2 X-ray Diffraction Analysis

The MATLAB script [58] described in section 3.2 was used and applied analogously to the diffraction patterns collected on the Mar345 detector. For comparison with fig. 3.6, fig. 4.5 shows the result of 3 steps in the code used to create the line profiles for analysis of the diffraction patterns collected by the Mar345 detector. The analyzed line profiles were created by integration over an azimuthal range of 20° about each of the axial and transverse directions.

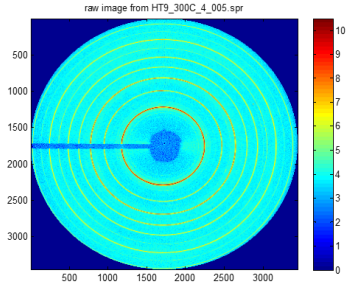

(a) The raw diffraction pattern collected on the Mar345 detector. The 6 strongest of the 9 ferrite rings seen here were used for peak profile fitting analysis.

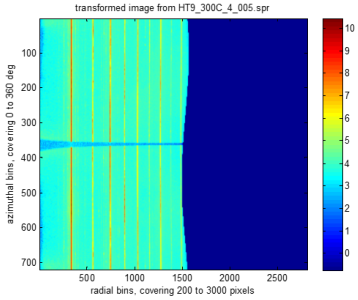

(b) The transform of the diffraction pattern collected on the Mar345 detector.

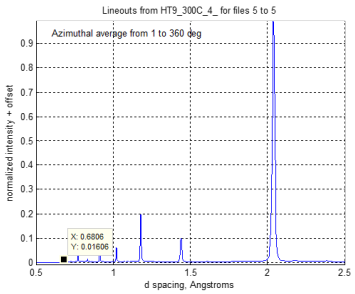

(c) The fully integrated diffraction line profile of the diffraction pattern, created by integrating across the complete azimuthal range to best identify all peaks from constituent phases.

Figure 4.5: Example outputs from the MATLAB script used to create line profiles. Diffraction data from HT9 at 300 °C prior to straining was collected by the Mar345 detector.

The change in each ferrite diffraction peak width was used as an indicator of dislocation

density evolution with deformation by using the modified Williamson-Hall analysis [55, 65]. The Williamson-Hall method is a technique used to deconvolute the effects of microstrain (from e.g. dislocations) from subgrain size effects. It is known that size broadening is diffraction order *independent* and strain broadening is diffraction order *dependent*. Based on the different dependencies, Williamson and Hall suggested that the full width at half maximum (FWHM) of diffraction profile peaks can be written as the sum of the two broadening effects as

$$\Delta K = 0.9/D + \Delta K^D \tag{4.1}$$

where the first term represents on the right hand side the size broadening resulting from average grain size D, and the second term ΔK^D is the microstrain contribution to broadening. Here $K = 2\sin\theta/\lambda$, $\Delta K = 2\cos\theta(\Delta\theta)/\lambda$, and θ, $\Delta\theta$, and λ are the diffraction angle, half of the FWHM of the diffraction peak, and the X-ray wavelength, respectively. Equation (4.1) assumes that ΔK^D is a linear or quadratic function of K. In a dislocated crystal, the equation takes the form

$$\Delta K^D = A(\rho*)^{1/2} + A'(Q*)^{1/2} \tag{4.2}$$

where ρ and Q are the dislocation density and correlation factor (in the simplest case, Q is the variance of the dislocation density), and $\rho*$ and $Q*$ are the values of these parameters when accounting for the average contrast factor,

$$\begin{aligned} \rho* &= \rho(\pi g^2 b^2 \bar{C})/2 \\ Q* &= Q(\pi g^2 b^2 \bar{C})^2/4 \end{aligned} \tag{4.3}$$

where $\bar{C}$ is the average contrast factor of dislocations for a particular reflection, g, and b is the Burgers vector of dislocations. In cubic materials, $\bar{C}$ is determined by

$$\bar{C} = \bar{C}_{h00}(1 - qH^2) \tag{4.4}$$

where $\bar{C}_{h00}$ is the average contrast factor of the h00 reflections, and H^2 is given by $(h^2k^2 + h^2l^2 + k^2l^2)/(h^2 + k^2 + l^2)^2$. $\bar{C}_{h00}$ varies depending on the edge/screw character of the dislocation and the material elastic constant, and q is a parameter characteristic of the material [66]. The value of the contrast factor defines the strain anisotropy in the material, and depends on the material elastic constant, relative orientation of the diffraction vector ($\mathbf{g}$), the Burgers vector ($\mathbf{b}$), the line vector, and the normal vector of the dislocation slip plane. Contrast factors are used as a measure of the visibility of

dislocations in diffraction experiments (for example, $\mathbf{bg} = 0$ would indicate no dislocation broadening effect in the peak profile).

By considering the effect of contrast factors, eq. (4.2) becomes eq. (4.5):

$$\Delta K = 0.9/D + (\pi A b^2/2)^{1/2} \rho^{1/2} (K\bar{C}^{1/2}) + (\pi A' b^2/2) Q^{1/2} (K^2 \bar{C}) \tag{4.5}$$

Equation (4.5), the modified Williamson-Hall equation, shows that the diffraction peak broadening as a result of microstrain caused by dislocations in a crystal will scale by $(K\bar{C}^{1/2})$ and not only by K. In this work, $\bar{C}_{h00}$ was tabulated for different screw and edge dislocation fractions, choosing the fraction which provided the best fit to the data (50% each) to create a modified Williamson-Hall plot in $\Delta K/\lambda$ vs $K\lambda$. The linear fit to the data then defines a slope and intercept indicative of the microstrain broadening (which is proportional to the square root of the average dislocation density) and size broadening (proportional to the inverse of the average subgrain size). To maximize the number of peaks contributing to this analysis, peak broadening was evaluated about the azimuthal angle η containing the most diffraction rings, (in this case, 45°). The modified Williamson-Hall plots generated from peak widths measured before and after deformation for both the 300 °C and 410 °C tests are shown in fig. 4.6. These plots were generated as a step in a MATLAB dislocation density estimation routine using the modified Williamson-Hall model. The routine fit lines to the points on each plot, and the parameter defining the slope of the line was used to generate the Williamson-Hall estimated dislocation density.

The linear fit of the data points converges with strain, indicating a more accurate choice of parameters for the strained state than for the undeformed material (possibly due to the estimated ratio of screw to edge dislocations).

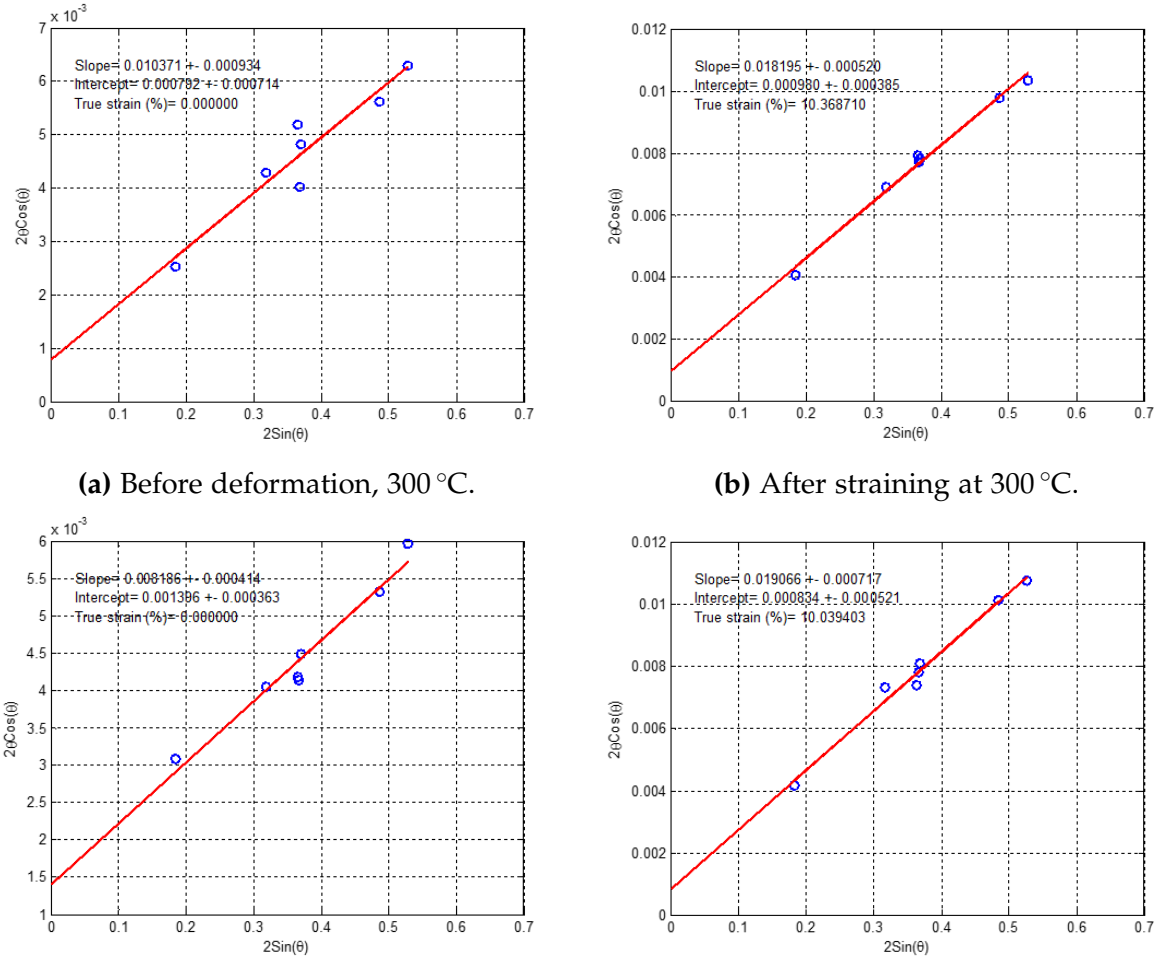

(a) Before deformation, 300 °C.

(b) After straining at 300 °C.

(c) Before deformation, 410 °C.

(d) After straining at 410 °C.

Figure 4.6: Modified Williamson-Hall plots produced by the MATLAB routine.

4.3 Results

The observed macroscopic stress-strain curves of the HT9 material tested at room temperature, 300 °C, and 410 °C are shown in fig. 4.7.

Because of the limitations of the screw-driven compact loading frame, some of these macroscopic measurements are suspect. No confidence should be placed in the room temperature macrostrain values, as these were determined during the problematic test conducted under load control. Because the loading stage used is screw driven (as opposed to hydraulic), it does not maneuver as precisely. When placed in load control, the stage tended to first overshoot the entered load by applying too large a displacement, then try to correct by moving the grips closer together again, and so forth. The controller for the tensile stage was also not well programmed, and would occasionally start reading

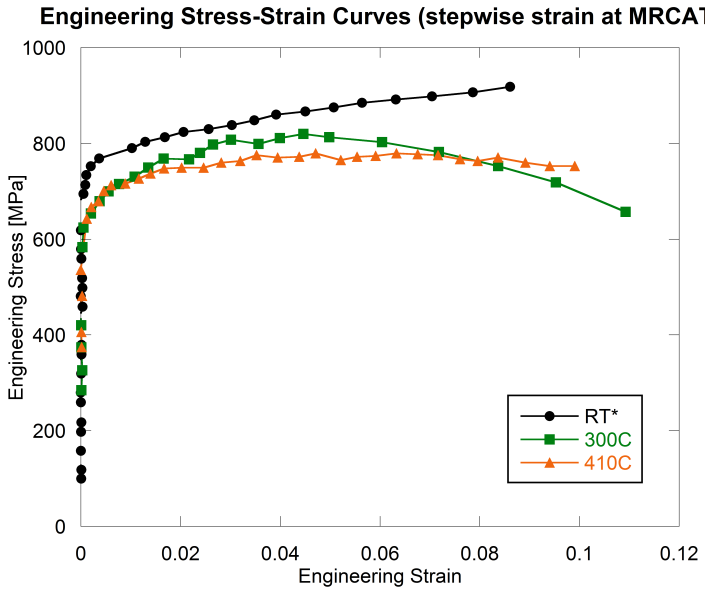

Figure 4.7: Macroscopic Stress-Strain curves for load tests conducted on unirradiated HT9 with stepwise strain. The room temperature curve can only be relied on for stress readings, not strain - pictured is a very rough approximation of the room temperature stress-strain curve.

out displacement (strain) values that were physically impossible given the range of the stage. We believe we traced this glitch to the control program being incompatible with displacement values that could become negative based on the grip spacing at which ”zero” was defined by the user. In any case, the macroscopic strain values should be disregarded for the test done under load control (at room temperature). Since the measured force from the loading stage did not have this problem, the room temperature stress-strain curve can still be used to look at tensile strength values. The recorded macroscopic strain values were adjusted down by a factor of 100 to artificially reproduce the rough shape of the expected room temperature deformation curve and fit it on the plot with those from the other test temperatures.

The high temperature tests were done under displacement control (strain control), during which the tensile stage and controller were much more agreeable. The stress-strain curves for both 300 °C and 410 °C tests are again shown to be very similar, falling beneath the room temperature curve. The lower temperature test displayed an only slightly higher UTS of 820 MPa compared to 780 MPa at 410 °C. The room temperature and 300 °C curve both exhibit similar strain hardening from the point of yield to the UTS. Less strain hardening occurred in the 410 °C test. The YS, UTS, and failure strength for each test temperature are shown in fig. 4.8 with values obtained by Roy in higher strain rate tests in a nitrogen atmosphere [32]. The stress values measured by the present

experiment are in excellent agreement.

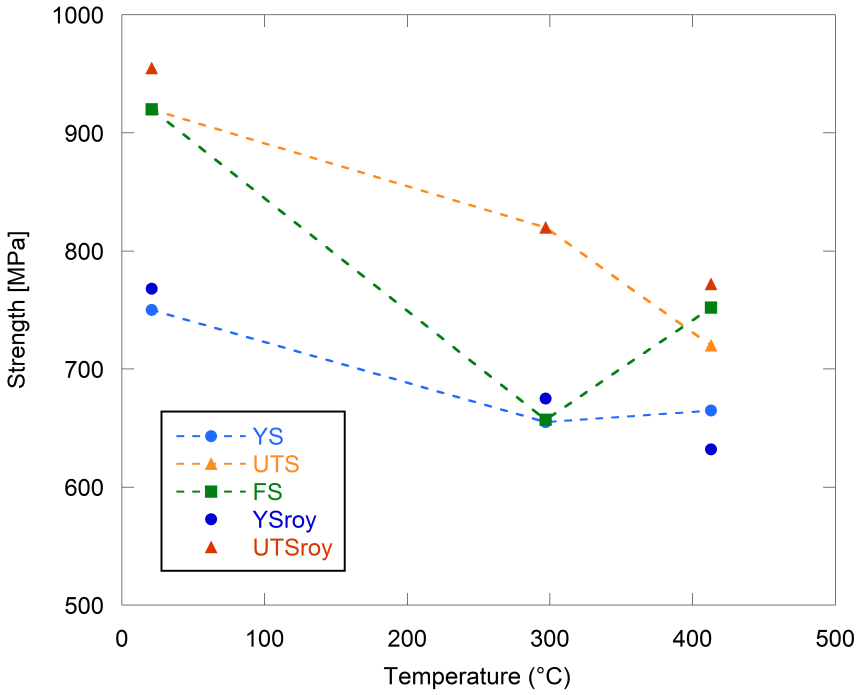

Figure 4.8: Strength properties of HT9 strained stepwise plotted as a function of test temperature. Here YS refers to the 0.2% offset yield strength, UTS to the ultimate tensile strength, and FS to the failure strength. The YS and UTS measured in elevated temperature tests by Roy [32] are included for comparison.

Because the room temperature test was performed using a lower energy X-ray beam, it showed comparatively superior resolution over a smaller range of d-spacings as compared to the high temperature tests. While not appropriate for making dislocation density estimates (since only 3 ferrite peaks were captured), this condition was ideal for examining minor phases in the material. A fully integrated diffraction line profile taken from the room temperature specimen prior to deformation is shown in fig. 4.9. Ferrite peaks are indexed in black. Only the (110), (200), and (211) peaks were captured. All other peaks were indexed as $Cr_{23}C_6$, using pdfcard #35-0783. No evidence of other precipitated phases was found in the diffraction pattern.

4.3.1 Lattice Strains

The hkl-specific lattice strains, ε_{hkl}, for the ferrite and carbide phases of the HT9 material as a function of applied stress are shown in fig. 4.10 for each of the 3 test temperatures. The response along the loading direction is shown with closed symbols, that along the

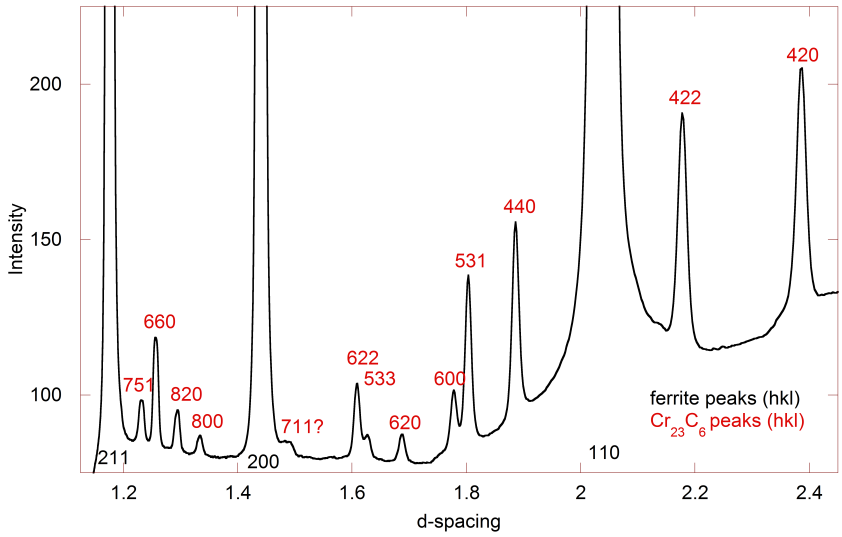

Figure 4.9: The pre-deformation diffraction line profile of HT9, integrated over the full azimuthal range for identification of constituent phases. The ferrite peak indices are printed in black and the $Cr_{23}C_6$ carbide in red. All peaks were attributable to either the ferrite matrix or the $Cr_{23}C_6$ carbide phase.

transverse direction with open ones. The carbide response is shown in red and the ferrite matrix in blue.

Elastic anisotropy in the ferrite hkl-specific lattice stresses is seen just as it was in the continuous strain test in section 3.3.1, with the (310) and (200) grains exhibiting lower effective elastic moduli than the remainder of the phase. The anisotropic behavior continues into the plastic region. While all of the ferrite lattice strains show similar development in the plastic region, the slopes in the (200) and (310) curves continue to be lower than the other ferrite curves. The carbide response is isotropic in the elastic region at all temperatures. It remains isotropic in the plastic region in almost all cases. The only appearance of anisotropy in the carbide response is seen in fig. 4.10b, which shows the (420) carbide grains unloading before the (422) in the transverse direction. The carbide strains were again quite noisy, the pictured plots were made by performing a 5-point smoothing operation on the (420) and (422) lattice strains.

The plastic deformation in the matrix phase exhibits the same strain development regions discussed in section 3.3.1. A detail view of this transition region for the room temperature sample is shown in fig. 4.11. The ferrite transition from elastic deformation to strain saturation to strain hardening is smoother in this case, the curve appearing this time more as an "S" shape. The transition points are most easily defined in the room

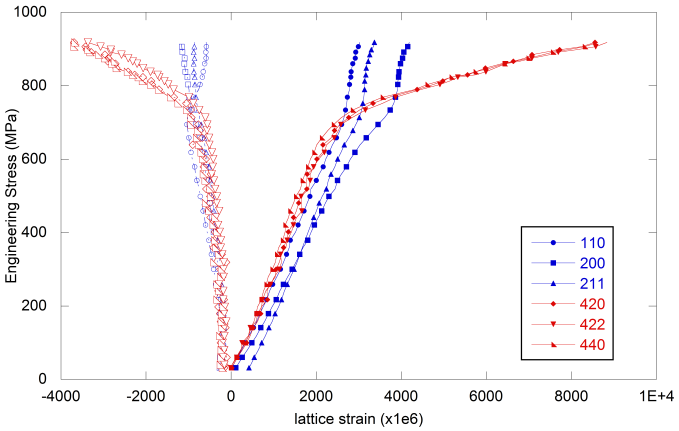

(a) Room Temp

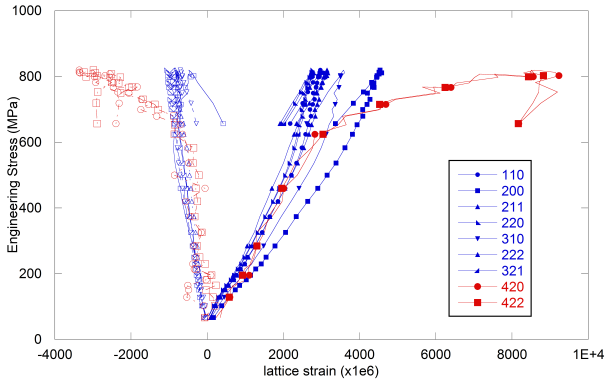

(b) 300 °C

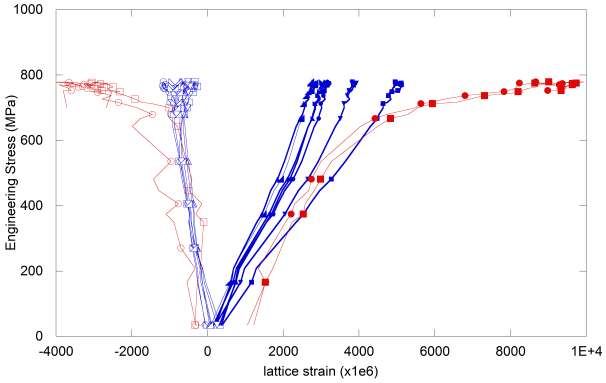

(c) 410 °C

Figure 4.10: Applied Stress vs. lattice strains for the ferrite matrix (blue) and carbide (red) in HT9 strained stepwise at different temperatures. The closed symbols represent the loading direction, the open symbols the transverse direction.

temperature case, and are more difficult to pinpoint in the higher temperature cases. The stress between the two transition points appears to increase with temperature, as it did in the continuous strain experiment.

4.3.2 Phase Stresses

Estimated principal axial phase stresses for each of the constituent phases of HT9 were calculated using eq. (3.4). The response of the (211) ferrite peak was assumed to be representative of the full matrix phase and the (420) $Cr_{23}C_6$ peak assumed to represent all of the $Cr_{23}C_6$ carbides. The axial phase stresses for each phase (in the direction of loading) are shown separately in fig. 4.12.

The accumulated axial stress in the ferrite phase is close to equivalent in both of the

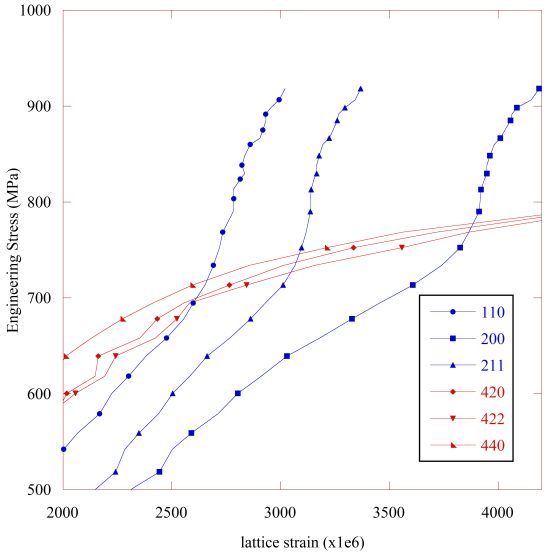

Figure 4.11: Detail view of the post-yield ferrite lattice strain development in HT9 stepwise strain tested at room temperature.

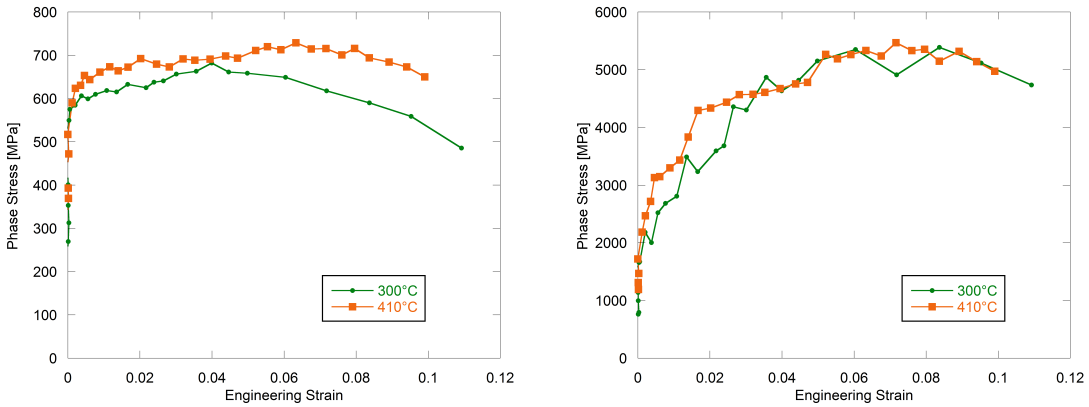

(a) ferrite (211) **(b)** carbide (420)

Figure 4.12: Estimated phase stresses (in the loading direction) in each of the constituent phases of HT9 at 300 °C and 410 °C: the matrix phase is represented by the (211) ferrite grains, and the $Cr_{23}C_6$ carbides by the (420) grains.

elevated temperature tests. The stresses at yield are 586 MPa and 622 MPa in the 300 °C and 410 °C tests, respectively. The maximum stress accumulated in each test is also roughly equal, 680 MPa at 300 °C and 730 MPa at 410 °C, but the strain at which the maximum stress is reached differs - at 4% in the lower and 6% in the higher temperature test. The estimated axial stress in the carbide phase at yield is approximately 2190 MPa

and 2460 MPa and 5375 MPa and 5480 MPa at maximum for the 300 °C and 410 °C tests, respectively. The accumulation of stress in the carbide with deformation is not dependent upon the test temperature in the range of 300 °C to 410 °C.

The phase stresses for the ferrite and carbide are shown together with the imposed (applied) stress for each test temperature in fig. 4.13. The macroscopic applied stress curve falls between the ferrite and carbide stresses in the axial direction. The axial stress in the ferrite is of the same order as the applied stress, the carbide stress is an order of magnitude larger. In the transverse direction as well, many times more stress accumulates in the carbide phase than in the ferrite.

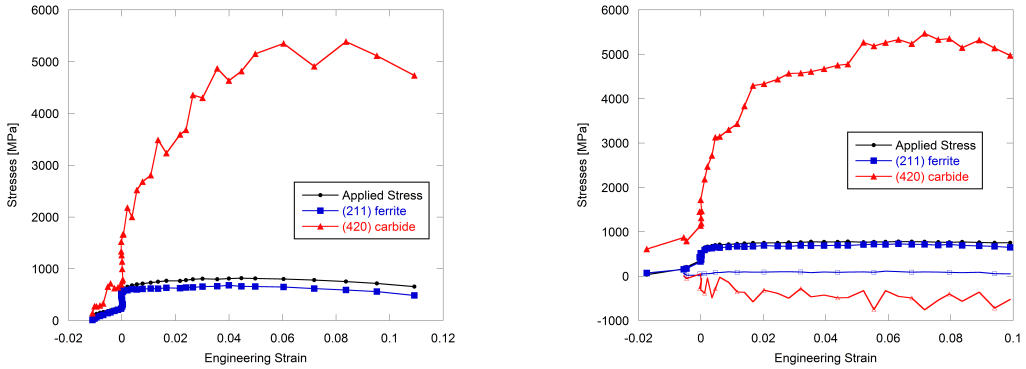

(a) 300 °C **(b)** 410 °C

Figure 4.13: A comparison of the stress development in each constituent phase of the HT9 material, where the matrix response is approximated by the (211) ferrite grains, shown in blue, and the carbide by the (420) $Cr_{23}C_6$ grains, shown in red. Closed symbols show the stresses in the axial direction, open symbols show the transverse direction.

4.3.3 Dislocation Density Evolution

The estimated dislocation density evolution for each of the high temperature tests was calculated using the modified Williamson-Hall method. The results depicting the evolution of dislocation density with applied stress and strain are shown in fig. 4.14.

As seen in fig. 4.14a, at 300 °C, the dislocation density stays constant until 540 MPa, then increases more rapidly with applied stress as the matrix deforms plastically. After the UTS is reached and necking has begun, the dislocation density increases slightly and thereafter remains constant. In the higher temperature test, the dislocation density appears to begin developing at a lower stress. It increases more rapidly with stress above

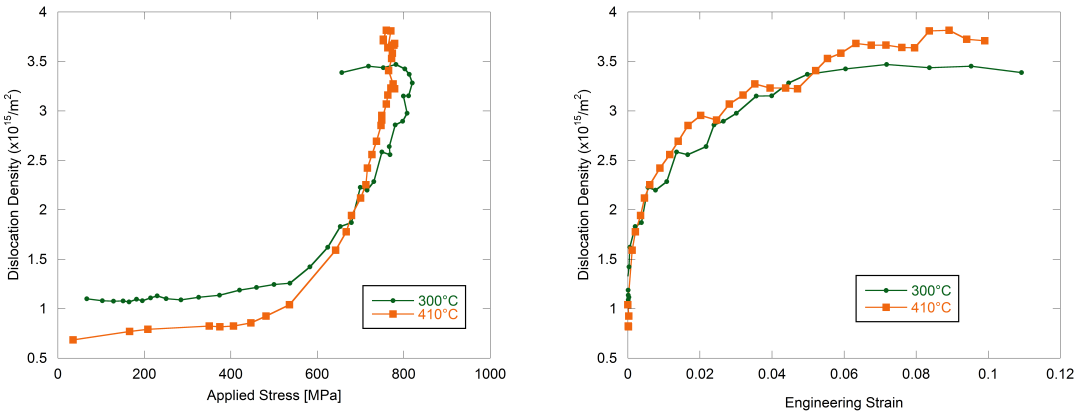

(a) Evolution with Stress.

(b) Evolution with Strain.

Figure 4.14: Dislocation density evolution during stepwise straining of HT9 at 300 °C and 410 °C, estimated using the modified Williamson-Hall model. Dislocation densities are shown as functions of Engineering Stress and Strain.

the YS until reaching the UTS. In fig. 4.14b, the dislocation density is shown developing rapidly with initial strain, then progressively more slowly until the uniform elongation strain is reached in the 300 °C test, shortly after which the dislocation density saturates. The sample tested at 410 °C did not show any non-uniform elongation, so the dislocation density does not appear to saturate.

Chapter 5

X–ray Diffraction Study of Load Partitioning in Irradiated HT9 Strained at Room Temperature

Prolonged exposure to neutron irradiation at high temperature changes the microstructure of materials through the creation of structural defects and introduction or enhancement of precipitated phases. To study the effect of irradiation conditions on the mechanical behavior of HT9, continuous strain tensile tests were conducted on samples extracted from the ACO–3 duct after its irradiation in FFTF. While previous studies examined post-irradiation microstructure and some mechanical properties, the way in which the microstructure and constituent phases influenced the macroscopic mechanical properties was merely inferred. Using high-energy X-ray diffraction, the internal phase strains and stresses experienced by the material were determined, helping to connect the internal structure of the irradiated material with its observable properties. The following presents the load partitioning behavior of irradiation-damaged HT9 as a function of its irradiation conditions. The specimens tested were irradiated for six years in the Fast Flux Test Facility (FFTF) experiencing fast spectrum neutron radiation doses ranging from 2 dpa to 147 dpa at temperatures from 382 °C to 504 °C, with the temperature-dose combinations depending on the location within the FFTF reactor core. Control and irradiated tensile samples were deformed in-situ while collecting high-energy X-ray diffraction data to monitor microstructural evolution. With the initiation of plastic deformation, all of the samples exhibited a clear load transfer from the ferrite matrix to carbide particulate. The dislocation density evolution in the material as a result of deformation was characterized through full pattern line profile analysis. There were substantial increases in the dislocation densities after deformation; the level of dislocation evolution observed was highly dependent upon the irradiation temperature of the sample. Differences in both the yield and hardening behavior between samples irradiated at higher and lower temperatures suggest the existence of a transition in tensile behavior at a temperature near 420 °C dividing regions of different dominant damage effects.

5.1 Experimental Methodology

5.1.1 Source and History of Material

The irradiated material used in this study was recovered from the ACO–3 hexagonal duct which experienced 6 years of irradiation exposure in the Fast Flux Test Facility (FFTF) during the Core Demonstration Experiment, a partial core loading of the FFTF to demonstrate fuel system capabilities. The hexagonal duct, shown in fig. 5.1, measured 367 cm in length, 60 mm across each hexagonal side, and 3 mm in wall thickness [28]. The nominal composition of the HT9 steel removed in the ACO–3 duct is Fe–11.8Cr–0.2C–0.2Si–0.5Mn–0.5W–0.3V–1.0Mo–0.5Ni in weight percent [39]. Prior to irradiation, the duct experienced a heat treatment of a 30 min hold at 1065 °C followed by an air cool, then a 60 min hold at 750 °C followed by a final air cool. The ACO–3 duct was irradiated at elevated temperature (367 °C–507 °C).

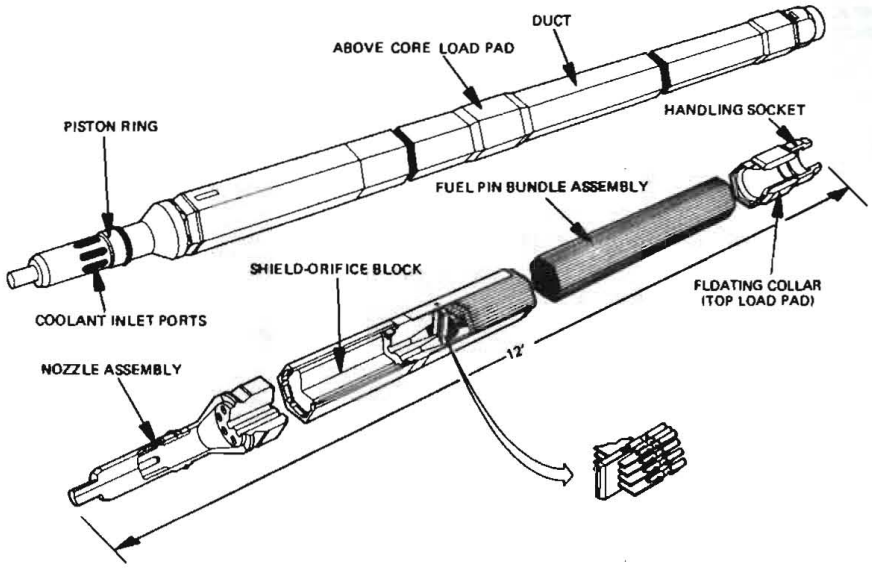

Figure 5.1: Schematic of the HT9 fuel pin irradiated in FFTF containing the hexagonal ACO-3 duct, from [67].

5.1.2 Sample Preparation

Samples were harvested from different positions along the duct after its irradiation. Depending on their position along the duct, these samples received doses from 2 dpa to 147 dpa at temperatures between 382 °C and 504 °C, see fig. 2.5. Note that, because

of the duct position in the FFTF core, the irradiation doses were lowest at the bottom and top of the duct, while the exposure temperature increased along the length of the duct from the bottom to the top [39]. Consequently, the combination of irradiation dose and irradiation temperature was unique for each position along the duct. Further details concerning the irradiation history of the duct and sample extraction technique are found in [28, 39]. Table 5.1 shows the irradiation conditions (both dose and average irradiation temperature) of the five test samples, historically labeled as 2E1, 5E1, 6E1, 6E5, and 6E9. Control specimens were removed from a sister duct which did not undergo irradiation. It should be noted that this control material is distinct (due to different thermo-mechanical processing) from the material used in the previous neutron diffraction tests of this alloy [59].

Table 5.1: Irradiation conditions of samples extracted from the ACO-3 duct.

Sample	Irradiation Temp (°C)	Dose (dpa)
2E1	504	2
5E1	441	147
6E1	416	110
6E5	399	42
6E9	382	22

Tensile samples in the "S1" geometry, shown in fig. 3.1, were electro-discharge machined (EDM'ed) from the control and irradiated duct material with a nominal gage length of 5 mm, width of 1.2 mm, and thickness of 500 µm.

5.1.3 Experimental Conditions

High-energy X-ray diffraction measurements were performed at the 1-ID beamline of the Advanced Photon Source (APS) at Argonne National Laboratory. The same load frame and pin holding method described in section 3.1.2 was used. Due to activation, the samples were covered with Kapton tape and contained in a polymer bellows attached to the grips during loading, shown in fig. 5.2. The force required to stretch the bellows was measured prior to the experiment and found to be negligible compared to the force required to deform the samples (2 orders of magnitude less). The engineering stress, σ_e, was calculated directly from the load cell by eq. (3.2). Unfortunately, due to the activity of the samples, we were unable to manually measure the gage area of each sample prior to loading at APS and instead relied on nominal dimensions and post-deformation

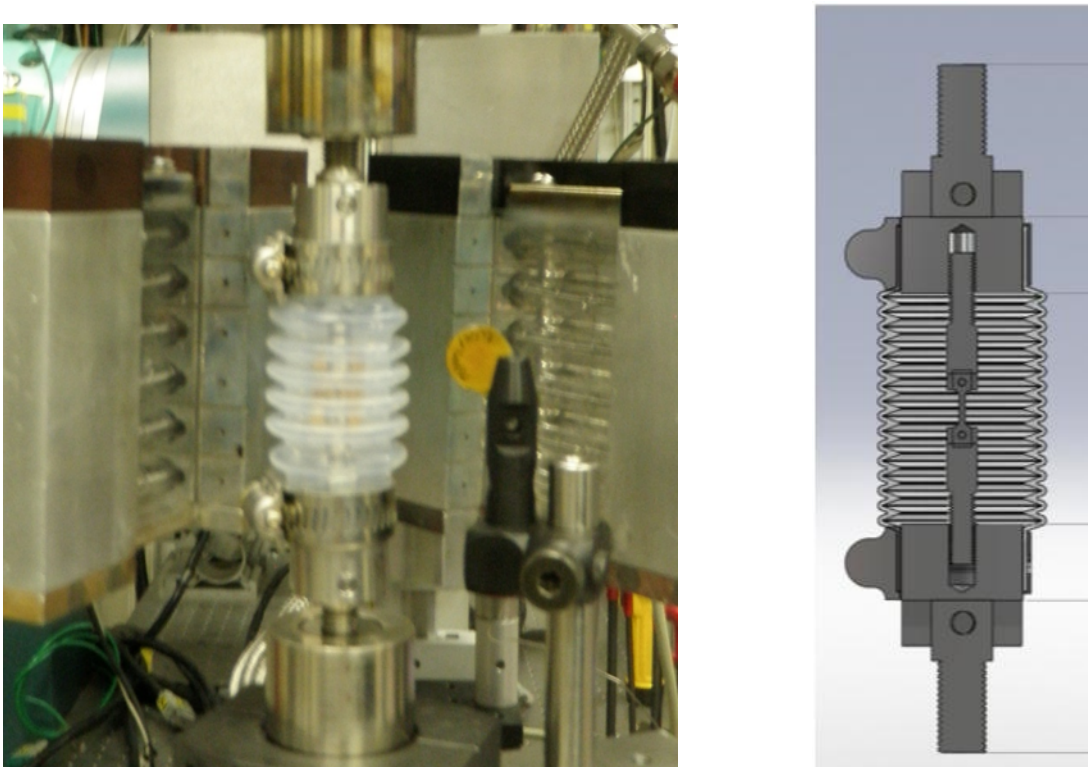

(a) **(b)**

Figure 5.2: An active sample wrapped in Kaptop tape is held in the load frame with pins and surrounded by a polymer bellows to provide secondary radioactive material containment in the event of sample failure.

measurements (conducted in hot cells at Los Alamos National Laboratory). Therefore the cross sectional area was not determined accurately. The estimated error in the thickness due to EDM slicing variations is approximately $\sim \pm 10\,\%$. Because the samples were cut relatively thin, a small absolute error in the final EDM'ed thickness resulted in a relatively large error in the cross sectional area. Also, the containment requirement prevented direct measurement of strain on the sample. The change in length of the sample was determined by a linear variable differential transducer (LVDT), but the pin holes in the sample distorted significantly during the measurement. Therefore, neither the macroscopic stress nor strain was determined as accurately as desired in the gage section of the sample.

The tensile samples were held and deformed vertically at room temperature with a constant crosshead speed corresponding to a strain rate of $1 \times 10^{-4}/\mathrm{s}$ under displacement control to displacements of $\sim$0.5 mm, resulting in plastic strains ranging from 3 % to 8 %, depending on the sample strength. Diffraction measurements were taken during deformation with a monochromatic 86 keV (λ = 0.144 Å) X-ray beam impinging on the

gage area of the sample. The incident beam size was $100 \times 100\ \mu m^2$. The Debye diffraction rings from the ferrite matrix and the carbide precipitates contained in the diffraction volume were recorded with a single GE41RT area detector composed of a 2048×2048 array of 200 µm pixels.

In order to examine internal lattice strains, diffraction measurements were conducted continuously during deformation with the detector set a distance of 1.15 m from the sample and centered on the through-beam, sampling a scattering angle 2θ of $\pm 9.7°$ in both vertical and horizontal directions. This configuration allowed for recording of complete Debye rings for peaks with d-spacing greater than 0.82 Å. The Debye rings were integrated in 15° segments centered at detector azimuthal angles, η, about the beam center to generate 24 diffraction line profiles (1-D patterns) using Fit2D [68, 69].

For whole profile diffraction line profile analysis (DLPA) to estimate dislocation densities, diffraction patterns were captured before and after deformation of each sample with the detector set at a distance of ~1.83 m and offset from the center of the through-beam by 184 mm. This off-center configuration sacrificed full Debye rings for all peaks, instead giving the maximum possible scattering angle (maximum $2\theta = 13°$) and optimizing instrument resolution for the best possible fitting of the whole profile. The instrumental broadening and peak shape were determined by fitting ceria peaks from a standard ceria reference sample. Recalibration of the detector was repeated after every change in the detector position.

5.2 X-ray Diffraction Analysis

5.2.1 Phase Strain and Stress

Rietveld refinement and single peak fits were completed for each diffraction pattern and lattice parameters for the ferrite matrix and carbides found with the General Structure Analysis Software (GSAS) [70]. A pseudo-Voigt function with fixed Lorentzian and fitted Gaussian components was used to fit the peak shapes and define their positions. Quoted uncertainties are based on the estimated standard deviations (esd's) returned by GSAS. The X-rays counted in a particular diffraction peak (hkl) are diffracted from a subset of grains defined by a specific plane normal (hkl) parallel to the diffraction vector. The evolution of that particular peak, e.g. change in position (d-space) or peak width, represents the evolution of that particular set of oriented grains. In this experiment, Rietveld fitting was incorporated to estimate the whole phase response of the ferrite

matrix. While the single peak fits represent the behavior of a particular set of grains, the lattice parameter determined from Rietveld refinement of the entire pattern, a, represents an empirical average over all grain orientations of the phase and represents the full phase response. As before, the internal lattice strains were calculated using eq. (3.3).

In the following, the phase strain in the matrix was calculated from the Rietveld refinement of the ferrite phase and the resulting lattice parameter a. In the control specimen, which was not activated and thus not in containment, several single carbide peaks were resolvable and Rietveld refinement of the carbide lattice parameter was completed as it was for the ferrite. In contrast, the parasitic, diffuse (incoherent) scattering caused by the polymer bellows necessary for the activated samples obscured several of the weak carbide peaks from the irradiated material making Rietveld refinement impossible. The strain in the carbides was thus calculated from the single peak fit of the $M_{23}C_6$ carbide (422) peak (where it was assumed that M=Cr) and the obtained interatomic spacing. This was the only carbide peak with adequate counting statistics for the irradiated samples and is assumed to be representative of the behavior of the carbide. As before, it is assumed that the lattice strains represent the response of the phase and thus the phase stresses were calculated in the axial direction using eq. (3.4).

Note, in general, it is not advisable to calculate a stress from hkl-specific strains because, with the exception of very specific textures, the grain sets sampled by strain measurements in orthogonal directions (axial and transverse) are distinct. Thus, a stress calculated using hkl-specific strains in multiple sample directions does not represent the stress perceived by any actual set of grains. In order to defensibly calculate a stress from hkl-specific strains, one implicitly assumes that the strains in the distinct grain sets sampled in the diffraction patterns with orthogonal diffraction patterns are equivalent, i.e. that the specific oriented grains are representative of the phase. Residual stress measurements using diffraction, in particular at monochromatic sources where it is difficult to record multiple diffraction peaks, often make this assumption out of necessity [71, 72], but the validity is seldom discussed.

In the following, strong orientation dependence of the hkl-specific strains in the steel ferrite phase will be presented. As such, the ferrite phase stress was not calculated from the hkl-specific strains but, rather, from the phase strain. However, less orientation dependence of the hkl-specific strains was observed in the carbide phase, in particular, of the control sample. Thus, as with many residual stress measurements, born of necessity, we assumed the strain determined from the (422) oriented grains was representative of the carbide phase and used it to calculate axial carbide phase stresses. The validity of this assumption will be addressed in the following.

5.2.2 Line Profile Analysis

The microstructures of the HT9 steel samples were quantitatively characterized using whole pattern DLPA. DLPA methods, as discussed in section 5.2.2, evaluate the measured data by forward modeling the diffraction pattern based on physical models of the microstructure and matching the theoretical pattern with the measured data [52, 55, 66, 73–75],. The models describe the effect of the following microstructural features: (i) the size distribution of the coherently scattering domains; (ii) the density, arrangement and character of dislocation structures; and (iii) frequency and type of planar faults [52, 74–77] on diffraction peak breadth and shape. The calculated profile functions corresponding to the various microstructural features, together with the experimentally determined instrumental peak broadening effects, are convolved to obtain the full theoretical diffraction pattern, which is fitted to the measured pattern in order to obtain the details of the microstructure [53].

The Extended Convolutional Multiple Whole Profile (eCMWP) line profile analysis software package was used to determine dislocation densities in the ferrite matrix both before and after deformation [53, 75]. The analysis was completed by modeling six independent diffraction peaks from the ferrite: (110, 200, 211, 220, 310, 321). The microstructure was refined for average sub-grain size and dislocation density. Background scattering from the containment and diffuse scattering from the radiation damaged samples obfuscated the eCMWP fits, in particular the fitting of the tails of the peaks. In this work, it was necessary to fix the variance of the lognormal crystallite size distribution and the Wilkens dislocation arrangement parameter, M. This arrangement parameter characterizes the configurational energy of the dislocation structure and is closely linked to the dipole character of the structure. Since the effect of this arrangement parameter mostly manifests in the shape of the tails of the diffraction peaks, the refined results for M were unreliable due to the additional background from the polymer containment. Thus, the values of M were fixed to those values obtained by eCMWP fits of high resolution neutron diffraction patterns of the same set of as-irradiated materials before loading [44]. The neutron diffraction patterns, taken with higher resolution and without the polymer bellows containment, had better quality peaks through the tail region yielding more reliable results for dislocation arrangement parameter. It was assumed for simplicity that the arrangement parameter was unchanged following the plastic deformation of the samples. This is not an ideal assumption, but the plastic strains were relatively small and, moreover, there is no basis to claim any particular evolution in M and therefore any prescribed variation in the parameter would be similarly unfounded.

In order to qualitatively examine the dislocation evolution during deformation, Rietveld refinement was performed on the ferrite peaks using GSAS and the microstrain extracted from the variance of the Gaussian component of the line shape. The Thompson-Cox-Hastings pseudo-Voigt function has a variance that depends on 2θ as follows:

$$\sigma^2 = U \tan^2\theta + V \tan\theta + W + P/\cos^2\theta \tag{5.1}$$

where the parameters U, V, and W are Cagliotti coefficients [78]. To get a qualitative measure of microstrain evolution during deformation, Rietveld fits of the ferrite peaks using this pseudo-Voigt function were completed by refining only one Gaussian fitting parameter, U. V was set to zero and W was fixed. Examining the variance equation above and considering that strain broadening goes as:

$$\Delta 2\theta = \Delta d/d \tan\theta \tag{5.2}$$

the strain broadening contribution to the variance is observable in the parameter U. Consider that the variance is

$$\sigma^2 = \langle \varepsilon^2 \rangle - \langle \varepsilon \rangle^2 \tag{5.3}$$

If we assume an appropriate selection of d_0, $\langle \varepsilon \rangle$ becomes zero and the variance is equal to the root mean square (rms) strain, $\varepsilon_{rms} = \langle \varepsilon^2 \rangle^{1/2}$. If we further assume that the development of microstrain in the matrix is coming primarily from an increase in dislocation density, then we can monitor the evolution of dislocation density in the matrix during deformation via the evolution of the ferrite rms strain values. This method is used here merely as a qualitative guide to dislocation evolution, recognizing it as complimentary to the more quantitative analysis of the dislocation density before and after deformation done with eCMWP. Thus, we used quantitative line profile analysis to determine the dislocation density before and after deformation, and qualitative analysis to monitor the evolution during deformation.

5.3 Results

Figure 5.3 shows the observed macroscopic stress-strain curves of the control and irradiated HT9 materials determined in-situ. With the caveat of increased uncertainty in the macroscopic stress and strain determined for the irradiated samples, the in-situ results are consistent with prior ex-situ mechanical tests [44, 61]. Material irradiated at

temperatures below 420 °C shows a significant increase in flow strength compared with the control material, while that irradiated above 420 °C shows little increased strength relative to the control material [44]. A decrease in the hardening rate is observed with increased yield strength. Unloading data are not shown for clarity.

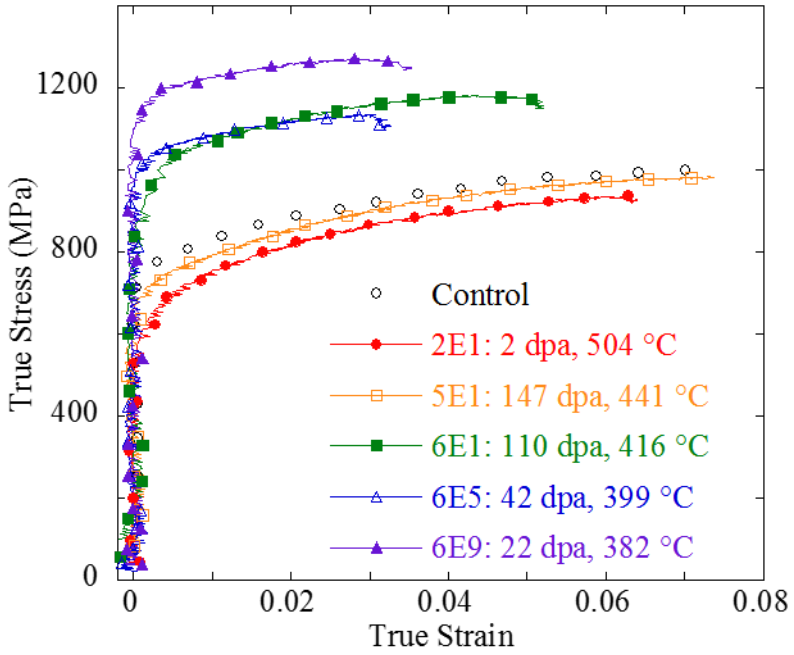

Figure 5.3: Macroscopic flow curves of control and irradiated materials determined in-situ during X-ray diffraction measurements.

5.3.1 Lattice Strains

Figure 5.4 shows several hkl-specific strains, ε_{hkl}, and the phase strain, ε_a, for the ferrite and carbide phases in the control material as a function of the applied stress. For clarity, only every 20th data point is indicated by a symbol, but the representative scatter in the experimental data can be gleaned from the noise in the lines, which go through every experimental point. The uncertainties in the strains in the ferrite are roughly 25$\mu\varepsilon$, and are smaller than the symbols. The uncertainties in the carbide strains are considerably larger, roughly 60$\mu\varepsilon$, comparable to the size of the symbols. These quoted uncertainties are based only on the quality of the GSAS refinement as represented by the esd's returned by GSAS. The true uncertainty in the strains may be much larger, but the uncertainties stemming from other considerations cannot be so easily quantified.

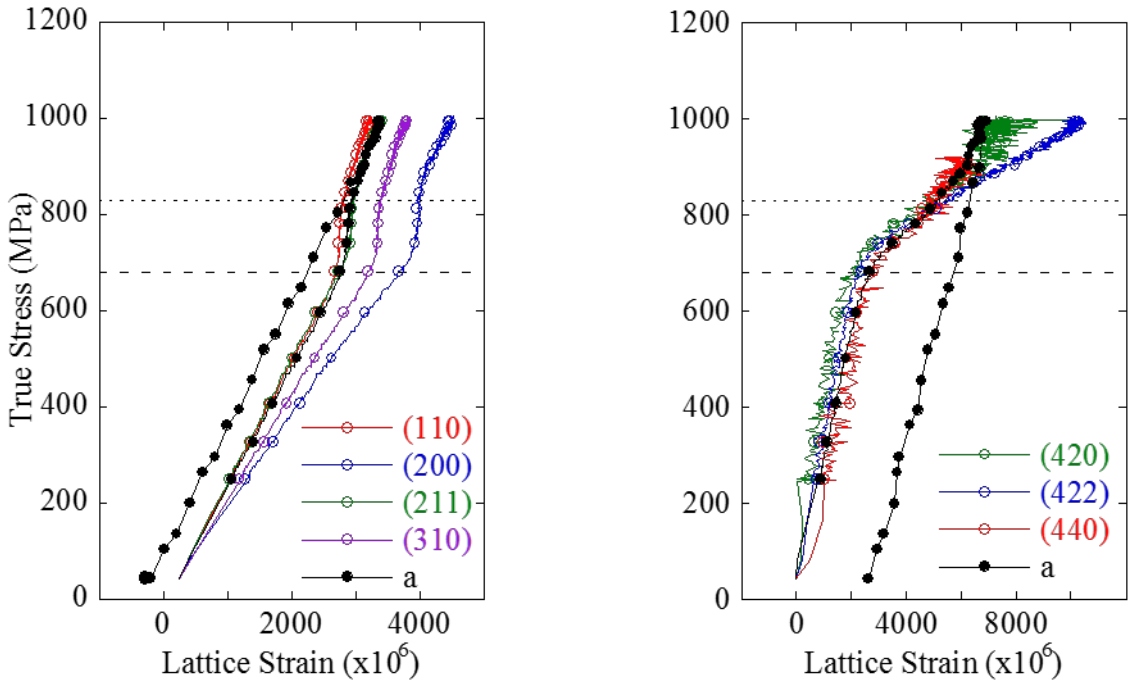

Figure 5.4: Control material: Measured stress vs. lattice strain curves for (a) the ferrite matrix and (b) the carbide precipitate.

The elastic anisotropy observed in the ferrite below the yield point (680 MPa) is expected based on the single crystal stiffness matrix [79] (the crystal is stiffest along the (111) plane normal, and most compliant along the (100)). The phase response closely matches that of (110) and (211) oriented grains. In contrast, the observed elastic response of the carbide particulate is relatively elastically isotropic.

Above 680 MPa, the experimentally observed ferrite lattice strains (hkl-specific and phase strains) saturate, indicating that the imposed strain is being accommodated by mechanisms other than elasticity, i.e. by plastic deformation in the matrix. Concomitantly, the carbide lattice strains increase at an elevated rate above the matrix yield point as subsequent increases in the applied load are shed from the ferrite matrix to the carbide particulate. Beyond 830 MPa, the ferrite grains again accumulate elastic strain, indicating that they have hardened. At this point, the first hint of strain anisotropy is observed in the carbide. The (422) oriented carbide grains continue to accumulate strain at an enhanced rate while the lattice strains in the (420) and (440) oriented grains, as well as the phase strain, accumulated at a decreased rate above 830 MPa. The relative isotropy of the grain response of the carbide phase throughout most of the deformation lends credence to the use of a single peak strain in the calculation of the phase stress, described above.

Figure 5.5a shows a plot of applied stress versus the experimentally observed phase strains in the loading direction (solid symbols) and transverse direction (open symbols) for the ferrite matrix and carbide phases of the control material. As plotted in fig. 5.5a, the difference in the loading direction phase strains between the matrix and carbide is immediately evident. The ratio of the elastic moduli of the two phases individually is $E_{carbide}/E_{ferrite} = 1.47$. However, the mutual geometric constraint of the phases in the composite forces the effective moduli ratio much closer to unity, experimentally observed to be 1.23 ± 0.02. The plastic response in fig. 5.5a is as described in reference to fig. 5.4, but less distinct because the scale is enlarged to include the transverse response.

Figure 5.5b shows similar data collected on the 504 °C/2 dpa material. The uncertainty in the carbide lattice strain increases in the irradiated material to roughly $150\mu\varepsilon$. Overall, the response of the individual phases is similar to the control material, with the yield strength reduced from 630 MPa to roughly 590 MPa. The ratio of the effective elastic moduli in the 504 °C/2 dpa material is 1.18 ± 0.04, again similar to the control material. Also similar to the control material, the phase strain in the ferrite saturates above the yield point and later begins to increase again, in this case, above ~750 MPa.

Figures 5.5c to 5.5f show similar data collected on material with the remaining irradiation conditions (441 °C/147 dpa, 416 °C/110 dpa, 399 °C/42 dpa, and 382 °C/22 dpa, respectively). The relative elastic response of the constituent phases is fundamentally different in these materials from that observed in the control and 504 °C/2 dpa material. In the material which received higher doses of radiation at lower temperatures, the carbide and ferrite phase strain curves are collinear in the elastic regime. This is unexpected, as this behavior typically presents in the case of e.g. a fiber composite, with fibers parallel to the straining direction, wherein both phases are geometrically constrained to accumulate the same strain [80]. Since we know the carbides are not constrained by fiber geometry in this material, it is unclear what is causing the coupling of the phase strains.

While cross sample comparison of the phase moduli is ill-advised because of the uncertainty in the macroscopic stress measurement, the ratio of the carbide to ferrite stiffness is insensitive to uncertainty in the macroscopic stress and can be compared across samples. In the 441 °C/147 dpa, 416 °C/110 dpa, 399 °C/42 dpa, and 382 °C/22 dpa materials, the observed ratio $E_{carbide}/E_{ferrite}$ is 0.98, 1.06, 1.12, and 1.09, respectively.

The behavior of the ferrite in the 441 °C/147 dpa material following the activation of plasticity, i.e. saturation of the lattice strains at 710 MPa followed by subsequent accumulation of strain above 900 MPa, is similar to the control and 504 °C/2 dpa material with the expected increase in the yield strength based on the macroscopic flow curve. However, the evolution of the phase strain in the ferrite beyond the initiation of plasticity

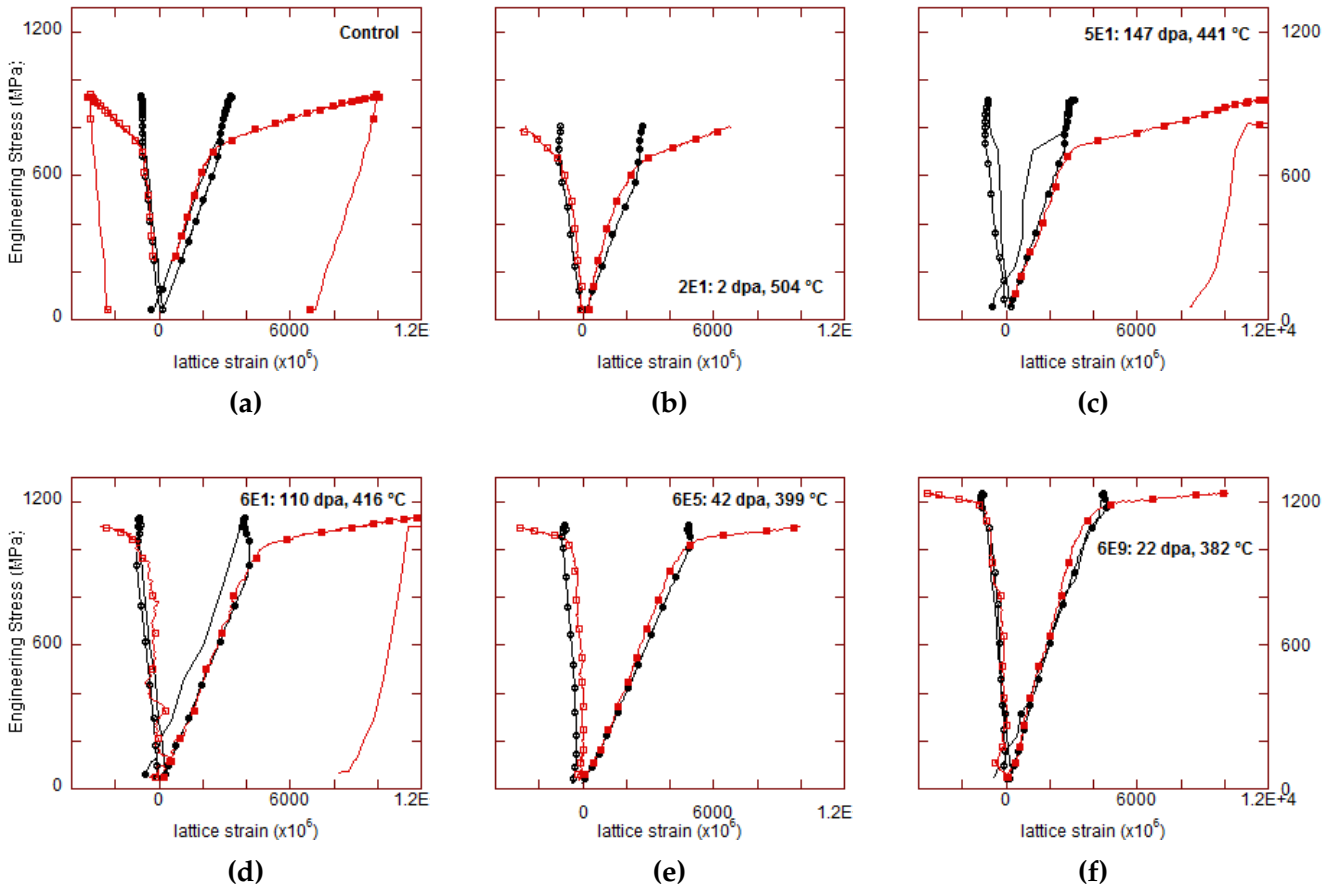

Figure 5.5: Stress vs. phase strains for the ferrite matrix (black) and carbide (red) in the control and irradiated materials.

is distinct in the 416 °C/110 dpa, 399 °C/42 dpa, and 382 °C/22 dpa materials. In each of these materials, the ferrite strain saturates at yield of the matrix, but does not later increase as observed in the control, 504 °C/2 dpa and 441 °C/147 dpa materials.

It is difficult to discern interesting behavior in the transverse strains, which are relatively small. The one exception is the 399 °C/42 dpa material where the transverse strain is nearly 0 throughout the deformation test. This is unphysical and an artifact of the data analysis (during which the profile fits in the transverse direction failed). We note that the carbide strain in the irradiated material, in particular in the transverse direction, was often not well determined by GSAS. In the case of the 441 °C/147 dpa material, the carbide phase in the diffraction pattern transverse to the straining direction could not be fit accurately at all. In the case of the 416 °C/110 dpa, 399 °C/42 dpa, and 382 °C/22 dpa materials, the fits to the carbide in the transverse direction became unstable prior to the completion of the deformation test.

5.3.2 Phase Stresses

Figure 5.6a shows the evolution of axial phase stresses in the ferrite during deformation of the control and irradiated materials. The phase stresses were calculated using eq. (3.4). The lack of reliable transverse strains from the carbides in the irradiated samples throughout the entire duration of the deformation tests makes it impossible to calculate the carbide phase stresses in these samples. Thus, for comparison with fig. 5.6a, fig. 5.6b shows the longitudinal phase strain in the carbides in the deforming control and irradiated materials, which is well determined and, in a tensor multiplication sense, is proportional to the axial phase stress. Reliable transverse strain data were available for the control material, enabling determination of the carbide axial phase stress in this case. Thus, the right axis of fig. 5.6b shows approximate stress levels associated with the lattice strains of the carbides in the control material. These provide the reader with a rough idea of the stress carried by the carbides in all of the samples.

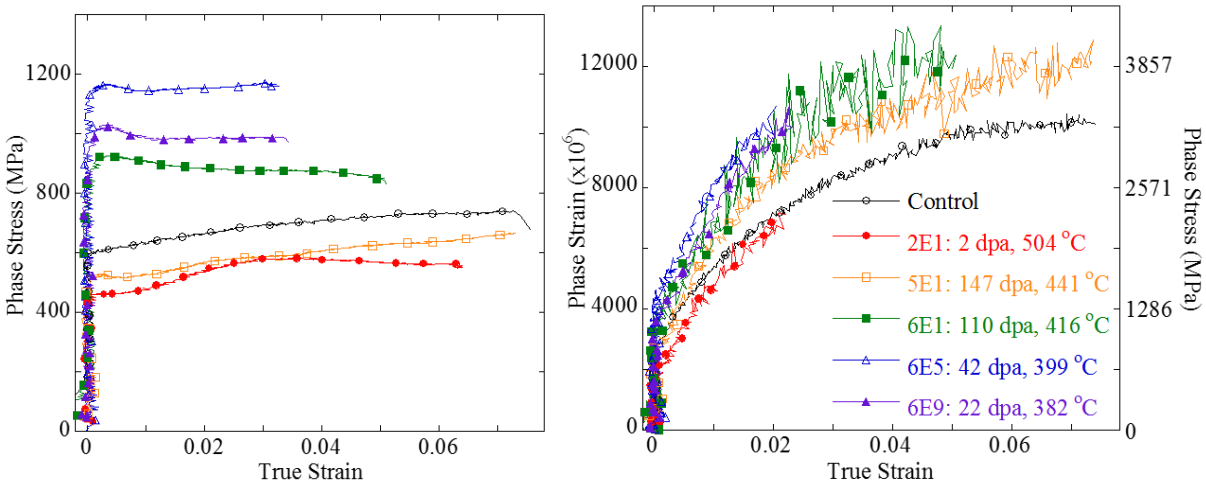

Figure 5.6: Evolution of the (a) ferrite phase stresses and (b) carbide phase strains with tensile deformation. The right axis on (b) represents the approximate carbide phase stress in the control material to provide a rough stress scale for the carbide phases in the irradiated materials as described in the text.

The evolution of the stress in the matrix varies greatly depending on whether the material was irradiated above or below 420 °C. Specifically, in the control material, the ferrite matrix yields when the axial phase stress is roughly 590 MPa, corresponding to a macroscopic applied stress of 700 MPa (fig. 5.3). The ferrite hardens to 740 MPa at the end of the test, at 0.07 strain. Beyond the yield point, subsequent increases in the macroscopic stress are being predominantly carried by the small volume fraction of

carbide reinforcement phase as the axial stress on that phase increases from roughly 800 MPa at the yield point to over 3000 MPa at the completion of the test.

The phase specific responses of the 504 °C/2 dpa and 441 °C/147 dpa materials (irradiated above 420 °C) are similar to the control material, with the yield stress on the ferrite slightly lower. It is interesting to note that the macroscopic flow stress of the control material and 441 °C/147 dpa material are very similar. Yet, the ferrite yields at a lower phase stress in the 441 °C/147 dpa material, while the carbide carries a larger portion of the load. This suggests a change in the mechanism of stress transfer between the materials.

In contrast, the yield strength of the ferrite in the material irradiated below 420 °C has increased to approach 1 GPa, and softens with subsequent plastic strain. The load carried by the carbide is correspondingly higher in these materials. We note that in an absolute sense, the ferrite phase stress observed in the 399 °C/42 dpa material is inconsistent with the observed macroscopic flow strength, i.e. the axial phase stress is larger than the macroscopic stress. This is due to the observed transverse strain shown in fig. 5.5e which was noted to be unphysical.

5.3.3 Peak Broadening

Figure 5.7 shows the (110) ferrite diffraction peak before and after deformation for two irradiation conditions (504 °C/2 dpa and 399 °C/42 dpa), with the intensity and peak position normalized to highlight the broadening; the broadening post-deformation is readily apparent. The full width at half maximum (FWHM) of the peaks evolve from 0.0050 $Å^{-1}$ to 0.0063 $Å^{-1}$ and from 0.0056 $Å^{-1}$ to 0.0069 $Å^{-1}$ in the 504 °C/2 dpa and 399 °C/42 dpa material, respectively. The lower temperature irradiated material starts with broader peaks, consistent with [44], and they remain as such following the deformation.

To give a qualitative view of the evolution of the dislocation density during deformation, fig. 5.8a shows the development of the root mean square (rms) strain, $\varepsilon_{rms} = \sqrt{\langle \varepsilon^2 \rangle}$, in each ferrite phase with increasing plastic strain. The control material as well as material irradiated at temperatures above 420 °C exhibit initially low ε_{rms}, while the materials irradiated at temperatures below 420 °C have higher ε_{rms}. ε_{rms} increases with plastic strain in all of the material, approaching 0.8 % where it seems to saturate. It is important to recognize what this number represents: the width of the distribution of the lattice strain around the average strain. A variance of 0.8 % represents a large distribution of

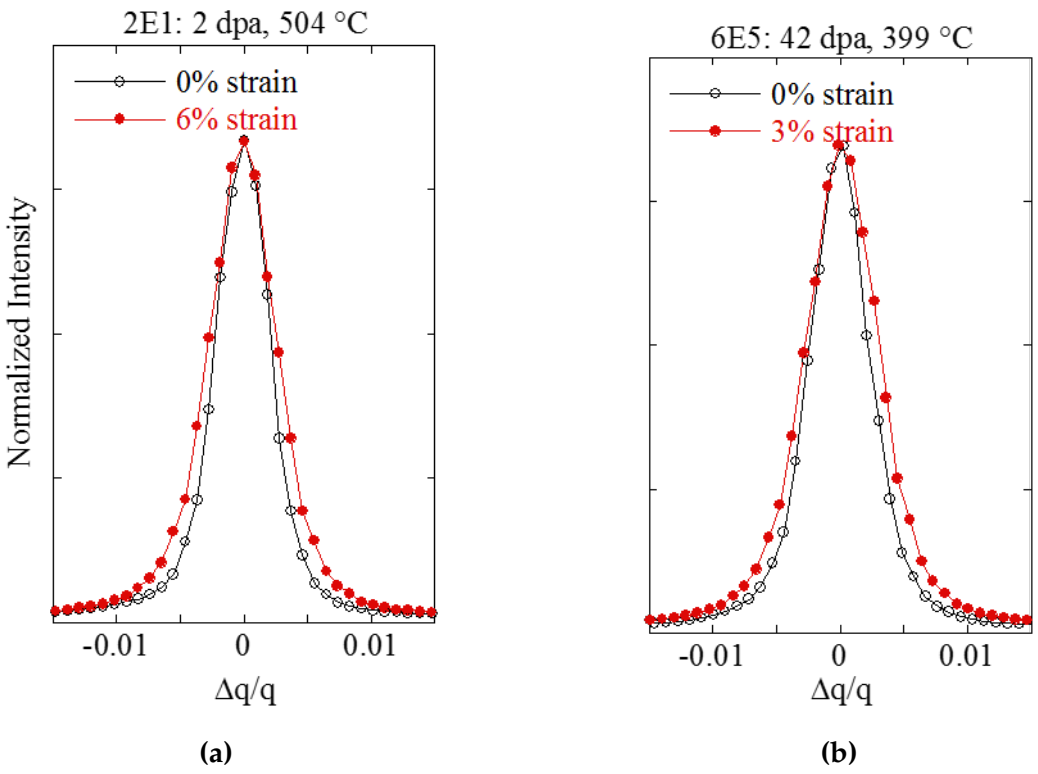

Figure 5.7: The (110) peak before and after irradiation.

elastic strain and is not consistent with variation in stress distribution across grain sets as the distribution itself would have to be much larger than the yield stress. This indicates that the major source of microstrain in the matrix phase are the heterogeneous strain fields associated with individual dislocations, consistent with our assumption, so we may view the evolution of the ferrite rms strain as representative of the qualitative dislocation density evolution. If changes in the Wilkens dislocation arrangement parameter (M) are neglected, ε_{rms} scales roughly with the square root of the dislocation density. Figure 5.8b shows the ε_{rms} observed in the carbide. The scale is held fixed relative to fig. 5.8a to emphasis the difference between the ferrite and carbide. Nearly an order of magnitude less microstrain develops in the carbide phase of each material with plastic strain, saturating at roughly 0.1 %. At this level of microstrain, it is reasonable to associate it with heterogeneous stress distribution based on variations in the local neighborhood of the individual carbide grains.

The increase in peak breadth of the ferrite peaks following deformation is unequivocal. As is often the case, the interpretation of same is more problematic. Line profile analysis of high resolution neutron and X-ray diffraction data completed specifically to determine the dislocation density and coherent crystal size was reported by Mosbrucker in [44]. The

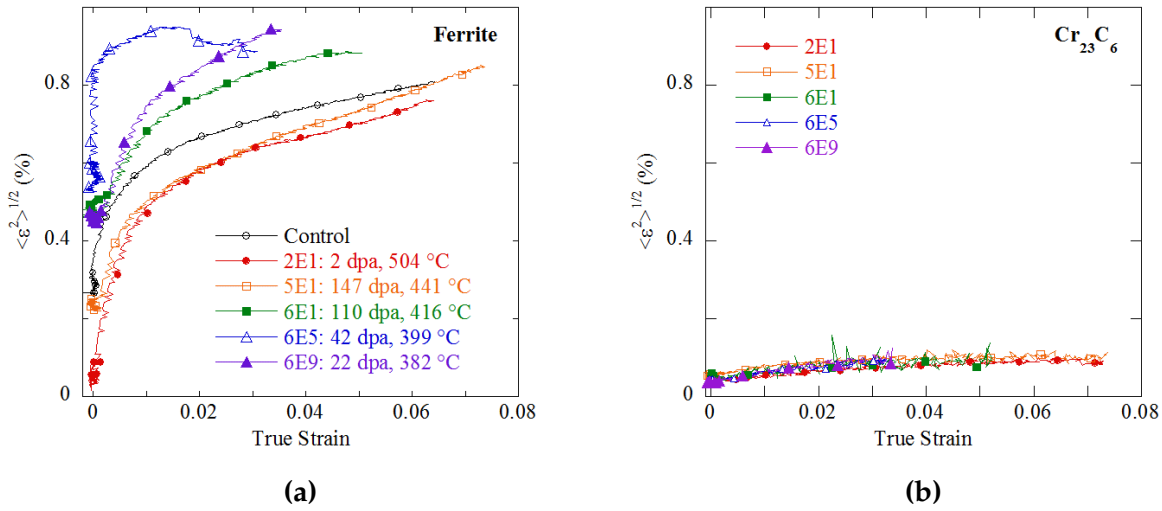

Figure 5.8: Development of root mean square strain in each phase.

current samples were analyzed analogously in the as-received state, but the data were less robust due to parasitic scattering from the polymer bellows containment. Figure 5.9 shows the dislocation density as a function of irradiation temperature (pre-deformation), determined using eCMWP for line profile analysis, in the current work and [44]. The agreement is very good, lending credibility to the results of the current work, even with data obscured by scatter from the containment. Figure 5.9 also shows the dislocation density in each material at the completion of the deformation test. In each case the dislocation density has increased considerably following deformation.

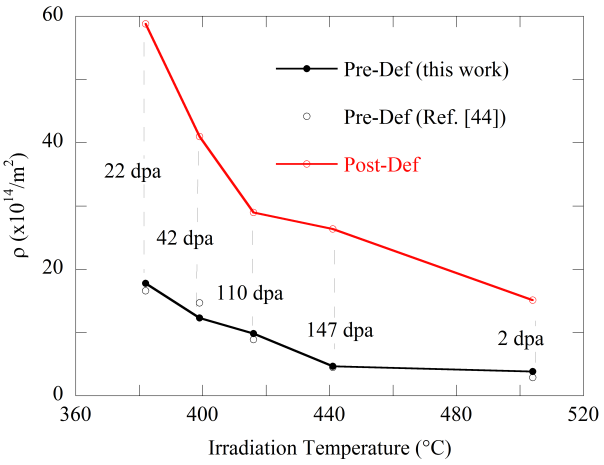

Figure 5.9: Observed dislocation densities obtained with eCMWP fitting before and after deformation.

Chapter 6

Discussion

The peak shape and positions derived from fitting the peaks in the observed diffraction line profiles were directly related to the evolution of material microstructure, its phase stresses, and dislocation density. Examination of the variation in these parameters before, during, and after deformation of the material lends understanding to the relationship between these microstructural properties and the macroscopic mechanical behavior of the material. This discussion will focus on the effect of both irradiation conditions and tensile test temperature on the deformation behavior of HT9, and the various differences in material condition and mechanisms that give rise to these dependencies.

6.1 The Effect of Sample Irradiation Conditions

What follows is a discussion of the results of the in-situ tensile tests conducted on the material extracted from the ACO–3 duct. Our results will be compared with previous microstructural examinations made on material extracted from the duct.

6.1.1 Elastic Deformation

The elastic response of the control and 504 °C/2 dpa materials is similar; the modulus of each phase is distinct and linear, as is usual and predicted. This similarity in response is to be expected, as the samples irradiated to 2 dpa at 504 °C and the control sample have similar microstructures and have been shown not to contain the same irradiation-induced phase structures, namely α' and G phase, present in samples irradiated at lower temperatures [15].

In contrast, the remaining irradiated materials exhibit the same phase-specific elastic modulus for the ferrite and carbide; this is unexpected in a particulate composite. It is unlikely that the irradiation-induced dislocation density alters the elastic interaction between the matrix and carbide. Confidence in that assertion is bolstered by the fact that

T °C	dpa	Cr solub at % (G. Bonny)	Cr solub at % (Phase diagram)	α′		G-phase		Loops		voids	
				L nm	d x10^{21} m^{-3}	L nm	d x10^{21} m^{-3}	L nm	d X10^{21} m^{-3}	L nm	d X10^{21} m^{-3}
380	20	9	8.1	7.8	72	11.3	9.3	14	0.93	X	X
410	100	9.1	10.1	9	2.6	16.2	1.4	-	-	23	-
440	155	9.3	12.4	9.6	9.5	26.5	1.1	18	0.5	28	0.25
466	92	9.9	14.7	X	X	X	X			X	X
505	2	12.5	18.5	X	X	X	X			X	X
475	10,000 hrs	10.3	15.5	X	X	X	X			X	X

Table 6.1: A summary of the microstructural characterizations of HT9 samples extracted from the ACO–3 duct irradiated at a variety of dose and temperature combinations, taken from [81].

the 441 °C/147 dpa material, which exhibits the elastic collinear deformation described in section 5.3.1, has the same dislocation density as the 504 °C/2 dpa material, which has distinct moduli for the ferrite and carbide phases. The material irradiated to higher dose at a lower temperature has been shown to contain irradiation-induced minor phases, including the α′ and G phases, as well as voids [15, 44]. The precipitation of these phases could affect the local (if not global) chemistry of the matrix and/or locally strengthen the matrix. We speculate that the effects of these microstructural features alter the elastic interaction between the matrix and carbide phases. For reference, a summary of the as-irradiated microstructure for various samples of HT9 extracted from the ACO–3 duct is shown in table 6.1.

6.1.2 Plastic Deformation

In Mosbrucker's work [44], it was shown that the initial yield strength of the irradiated material was roughly proportional to the square root of the post-irradiation dislocation density, consistent with the Taylor law [82],

$$\sigma = \sigma_0 + M_T \alpha G b \sqrt{\rho} \tag{6.1}$$

where σ is stress, the Taylor factor, M_T, is 3 [82, 83], G is the shear stress (86.95 GPa for HT9 steel), b is the length of the Burgers vector, 2.466 Å for the $\langle 111 \rangle \{110\}$ slip system, and ρ is the dislocation density. Here, α is a factor describing the strength of the obstacles that a moving dislocation has to overcome during plastic deformation; for metals, the value of α is usually roughly 0.3 [84].

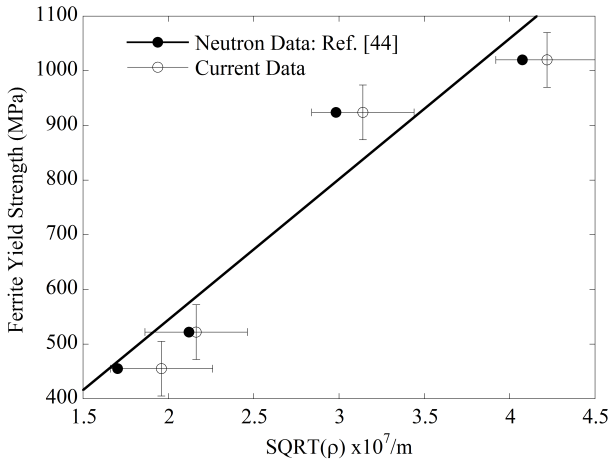

Figure 6.1: Dependence of the ferrite yield strength on the square root of the observed dislocation density.

It is perhaps more appropriate to remake the Taylor plot using the yield stress of the ferrite determined herein, rather than the macroscopic yield strength. This is shown in fig. 6.1. Note, we have omitted the 399 °C/42 dpa data as the yield strength is skewed by the unphysical transverse strains (shown in fig. 5.5e). The plot of the square root of the dislocation density with the phase yield strength of each sample is roughly linear, indicating that the ferrite yield stress of the irradiated samples is largely determined by their post-irradiation dislocation density and the interactions between those dislocations, consistent with the Taylor model.

The evolution of the dislocation density during deformation is not consistent with the Taylor Law. In particular, the dislocation density of the samples irradiated below 420 °C (416 °C/110 dpa, 399 °C/42 dpa, and 382 °C/22 dpa) increases with deformation, while the flow strength of the ferrite reaches a maximum at very low strains and thereafter remains constant or decreases. Transmission electron microscopy examination of the as-irradiated and deformed microstructures was performed on the 382 °C/22 dpa sample, shown in fig. 6.2. This condition was selected for further examination since it shows the largest increase in yield strength of any of the irradiated conditions and the as-irradiated microstructure has been examined previously [15, 40].

The as-deformed microstructure shows high dislocation densities and precipitate densities. This is consistent with the earlier TEM results on this material irradiation condition in the undeformed state [15, 40]. Relatively large void structures in the deformed material are seen on the lath boundaries in fig. 6.2a. The high precipitate and dislocation densities and their interactions are evident in fig. 6.2b. Earlier studies,

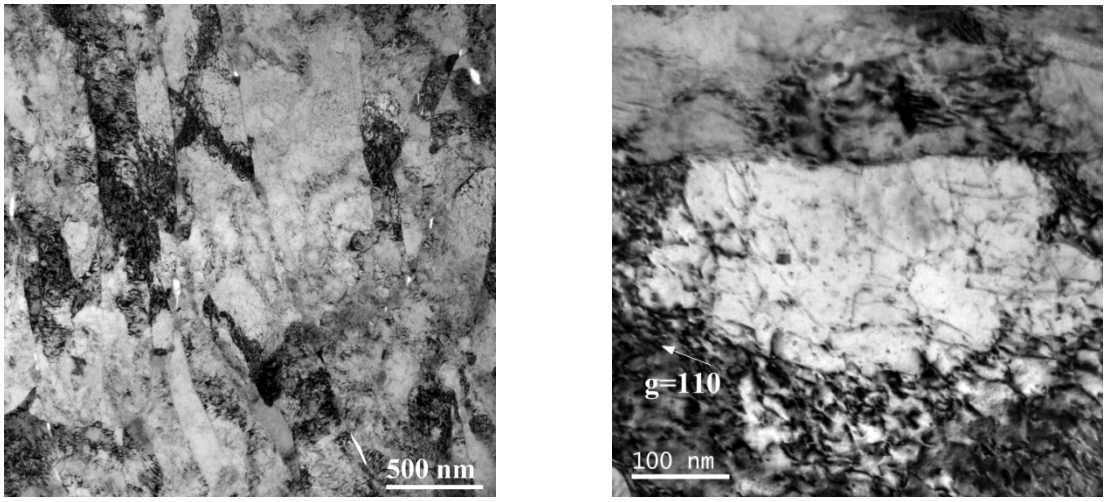

(a) **(b)**

Figure 6.2: Bright field TEM images of HT9 irradiated to 20 dpa at 380 °C, after deformation to ~3.5 % strain: In (a), most of the voids are seen along lath boundaries, (b) shows a high density of dislocations and precipitates with the potential for interaction and pinning. Microscopy was performed by O. Anderoglu, for further detail see [85].

[15, 40], show the presence of a high number density of α' precipitates at 380 °C with sizes ranging from 4 nm to 11 nm in the as-irradiated material. The number density reduces with increasing irradiation temperature, with no α' precipitates found in the sample irradiated at 505 °C. Despite the high number densities at moderate temperatures, Cr content in this material is on the edge of the compositions where α' is found. The highest experimentally derived α' content in any of these irradiation conditions is less than 4 % by volume and may not have a major impact on the observed mechanical properties. Nevertheless, the highest observed concentrations of α' are found in the material condition with the highest yield strength: 380 °C at 20 dpa [15, 40].

In the current study, there is no evidence of dislocation channeling or flow localization processes which have been observed in other post-irradiation deformation studies of similar materials [86, 87]. The tensile results here, shown in fig. 5.3, indicate sustained plastic hardening following yield in all of the tests. This behavior indicates some level of uniform plastic flow as opposed to sharp load drops following yield and more localized flow typical of flow localization behavior. In the two lower temperature samples, 382 °C and 399 °C, there is minimal identifiable work hardening with a large increase in dislocation density. This behavior has been seen before in steels [88], and is an indication of uniform plastic flow over the range of plastic deformation investigated in these studies. This supports a process where mobile dislocation structures in the material can annihilate the irradiation-induced dislocation loops initially present in the as-irradiated material as

they move during plastic deformation, reducing the work hardening of the material. The TEM results, in fig. 6.2, show a widely dispersed dislocation structure within the laths as well as the higher density dislocation structures in the lath boundaries. The radiation-induced precipitation structure, particularly at lower irradiation temperature [15, 40], accounts for the elevated yield strength. The relatively uniform distribution of dislocation structures within lath boundaries accounts for the observed strain hardening behavior. This more uniform plastic deformation behavior and the ability to generate copious dislocations during plastic deformation, even at the lower irradiation temperatures, is an important aspect of the post-irradiation mechanical performance of this alloy.

6.2 The Effect of Tensile Testing Conditions

In situ tensile tests conducted on a set of unirradiated HT9 samples complement those on the irradiated ACO–3 duct material by examining the effect of tensile testing conditions on the macroscopic and phase-specific deformation characteristics of HT9.

6.2.1 Elastic Region

The ferrite phase strain development remains anisotropic at all temperatures within our examined range of 300 °C to 500 °C. However, examination of the relationship between the carbide and matrix phases in the elastic region reveals some differences depending on the test temperature. This relationship is represented by the ratio of the effective ferrite elastic modulus to that of the carbide, as $E_{ferrite}/E_{carbide}$, where the (211) ferrite grains are chosen to represent the behavior of the whole matrix phase, and the (420) grains the carbide phase. Figure 6.3 presents the ratios of effective phase-specific elastic moduli $E_{ferrite}/E_{carbide}$ (aproximated by $E_{ferrite(211)}/E_{carbide(420)}$), as well as the ratio of $E_{ferrite(200)}/E_{carbide(420)}$, where the (200) ferrite peak was selected for its distinct (smaller) effective elastic modulus compared to the bulk of the ferrite phase.

The ratio $E_{ferrite}/E_{carbide}$ increases with increasing test temperature for the continuous strain tests. In the stepwise strain tests, there is no clear dependence of the ratio on test temperature. $E_{ferrite(200)}/E_{carbide}$ does not show a dependence on test temperature in either case. It was previously established that the ratio of the elastic modulus of ferrite to the elastic modulus of the $Cr_{23}C_6$ carbide independently is 0.68. As, in this study, they are constituent phases within the HT9 alloy, they are geometrically constrained, making the ratio of their effective elastic moduli closer to one. As the test temperature is increased,

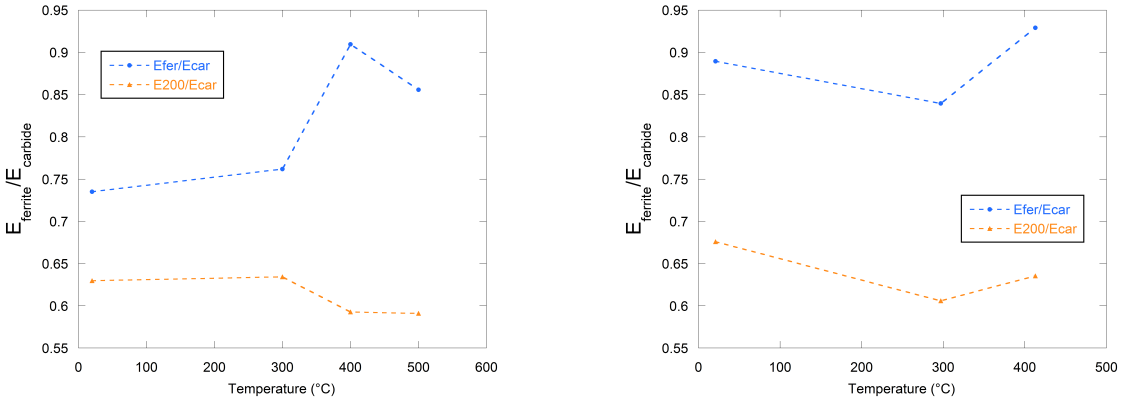

(a) Continuous strain

(b) Stepwise strain

Figure 6.3: Ratio of the effective modulus of the ferrite and the carbide phase.

this ratio comes closer to unity. One explanation for this is the possible precipitation of the coherent α' phase, a chromium-rich ferrite phase in the miscibility gap of the Fe-Cr system. This phase has been known to develop in ferritic and duplex steels near ~475 °C, in a phenomenon known as 475 °C embrittlement. It has been found in a wide range of steels at temperatures between 350 °C and 550 °C. While the α' phase precipitates out from the $\alpha-$ferrite matrix, because the difference between their lattice constants is so small (a=2.877 Å for α' and 2.863 Å for α), the phases would be indistinguishable from one another in our XRD results. Therefore, while we can't look for evidence of the α' phase in the diffraction patterns, we can consider that an increase in hardness of the matrix phase (which can be made up of ferrite and the coherent α' phase invisible to diffraction) would cause the ratio $E_{ferrite}/E_{carbide}$ to increase by hardening the matrix (ferrite +α') phase.

The precipitation of α' in steels results in a slow increase in hardness and an accompanying loss of toughness. A loss of toughness is seen for the HT9 samples at higher test temperatures, shown in fig. 6.5a, but this could be attributable to the reduction in strength and not necessarily to hardening by α'. No α' precipitation was observed after a 10,000 hr anneal of ACO–3 control material at 475 °C (refer to table 6.1), but that control material was distinct (provided by a different manufacturer and subject to different thermo-mechanical treatment) from the material used in the high temperature tensile tests here. The lack of temperature dependence seen in the $E_{ferrite(200)}/E_{carbide}$ does not necessarily contradict the idea of α' precipitation in the matrix phase, as it could form

with a crystallographic preference under deformation. Additional exploration is required to determine if there is any evidence of α' precipitate formation, and, if so, if there is any stress-induced orientation preference of the precipitated phase. The reduced (or, arguably, lack of) test temperature dependence of $E_{ferrite}/E_{carbide}$ in the stepwise strain tests may stem from relaxation of the sample during holding at each displacement step. Particularly since the tests were conducted at elevated temperature, the stepwise straining routine resulted in a repeated pattern of increasing stress (as the crosshead position moved to the assigned displacement step) followed by relaxation (as the sample was held at constant displacement and the stress relaxed). The degree of stress relaxation is greater at higher temperature. The semi-cyclic loading pattern in the stepwise strain tests could result in some strain softening that mitigates the effect of any precipitated hardening phase. Further study is needed to determine the way in which test temperature influences the elastic relationship between the matrix and carbide phases.

Our macroscopic stress-strain results found the magnitude of YS, UTS, and FS all decreased with increasing temperature, as in previous tests on this alloy. In addition, we found the magnitude of the change was most significant at temperatures above ~410 °C, which mirrors the finding in work by Roy of a distinct increase in the effect of tensile test temperature on mechanical properties at a threshold temperature above 400 °C [32]. The ductility of the samples, as measured by the total elongation (%), decreased slightly between the room temperature and 400 °C tests, due to dynamic strain aging, but showed a great increase at 500 °C due to the enhanced plastic flow.

6.2.2 Plastic Region

There was some variation in accumulated stresses within the matrix phase with test temperature, whereas the carbide phase stresses appeared to be largely independent of tensile testing temperature, see fig. 3.15 and fig. 4.12. This is due to temperature enhancement of dislocation mobility in the ferrite matrix phase. Since dislocations are forming within the matrix phase of the material and not within the carbide phase, increased dislocation density with deformation manifests more as stress accumulation within the ferrite phase. At higher temperatures, the dislocations become more mobile due to thermal activation, thereby softening the matrix and reducing some of the stress due to dislocation entanglement.

A representation of the strain hardening, the difference between the UTS and the YS of each sample, is plotted in fig. 6.4 as a function of test temperature. The enhanced mobility

of dislocations at higher temperature prevents the pinning and tangling of dislocations that result in strain hardening, thereby limiting strain hardening at the highest test temperature.

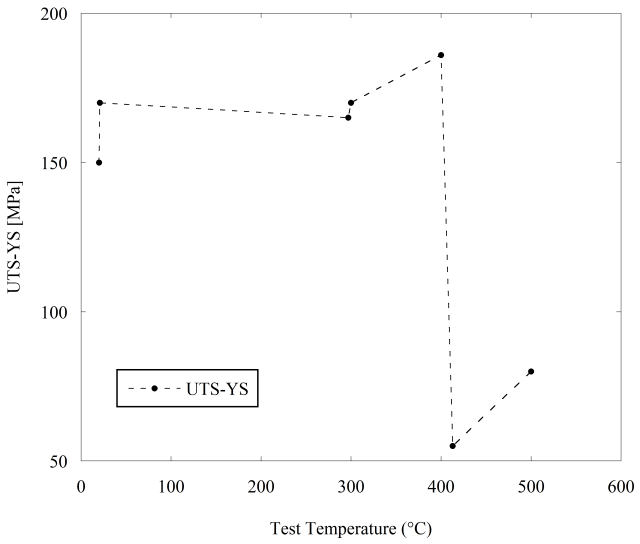

Figure 6.4: The magnitude of strain hardening in each sample, represented as the difference between the UTS and YS, as a function of test temperature.

Because of uncertainty relating to calibration of the strain and stress on different loading stages, when combining data from different experimental setups, it is most useful to compare relative values of the parameters describing material properties. In fig. 6.5a, the relative toughness of HT9 is plotted as a function of test temperature. Relative properties were defined herein as the property value at elevated temperature divided by the value at low temperature using the same straining routine. Room temperature test information was used as standard for the continuous strain tests at beamline 1-ID, and the analogous "low" temperature test was considered to be the 300 °C test for the stepwise strain experiment at MRCAT, since the test at room temperature had no reliable strain information. The relative toughness values were tabulated by estimating the area under the stress-strain curve. Toughness decreases with increasing test temperature, although not as much as the material's reduced strength with temperature might lead one to assume. The substantial increase in total elongation of the samples with higher test temperature offset much of the decrease in strength. However, for the sake of validating structural materials, the toughness and *total* elongation matter little in comparison to the

region of *uniform* elongation. In engineering practice, a structural material strained into the nonuniform elongation region would be considered failed. If increased temperature substantially decreases the strength and reduces the uniform elongation or resilience of the material (the region over which the material can recover from being strained), any increase in its total elongation holds little value. Calculation of the relative resilience of HT9, which depends not on the total elongation but on the uniform elongation, reveals a dramatic decrease in the resilience at 500 °C due to very low uniform elongation, shown in fig. 6.5b. Above 400 °C, the matrix is weak and plastic flow is enhanced by greater dislocation mobility. When the sample was strained at 500 °C, the UTS was reached at very low strain; consequently, most of the interactions between the particle and the matrix took place in the necking region of the 500 °C sample.

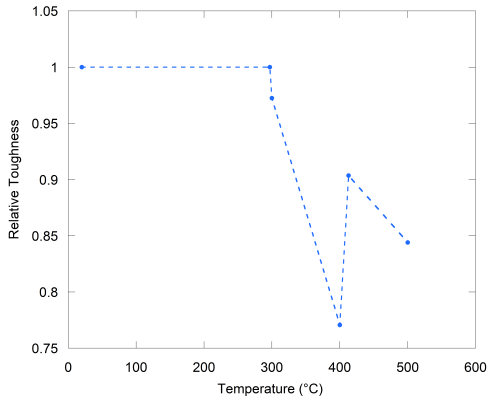

(a) Relative toughness, estimated by the area under the stress-strain curve to the point of failure.

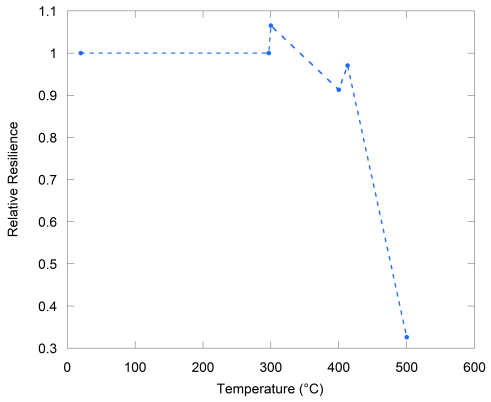

(b) Relative resilience, estimated by the area under the stress-strain curve in the region of uniform elongation.

Figure 6.5: A comparison of the temperature dependence of toughness, the ability of the material to resist fracture, and resilience, its ability to resist permanent deformation.

6.2.3 Dislocation Density Evolution

The pre-existing initial dislocation structure within the martensite laths of HT9 contributes to the strength of the material. This dislocation structure is altered by plastic deformation. The initial dislocation multiplication during plastic deformation, up to an imposed engineering strain of ~4% for the test at 300 °C, led to strain hardening in the ferrite phase, evidenced by the increasing lattice strain in the 0-4% strain region of fig. 6.6b.

Concomitantly, the strain in the carbide rapidly increased, see fig. 6.6c. This can be attributed to dislocation pileup at the carbide-matrix interface. The dislocation density slowly increased until ~5% strain, at which point it saturated. The strain in the ferrite phase decreased at strains beyond 4%, while that in the carbide stayed constant. There is a strain localization apparent in the ferrite phase here. Strain softening without an accompanying decrease in estimated (average) dislocation density can occur when there is rearrangement of dislocations into zones of high and low dislocation densities. This can result in subgrain formation via creation of dislocation walls, and even vein structures that provide clear paths for dislocation motion. This results in an increased mean free path for dislocations, resulting in softening. There are some alternate explanations for strain localization and softening behavior mentioned in [88], but it is difficult to determine the direct cause of the softening observed here. In the higher temperature 410 °C test, neither the dislocation density nor carbide lattice strains saturate. Instead, both follow similar trends of initial rapid increase followed by gradually slower gain after ~2% for the dislocation density and ~1.5% for the carbide strain. The ferrite, by contrast, shows increased lattice strain with dislocation development up to just beyond 1% strain, and thereafter nearly saturates. However, no softening is seen at this temperature. This is again explained by the dislocations multiplying in the matrix and piling up at obstacles like grain boundaries and at the carbide interfaces, increasing the carbide strain.

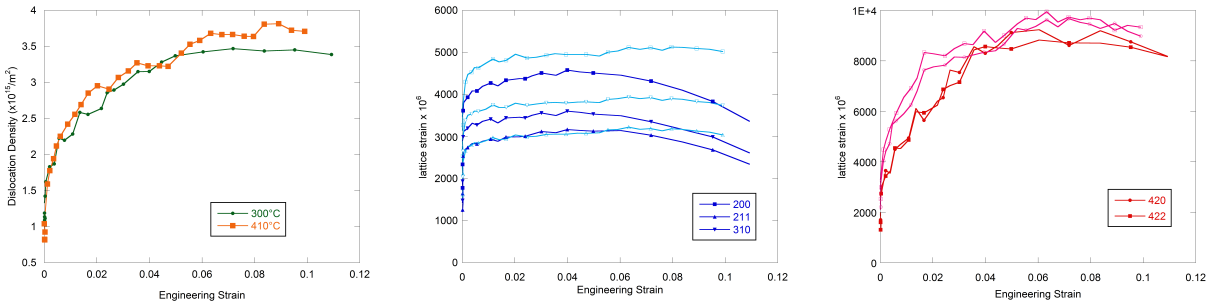

(a) Dislocation Density **(b)** Ferrite Phase Strain **(c)** Carbide Phase Strain

Figure 6.6: Strain evolution in ferrite and carbide phases as a function of macroscopic imposed strain. In fig. 6.6b and fig. 6.6c, the closed symbols and dark colors are for the 300 °C and the open symbols with lighter colors are for 410 °C tests.

As with the irradiated material tests, dislocation density evolution with sample deformation does not follow the Taylor law, as seen by the nonlinearity of fig. 6.7. Accordance with the Taylor Law requires proportionality of $\rho^{1/2}$ and the true stress, meaning the points in the plot would be linear.

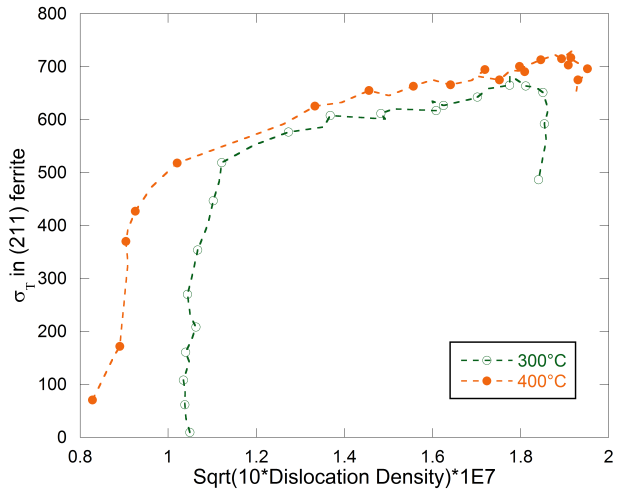

Figure 6.7: A Taylor plot illustrating the relationship between stress in the (211) ferrite grains and the dislocation density.

Chapter 7

Conclusion

7.1 Load Partitioning Behavior of Alloy HT9

In-situ strain testing with X-ray diffraction analysis was conducted on miniature tensile samples of unirradiated HT9, heat 9–607, supplied by ORNL. Tensile tests were conducted at ambient and elevated temperatures of 300 °C, 400 °C, and 500 °C under continuous strain at a constant rate of 2×10^{-4}/s. In situ tensile tests were also conducted with a stepwise straining routine at room temperature, ~300 °C, and ~410 °C. X-ray diffraction peak profile analysis monitored the behavior of the ferrite matrix and carbide precipitate phases of the material. The $Cr_{23}C_6$ carbide structure, making up roughly 3% of the alloy by volume, maintains elastic strength beyond that of the ferrite matrix, contributing substantially to the measured strength of the alloy. With the initiation of plastic deformation, a clear load transfer occurs from the ferrite matrix to carbide particulates. With the carbide phase accommodating further increases in the applied load, the strain in the ferrite phase saturates (completely at low and partially at high test temperatures) until the developing dislocation structure entangles and strain hardens the matrix phase. The matrix and carbide phases then both continue to accumulate additional strain until the sample fails. The strain hardening in the ferrite phase is most pronounced at the lowest test temperatures. The dislocation structure evolves with strain and provides reasonable ductility to the material. The observed macroscopic and phase-specific mechanical behavior of the samples is seen to change dramatically at temperatures above 410 °C. A threshold temperature exists between 410 °C and 500 °C beyond which thermally activated dislocation motion provides substantial enhancement of the plastic flow. Comparable in-situ tensile tests were performed on a set of five HT9 samples extracted from the ACO–3 duct following a six year irradiation in FFTF. The irradiated sample set received fast spectrum neutron radiation doses ranging from 2 dpa to 147 dpa at temperatures from 382 °C to 504 °C. The tensile tests were performed at room temperature with a constant strain rate of 1×10^{-4}/s.

7.2 Influence of Irradiation Conditions on the Microstructure and Mechanical Properties of HT9

In-situ X-ray diffraction measurements during deformation of control and irradiated HT9 steel samples were completed to generate an understanding of the documented changes in macroscopic mechanical properties in terms of the grain-scale response. The distribution of stress between the phases during elastic loading was observed to be distinct in the material irradiated below 420 °C, i.e. material with a high irradiation-induced dislocation density [44] and irradiation-induced minor phases [15, 40]. Collinear elastic deformation behavior, similar to that expected for fiber composites [80], was observed in the material irradiated below 500 °C. The change in the elastic behavior occurs concurrently with the formation of irradiation-induced minor phases and we suppose, without solid evidence, that the effects are related. Moreover, the hardening of the ferrite matrix was distinct between the material irradiated below 420 °C and that irradiated above. In the control material and high temperature irradiated material, the ferrite hardened significantly with deformation, while the ferrite in the material irradiated at low temperature showed limited hardening.

Qualitative indications of increases in dislocation density were observed during the deformation in the form of increased peak breadth and increased root mean square strain in the material in each irradiation condition. Quantitative measurements of the dislocation density before and after deformation indicated a clear and substantial increase during deformation. The initial dislocation density in the ferrite scales linearly with the phase yield strength as expected based on the Taylor law [82].

7.3 Technical Impact and Merit

The set of irradiated samples extracted from the ACO–3 duct in FFTF represents a first set of samples to be irradiated in realistic time-variant conditions, including cyclic temperature and fluence variations. Previous experiments have been done under tightly-controlled experimental conditions, with temperature and fluence only fluctuating within experimental error ranges. In a true reactor environment, temperature and fluence will cycle through normal operations, including periods of shutdown. The material results from the FFTF material tests are the first that can provide comparison between realistic and constant-fluence experiments, including possible evidence that these simpler experiments (done in less time and at lesser cost) can effectively determine the suitability

of materials for use in real-life reactor operating conditions. The results obtained on the irradiated sample set, therefore, are of great interest to both the experimentalist and modeling nuclear materials community.

Additionally, providing a connection between the microstructure and mechanical properties of HT9 throughout a higher (and close to operational) temperature range will have impact on the design, development, and qualification of future, more radiation-tolerant, alloys. A greater understanding of deformation mechanisms and interaction between the inclusion carbide phase and the matrix phase of these materials will also influence the two-phase and physics-based modeling efforts for this class of materials.

Chapter 8

Recommendations for Future Work

There remains active interest in HT9, and other high-chromium ferritic/martensitic and oxide-dispersion strengthened alloys in general, for use as structural materials in advanced next-generation nuclear systems. There are several interesting ways to further explore the mechanical behavior of HT9 and the influence of microstructure under a variety of conditions that would provide an excellent complement to this work.

8.1 Alpha Prime Precipitation

The precipitation of α' changes a material's mechanical properties (increasing hardness, YS, and UTS; decreasing elongation and impact resistance) and the corrosion properties (decreasing corrosion resistance). Appearance of precipitated α' has been credited with strength increases of 30 % to 50 % in Fe14Cr after sufficient aging [89]; the disappearance of α' coinciding with a decrease in DBTT of Fe-Cr alloys following de-embrittling treatment infers the phase plays a strong role in determining the DBTT of high-Cr F/M alloys. However, the factors dominating the appearance and morphology of α' precipitation are at present still points of contention within the nuclear materials community. It has been established that physical property changes attributed to α' precipitation can be reversible by annealing (~600 °C), but the exact conditions and mechanisms for re-dissolution of the phase in ferritic/martensitic materials are not yet established. Our inability to distinguish α' phase precipitations from α ferrite in the XRD studies presented here cripples our understanding of the matrix phase of HT9 (which we know *can* contain α' under certain, presently ill-defined, conditions). Because the α' phase is coherent with ferrite, the constituent atoms (Fe and Cr) are very close in atomic size and have similar X-ray and electron-scattering amplitudes, and the precipitates are generally small (20 Å to 200 Å) and resistant to coarsening, they can't readily be observed using TEM or electron/X-ray diffraction techniques. Chemical microanalysis techniques encounter similar difficulties. The best techniques for examination of this phase appear to be small-angle neutron

scattering (SANS) and mossbauer spectroscopy. SANS examination of same-origin HT9 samples at elevated temperatures following exposure to a controlled matrix of thermo-mechanical processing treatments could provide the correlated data needed to demystify the mechanisms for α' precipitation and the resulting structures.

8.2 Complementary Experimental Techniques

TEM study of the deformed region of the remaining ACO–3 samples, while difficult, could also provide more insight into the dislocation arrangement, average subgrain size, and their relationship to the observed phase strains. SEM of the fracture surfaces and characterization of cracks or dimpled structures to differentiate between fracture modes on the high-temperature samples could provide an additional point of comparison between the continuous and stepwise-strain high temperature tests. Examination of the post-deformation microstructures for evidence of re-dissolution or transformation of precipitated carbide structures is also of interest, although this would require destruction of the specimens in harvesting of the carbides. A coordinated experiment examining the stability of carbide structures under loading and annealing conditions could also prove complementary to this work.

8.3 Further Analysis of Diffraction Data

This work utilized several models of varying complexity to perform diffraction line profile analysis for estimation of dislocation densities. A more structured study examining the validity of using each of the different models for dislocation density estimation using diffraction data (e.g. eCMWP, Williamson-Hall w/ single peak fits, Rietveld fits) would prove useful to the ferritic/martensitic materials community at large. Obtaining diffraction patterns with sufficient peaks and resolution to perform CMWP fitting routines is often difficult. If confidence intervals and conditions surrounding the validity of the more simplified dislocation density and subgrain size estimation models could be established, many more in-situ tensile XRD experiments may be able to provide complementary dislocation evolution studies.

SAXS data was also collected during the high temperature continuous strain tensile tests conducted at 1-ID. Analysis of the SAXS data could provide complement to this work as well as to the SAXS examination of ODS steel performed under similar conditions

by Miao [90].

To evaluate small structure effects in the samples, total scattering and atomic pair distribution function analysis of the diffraction data should be explored. These approaches glean information from the diffuse scattering as well as the intense Bragg peaks (which we considered alone in this work). They are likely to be most useful when there is a very high density of lattice defects, allowing the material to be considered as locally non-crystalline. The theory of these underutilized methods and some software programs facilitating their use are well-described in the text by Egami [91].

8.4 Further Study of Radiation Effects

8.4.1 In-situ XRD of HT9 Samples Irradiated in ATR

As mentioned previously, the high-temperature in-situ XRD tests, particularly those conducted using the modular test station at sector 10, served as a set of pilot tests with the aim of ultimately examining HT9 samples from the same source following their irradiation at ATR to doses of 0.01, 0.1, 0.5, 1, 5, and 10 dpa at temperatures of 300 °C, 450 °C, and 550 °C.

8.4.2 In-situ XRD with Ion Irradiation and Tensile Testing at XMAT

A proposal to create a dedicated beamline at APS for examination of hot samples, called XMAT, is being considered for development at Argonne National Lab. The design proposes an isolated containment vessel that can provide in-situ strain and thermal gradient test conditions, as well as implant high energy heavy ions at controlled doses up to 25 dpa/hr. Diffraction capabilities suggested include synchrotron X-ray diffraction, scattering, SAXS, and tomography. The current status of the X-MAT project is uncertain, but additional study of irradiation damage effects in-situ presents another promising opportunity.

References

[1] "International energy outlook 2016," Tech. Rep. DOE/EIA–0484, U.S. Energy Information Administration, Office of Energy Analysis, U.S. Department of Energy, 2016.

[2] "Technology roadmap update for generation iv nuclear energy systems," tech. rep., Generation IV International Forum, 2014.

[3] M. L. Grossbeck, L. T. Gibson, and S. Jitsukawa, "Irradiaton creep in austenitic and ferritic steels irradiated in a tailored neutron spectrum to induce fusion reactor levels of helium," *Journal of Nuclear Materials*, vol. 233237, Part 1, pp. 148–151, Oct. 1996.

[4] D. Blasl, H. Tsunakawa, K. Miyahara, and N. Igata, "Void swelling and microstructure evolution of a dual phase (ferritic and austenitic) stainless steel," *Journal of Nuclear Materials*, vol. 133134, pp. 517–520, Aug. 1985.

[5] R. L. Klueh, "Elevated temperature ferritic and martensitic steels and their application to future nuclear reactors," *International Materials Reviews*, vol. 50, pp. 287–310, Oct. 2005.

[6] R. Klueh and D. Harries, eds., *High-Chromium Ferritic and Martensitic Steels for Nuclear Applications*. 100 Barr Harbor Drive, PO Box C700, West Conshohocken, PA 19428-2959: ASTM International, Jan. 2001.

[7] A. Kohyama, A. Hishinuma, D. S. Gelles, R. L. Klueh, W. Dietz, and K. Ehrlich, "Low-activation ferritic and martensitic steels for fusion application," *Journal of Nuclear Materials*, vol. 233-237, pp. 138–147, 1996.

[8] L. Mansur, A. Rowcliffe, R. Nanstad, S. Zinkle, W. Corwin, and R. Stoller, "Materials needs for fusion, Generation IV fission reactors and spallation neutron sources similarities and differences," *Journal of Nuclear Materials*, vol. 329-333, pp. 166–172, Aug. 2004.

[9] I. Charit and K. Murty, "Structural materials issues for the Next Generation Fission Reactors," *Journal of the Minerals, Metals & Materials Society*, vol. 62, no. 9, pp. 67–74, 2010.

[10] R. Klueh and A. Nelson, "Ferritic/martensitic steels for next-generation reactors," *Journal of Nuclear Materials*, vol. 371, pp. 37–52, Sept. 2007.

[11] S. A. Maloy, T. Romero, M. R. James, and Y. Dai, "Tensile testing of EP-823 and HT-9 after irradiation in STIP II," *Journal of Nuclear Materials*, vol. 356, pp. 56–61, Sept. 2006.

[12] Y. Chen, "Irradiation effects of HT-9 martensitic steel," *Nuclear Engineering and Technology*, vol. 45, pp. 311–322, June 2013.

[13] D. S. Gelles, "Development of martensitic steels for high neutron damage applications," *Journal of Nuclear Materials*, vol. 239, pp. 99–106, Dec. 1996.

[14] S. J. Zinkle and G. S. Was, "Materials challenges in nuclear energy," *Acta Materialia*, vol. 61, pp. 735–758, Feb. 2013.

[15] O. Anderoglu, J. Van den Bosch, P. Hosemann, E. Stergar, B. H. Sencer, D. Bhattacharyya, R. Dickerson, P. Dickerson, M. Hartl, and S. A. Maloy, "Phase stability of an HT-9 duct irradiated in FFTF," *Journal of Nuclear Materials*, vol. 430, pp. 194–204, Nov. 2012.

[16] J. D. Almer and S. R. Stock, "Internal strains and stresses measured in cortical bone via high-energy X-ray diffraction," *Journal of Structural Biology*, vol. 152, pp. 14–27, Oct. 2005.

[17] M. L. Young, J. DeFouw, J. D. Almer, and D. C. Dunand, "Load partitioning during compressive loading of a Mg/MgB2 composite," *Acta Materialia*, vol. 55, pp. 3467–3478, June 2007.

[18] M. Young, J. Almer, M. Daymond, D. Haeffner, and D. Dunand, "Load partitioning between ferrite and cementite during elasto-plastic deformation of an ultrahigh-carbon steel," *Acta Materialia*, vol. 55, pp. 1999–2011, Apr. 2007.

[19] P. Hedstrom, L. E. Lindgren, J. Almer, U. Lienert, J. Bernier, M. Terner, and M. Oden, "Load Partitioning and Strain-Induced Martensite Formation during Tensile Loading of a Metastable Austenitic Stainless Steel," *Metallurgical and Materials Transactions A*, vol. 40, pp. 1039–1048, May 2009.

[20] S. Cheng, Y. D. Wang, H. Choo, X. L. Wang, J. D. Almer, P. K. Liaw, and Y. K. Lee, "An assessment of the contributing factors to the superior properties of a nanostructured steel using in situ high-energy X-ray diffraction," *Acta Materialia*, vol. 58, pp. 2419–2429, Apr. 2010.

[21] X. Pan, X. Wu, X. Chen, K. Mo, J. Almer, D. R. Haeffner, and J. F. Stubbins, "Temperature and particle size effects on flow localization of 912%Cr ferritic/martensitic steel by in situ X-ray diffraction and small angle scattering," *Journal of Nuclear Materials*, vol. 398, pp. 220–226, Mar. 2010.

[22] K. B. Colas, A. T. Motta, J. D. Almer, M. R. Daymond, M. Kerr, A. D. Banchik, P. Vizcaino, and J. R. Santisteban, "In situ study of hydride precipitation kinetics and re-orientation in Zircaloy using synchrotron radiation," *Acta Materialia*, vol. 58, pp. 6575–6583, Dec. 2010.

[23] M. A. Weisser, A. D. Evans, S. Van Petegem, S. R. Holdsworth, and H. Van Swygenhoven, "In situ room temperature tensile deformation of a 1% CrMoV bainitic steel using synchrotron and neutron diffraction," *Acta Materialia*, vol. 59, pp. 4448–4457, June 2011.

[24] L. Wang, M. Li, and J. Almer, "Investigation of deformation and microstructural evolution in grade 91 ferritic-martensitic steel by in situ high-energy x-rays," *Acta Materialia*, vol. 62, pp. 239–249, Jan. 2014.

[25] S. N. Rosenwasser, P. Miller, J. A. Dalessandro, J. M. Rawls, W. E. Toffolo, and W. Chen, "The application of martensitic stainless steels in long lifetime fusion first wall/blankets," *Journal of Nuclear Materials*, vol. 8586, Part 1, pp. 177–182, Dec. 1979.

[26] T. Lechtenberg, "Irradiation effects in ferritic steels," *Journal of Nuclear Materials*, vol. 133134, pp. 149–155, Aug. 1985.

[27] F. Garner, *Irradiation Performance of Cladding and Structural Steels in Liquid Metal Reactors, in: Materials Science and Technology: A Comprehensive Review*, vol. 10A, ch. 6, pp. 419–543. VCH, Weinheim, 1994.

[28] B. H. Sencer, J. R. Kennedy, J. I. Cole, S. A. Maloy, and F. A. Garner, "Microstructural analysis of an HT9 fuel assembly duct irradiated in FFTF to 155dpa at 443C," *Journal of Nuclear Materials*, vol. 393, pp. 235–241, Sept. 2009.

[29] R. L. Klueh and J. M. Vitek, "Tensile behavior of irradiated 12cr-1movw steel," *Journal of Nuclear Materials*, vol. 137, p. 44, 1985.

[30] C. K. Elliott, G. E. Lucas, R. Maiti, and G. R. Odette, "Microstructures of HT-9 as a function of heat treatment," *Journal of Nuclear Materials*, vol. 141–143, Part 1, pp. 439–443, Nov. 1986.

[31] S. A. Maloy, *AFCI Materials Handbook: Materials Data for Particle Accelerator Applications.* No. LA-CP-06-0904, Los Alamos, NM: Los Alamos National Laboratory, 2006.

[32] A. K. Roy, S. R. Kukatla, B. Yarlagadda, V. N. Potluri, M. Lewis, M. Jones, and B. J. OToole, "Tensile properties of martensitic stainless steels at elevated temperatures," *Journal of Materials Engineering and Performance*, vol. 14, pp. 212–218, Apr. 2005.

[33] J. J. Kai and G. L. Kulcinski, "14 mev nickel-ion irradiated ht-9 ferritic steel with and without helium pre-implantation," *Journal of Nuclear Mat*, vol. 175, pp. 227–236, December 1990.

[34] D. Gilbon and C. Rivera, "Behavior of different ferritic steels under ion, electron, and fast neutron irradiation," *Journal of Nuclear Materials*, vol. 155-157, no. 2, pp. 1268–1273, 1988.

[35] G. Was, J. P. Wharry, B. Frisbie, B. D. Wirth, D. Morgan, J. D. Tucker, and T. R. Allen, "Assessment of radiation-induced segregation mechanisms in austenitic and ferritic-martensitic alloys," *Journal of Nuclear Materials*, vol. 411, pp. 41–50, April 2011.

[36] R. L. Klueh and D. J. Alexander, "Heat treatment effects on impact toughness of 9cr-1movnb and 12cr-1movw steels irradiated to 100 dpa," *Journal of Nuclear Materials*, vol. 253-258, pp. 1269–1274, 1998.

[37] T. S. Byun, W. Daniel Lewis, M. B. Toloczko, and S. A. Maloy, "Impact properties of irradiated HT9 from the fuel duct of FFTF," *Journal of Nuclear Materials*, vol. 421, pp. 104–111, Feb. 2012.

[38] P. Dubuisson, D. Gilbon, and J. L. Sran, "Microstructural evolution of ferritic-martensitic steels irradiated in the fast breeder reactor phenix," *Journal of Nuclear Materials*, vol. 205, pp. 178–189, Oct. 1993.

[39] S. A. Maloy, M. Toloczko, J. Cole, and T. S. Byun, "Core materials development for the fuel cycle R&D program," *Journal of Nuclear Materials*, vol. 415, pp. 302–305, Aug. 2011.

[40] B. H. Sencer, J. R. Kennedy, J. I. Cole, S. A. Maloy, and F. A. Garner, "Microstructural stability of an HT-9 fuel assembly duct irradiated in FFTF," *Journal of Nuclear Materials*, vol. 414, pp. 237–242, July 2011.

[41] S. A. Maloy, T. J. Romero, P. Hosemann, M. B. Toloczko, and Y. Dai, "Shear punch testing of candidate reactor materials after irradiation in fast reactors and spallation environments," *Journal of Nuclear Materials*, vol. 417, pp. 1005–1008, Oct. 2011.

[42] T. S. Byun, M. B. Toloczko, T. A. Saleh, and S. A. Maloy, "Irradiation dose and temperature dependence of fracture toughness in high dose HT9 steel from the fuel duct of FFTF," *Journal of Nuclear Materials*, vol. 432, pp. 1–8, Jan. 2013.

[43] T. S. Byun, J.-H. Baek, O. Anderoglu, S. A. Maloy, and M. B. Toloczko, "Thermal annealing recovery of fracture toughness in HT9 steel after irradiation to high doses," *Journal of Nuclear Materials*, vol. 449, pp. 263–272, June 2014.

[44] P. L. Mosbrucker, D. W. Brown, O. Anderoglu, L. Balogh, S. A. Maloy, T. A. Sisneros, J. Almer, E. F. Tulk, W. Morgenroth, and A. C. Dippel, "Neutron and X-ray diffraction analysis of the effect of irradiation dose and temperature on microstructure of irradiated HT-9 steel," *Journal of Nuclear Materials*, vol. 443, pp. 522–530, Nov. 2013.

[45] S. A. Maloy, M. B. Toloczko, K. J. McClellan, T. Romero, Y. Kohno, F. A. Garner, R. J. Kurtz, and A. Kimura, "The effects of fast reactor irradiation conditions on the tensile properties of two ferritic/martensitic steels," *Journal of Nuclear Materials*, vol. 356, pp. 62–69, Sept. 2006.

[46] U. o. L. Birkbeck College, "School of crystallography," 2006.

[47] H.-R. Wenk and P. V. Houtte, "Texture and anisotropy," *Reports on Progress in Physics*, vol. 67, pp. 1367–1428, 2004.

[48] B. S. H. Van Swygenhoven, "Following peak profiles during elastic and plastic deformation: A synchrotron-based technique," *Review of Scientific Instruments*, vol. 77, no. 1, pp. 013902–013902–10, 2006.

[49] H. M. Rietveld, "Line profiles of neutron powder-diffraction peaks for structure refinement," *Acta Crystallographica*, vol. 22, pp. 151–152, Jan 1967.

[50] H. M. Rietveld, "A profile refinement method for nuclear and magnetic structures," *Journal of Applied Crystallography*, vol. 2, pp. 65–71, Jun 1969.

[51] L. B. McCusker, R. B. Von Dreele, D. E. Cox, D. Louër, and P. Scardi, "Rietveld refinement guidelines," *Journal of Applied Crystallography*, vol. 32, pp. 36–50, Feb 1999.

[52] G. Ribarik and T. Ungar, "Characterization of the microstructure in random and textured polycrystals and single crystals by diffraction line profile analysis," *Materials Science and Engineering a-Structural Materials Properties Microstructure and Processing*, vol. 528, pp. 112–121, Nov. 2010.

[53] G. Ribarik, J. Gubicza, and T. Ungar, "Correlation between strength and microstructure of ball-milled AlMg alloys determined by X-ray diffraction," *Materials Science and Engineering: A*, vol. 387-389, pp. 343–347, Dec. 2004.

[54] B. E. Warren and B. L. Averbach, "The separation of stacking fault broadening in cold-worked metals," *Journal of Applied Physics*, vol. 23, p. 1059, 1952.

[55] T. Ungar and A. Borbely, "The effect of dislocation contrast on x-ray line broadening: A new approach to line profile analysis," *Applied Physics Letters*, vol. 69, pp. 3173–3175, Nov. 1996.

[56] M. Wilkens, "X-ray diffraction line broadening of crystals containing small-angle boundaries," *Journal of Applied Cryst*, vol. 12, pp. 119–125, 1979.

[57] J. Hawthorne and F. Smidt, "Evaluation of fracture resistance of ferritic stainless steels for first wall and blanket applications," vol. 104, pp. 883–886, 1981.

[58] K. Mo, *Microstructural evolution and mechanical behavior in nickel based alloys for very high temperature reactor*. PhD thesis, University of Illinois at Urbana-Champaign, 2011.

[59] B. Clausen, D. W. Brown, M. A. M. Bourke, T. A. Saleh, and S. A. Maloy, "In situ neutron diffraction and elastic-plastic self-consistent polycrystal modeling of ht-9," *Journal of Nuclear Materials*, vol. 425, pp. 228–232, June 2012.

[60] G. Young, T. Capobianco, M. Penik, B. Morris, and J. McGee, "The mechanism of ductility dip cracking in nickelchromium alloys," *Weld J*, vol. 87, pp. 31S–43S, 2008.

[61] T. Saleh, S. Maloy, and T. Romero Tech. Rep. LA-CP-00689, Los Alamos National Laboratory, 2011.

[62] P. Hosemann, Y. Dai, E. Stergar, H. Leitner, E. Olivas, A. T. Nelson, and S. A. Maloy, "Large and Small Scale Materials Testing of HT-9 Irradiated in the STIP Irradiation Program," *Experimental Mechanics*, vol. 51, pp. 1095–1102, Sept. 2011.

[63] A. Sarkar, A. H. Alsabbagh, and K. L. Murty, "Investigation of microstructure and mechanical properties of low dose neutron irradiated HT-9 steel," *Annals of Nuclear Energy*, vol. 65, pp. 91–96, Mar. 2014.

[64] K. Mo, A. Oaks, Y. Miao, and J. F. Stubbins, "Crystalline property calculator," 2013.

[65] G. K. Williamson and W. H. Hall, "X-ray line broadening from filed aluminium and wolfram," *Acta Metallurgica*, vol. 1, pp. 22–31, Jan. 1953.

[66] T. Ungar, I. Dragomir, A. Revesz, and A. Borbely, "The contrast factors of dislocations in cubic crystals: the dislocation model of strain anisotropy in practice," *Journal of Applied Crystallography*, vol. 32, pp. 992–1002, Oct. 1999.

[67] T. S. B. S. A. Maloy, D. Hoelzer, "Core materials development," in *presented at the FCRD Fuels Quarterly Meeting, Salt Lake City, Utah*, 2010.

[68] A. P. Hammersley, S. O. Svensson, M. Hanfland, A. N. Fitch, and D. Hausermann, "Two-dimensional detector software: From real detector to idealised image or two-theta scan," *High Pressure Research*, vol. 14, no. 4-6, pp. 235–248, 1996.

[69] A. Hammersley, "FIT2d: An Introduction and Overview," 1997.

[70] R. B. Von Dreele, J. D. Jorgensen, and C. G. Windsor, "Rietveld refinement with spallation neutron powder diffraction data," *Journal of Applied Crystallography*, vol. 15, pp. 581–589, Dec. 1982.

[71] T. M. Holden, R. R. Hosbons, J. H. Root, and E. F. Ibrahim, "Neutron Diffraction Measurements of Strain and Texture in Welded Zr 2.5 wt. % Nb Tube," in *Symposium U - Nondestructive Monitoring of Materials Properties*, vol. 142 of *MRS Online Proceedings Library*, 1988.

[72] T. M. Holden, C. N. Tom, and R. A. Holt, "Experimental and theoretical studies of the superposition of intergranular and macroscopic strains in Ni-based industrial alloys," *Metallurgical and Materials Transactions A*, vol. 29, pp. 2967–2973, Dec. 1998.

[73] P. Scardi and M. Leoni, "Whole powder pattern modelling," *Acta Crystallographica Section A*, vol. 58, pp. 190–200, Mar. 2002.

[74] T. Ungar, "Dislocation model of strain anisotropy," *Powder Diffraction*, vol. 23, pp. 125–132, June 2008.

[75] T. Ungar, J. Gubicza, G. Ribarik, and A. Borbely, "Crystallite size distribution and dislocation structure determined by diffraction profile analysis: principles and practical application to cubic and hexagonal crystals," *Journal of Applied Crystallography*, vol. 34, pp. 298–310, June 2001.

[76] L. Balogh, G. Ribarik, and T. Ungar, "Stacking faults and twin boundaries in fcc crystals determined by x-ray diffraction profile analysis," *Journal of Applied Physics*, vol. 100, p. 023512, July 2006.

[77] L. Balogh, G. Tichy, and T. Ungar, "Twinning on pyramidal planes in hexagonal close packed crystals determined along with other defects by X-ray line profile analysis," *Journal of Applied Crystallography*, vol. 42, pp. 580–591, Aug. 2009.

[78] A. Larson and R. Von Dreele, "GSAS Manual," 1986.

[79] H. Zhang, M. P. J. Punkkinen, B. Johansson, S. Hertzman, and L. Vitos, "Single-crystal elastic constants of ferromagnetic bcc Fe-based random alloys from first-principles theory," *Physical Review B*, vol. 81, p. 184105, May 2010.

[80] B. Clausen, M. A. M. Bourke, D. W. Brown, and E. stndag, "Load sharing in tungsten fiber reinforced Kanthal composites," *Materials Science and Engineering: A*, vol. 421, pp. 9–14, Apr. 2006.

[81] S. A. Maloy, "Metal alloys for nuclear applications: Needs, advances and challenges," Tech. Rep. LA-UR-12-25608, Los Alamos National Laboratory (LANL), 2012.

[82] G. Taylor, "Plastic strain in metals," *J. Institute of Metals*, vol. 62, pp. 307–324, 1938.

[83] R. E. Stoller and S. J. Zinkle, "On the relationship between uniaxial yield strength and resolved shear stress in polycrystalline materials," *Journal of Nuclear Materials*, vol. 283–287, Part 1, pp. 349–352, Dec. 2000.

[84] A. Cottrell, "Strain hardening at different temperatures," *Philosophical Magazine Letters*, vol. 89, pp. 19–22, Jan. 2009.

[85] C. Tomchik, J. Almer, O. Anderoglu, L. Balogh, D. Brown, B. Clausen, S. Maloy, T. Sisneros, and J. Stubbins, "High energy x-ray diffraction study of the relationship between the macroscopic mechanical properties and microstructure of irradiated ht-9 steel," *Journal of Nuclear Materials*, vol. 475, pp. 46–56, 2016.

[86] S. J. Zinkle, "Microstructures and Mechanical Properties of Irradiated Metals and Alloys," in *Materials Issues for Generation IV Systems* (V. Ghetta, D. Gorse, D. Mazire, and V. Pontikis, eds.), NATO Science for Peace and Security Series B: Physics and Biophysics, pp. 227–244, Springer Netherlands, 2008.

[87] E. E. Bloom, J. T. Busby, C. E. Duty, P. J. Maziasz, T. E. McGreevy, B. E. Nelson, B. A. Pint, P. F. Tortorelli, and S. J. Zinkle, "Critical questions in materials science and engineering for successful development of fusion power," *Journal of Nuclear Materials*, vol. 367–370, Part A, pp. 1–10, Aug. 2007.

[88] K. Farrell, T. Byun, and N. Hashimoto, "Deformation mode maps for tensile deformation of neutron-irradiated structural alloys," *Journal of Nuclear Materials*, vol. 335, pp. 471–486, Dec. 2004.

[89] P. Grobner, "The 885 degree f (475 degree c) embrittlement of ferritic stainless steels," *Metallurgical Transactions*, vol. 4, pp. 251–260, January 1973.

[90] Y. Miao, *Advanced Characterization of Austenitic Oxide Dispersion-Strengthened (ODS) Steels for High-Temperature Reactor Applications*. PhD thesis, University of Illinois at Urbana-Champaign, 2015.

[91] T. Egami and S. Billinge, *Underneath the Bragg Peaks: structural analysis of complex materials*. Pergamon, 2003.